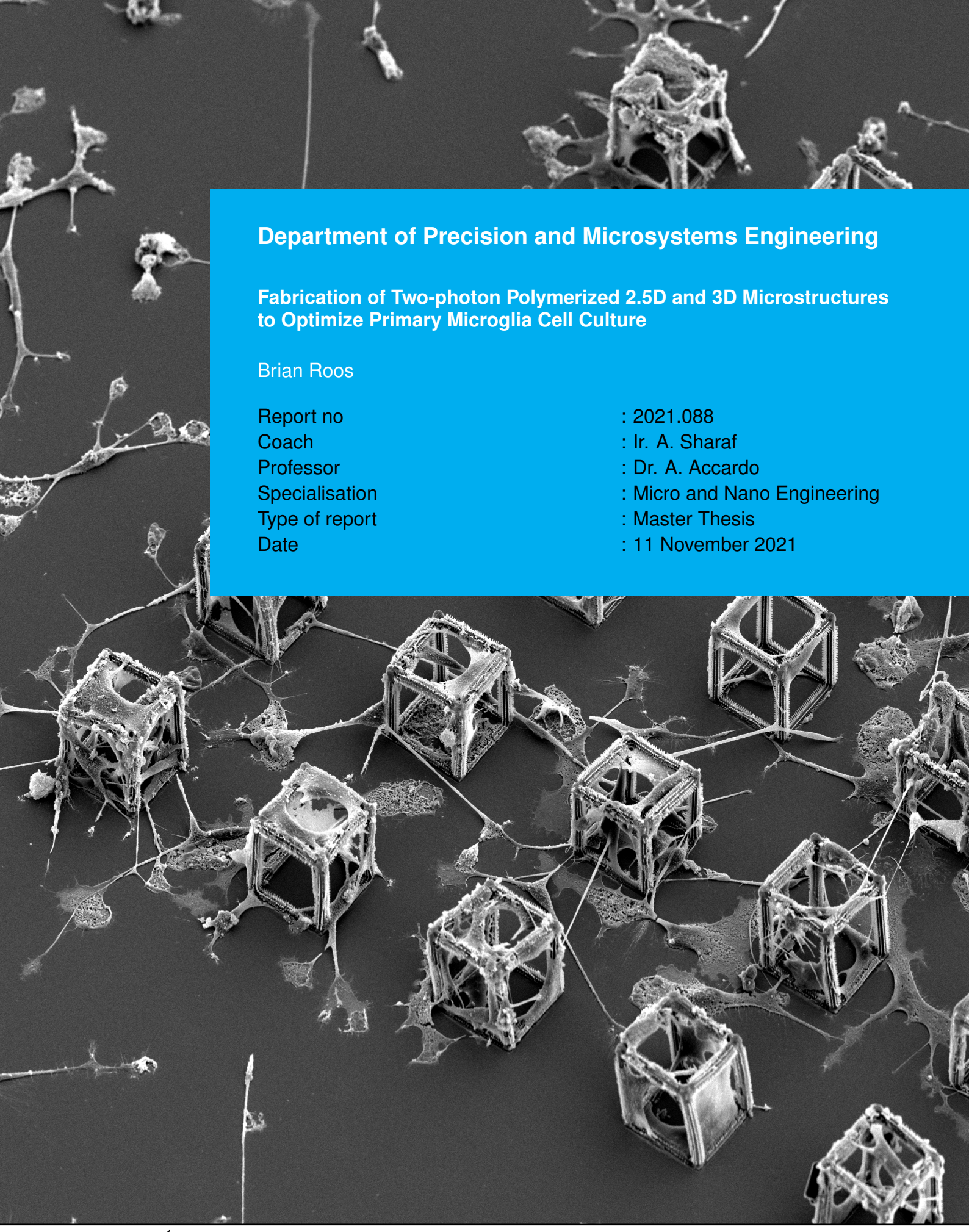

Department of Precision and Microsystems Engineering

Fabrication of Two-photon Polymerized 2.5D and 3D Microstructures to Optimize Primary Microglia Cell Culture

Brian Roos

Report no	: 2021.088
Coach	: Ir. A. Sharaf
Professor	: Dr. A. Accardo
Specialisation	: Micro and Nano Engineering
Type of report	: Master Thesis
Date	: 11 November 2021

TU Delft Delft University of Technology

Challenge the future

Fabrication of Two-photon Polymerized 2.5D and 3D Microstructures to Optimize Primary Microglia Cell Culture

by

Brian Roos

To obtain the degree of Master of Science in Mechanical Engineering

at the Delft University of Technology,

to be defended publicly on November 11, 2021 at 13:00.

Responsible Supervisor

Dr. A. Accardo

Daily Supervisor

Ir. A. Sharaf

Collaborators from the Biomedical Primate Research Centre (BPRC)

Dr. J. Bajramovic

R. Timmerman

Student number:	4290623	
Project duration:	July 1, 2020 – November 11, 2021	
Thesis committee:	Dr. M.K. Ghatkesar	TU Delft, Committee chair
	Dr. A. Accardo	TU Delft, Supervisor
	Ir. A. Sharaf	TU Delft, Daily supervisor
	Dr. J. Bajramovic	BPRC, Supervisor
	R. Timmerman	BPRC, Daily supervisor

TU Delft

Abstract

Microglia, the resident macrophages of the central nervous system, are key players in neuroinflammation and neurodegenerative diseases, such as Alzheimer's and Parkinson's. These cells represent promising cellular targets for therapeutic intervention, therefore a detailed cellular biological knowledge of microglia is of paramount importance. Current microglia ***in vitro*** cell culture models are limited in their ability to recapitulate ***in vivo*** microglia in terms of gene expression and cell morphology. There is growing evidence that mimicking the cellular environment of microglia in the central nervous system will contribute to a more physiologically accurate culture model. Three-dimensional geometries, and physical and biochemical cues similar to the brain's extracellular matrix, are necessary to create a 3D biomimetic ***in vitro*** environment, as microglia cells can sense these environmental cues through mechanosensing.

In this thesis, the effect of two-photon polymerized 2.5D and 3D microstructures on microglia morphology and phenotype was studied through quantitative and qualitative cell analysis. Also, an attempt was made to create ***in vitro*** ramified microglia that resemble ***in vivo*** microglia from a morphological point of view, by controlling the effective shear modulus through dimensional optimization of compliant micro-and nanopillars. It was found that culturing microglia especially on nanopillars enabled an increase of the ramified phenotype and a more complex (i.e. more ramifications) cell morphology as compared to microglia cultured on flat fused silica substrates. Furthermore, we report that microglia cultured on 3D structures exhibit similar phenotypes observed in the 2D and 2.5D cultures, and were more resembling ***in vivo*** microglia in terms of 3D cell morphology.

Preface

I present before you my master thesis, the "Fabrication of Two-photon Polymerized 2.5D and 3D Microstructures to Optimize Primary Microglia Cell Culture". The motivation for this project stems from a sense of duty to contribute to the defeat of neurodegenerative diseases, combined with a deep interest in 3D printing and everything on the micro-and nanoscale. For my grandmother, who is at the beginning stage of Alzheimer's, it is already too late, but I hope that my research might contribute to preventing or curing people who suffer from neurodegenerative diseases in the future.

After a long journey of repeatedly testing my patience, this project, which took place during the corona pandemic, finally comes to an end. I would like to thank everyone that helped me during this project and kept me motivated.

Firstly, I would like to thank my TU Delft supervisors Ahmed Sharaf and Angelo Accardo who provided me with help, guidance and insights during the whole project. Secondly, my supervisors and collaborators from the BPRC: Jeffrey Bajramovic and Raissa Timmerman that also helped greatly and guided me. I would like to thank Raissa specifically for providing the cell culture part, which I could not have done without. Thirdly, I would like to thank Rob, Patrick and the other people from the Lab support that helped me set up experiments and gave me training for the instruments that I needed. Additionally, special thanks to Gert-Jan from the Erasmus medical centre, that provided me with training for the confocal microscope.

Last but not least, I would like to thank Pieter, Damla, Qais and Halis who made the time spent in the lab bearable. Furthermore, special thanks to Malte, Bram, and my housemates Gavin, Cedric, Bas, Mats and Bart for listening to my complaints. And of course my family, my mother Birgitta, my father Henny and my little sister Lisa for always believing in me.

B. Roos
Delft, November 2021

List of Acronyms

2PP - Two photon polymerization
AFM - Atomic force microscopy
AD - Alzheimer's disease
AM - Additive manufacturing
AUC - Area under the curve
BC - Big cage
BC-MP - Big cage micropillar decorated
BC-NP - Big cage nanopillar decorated
BMDM - Bone marrow derived macrophages
CAD - Computer assisted design
CNS - Central nervous system
DLW - Direct laser writing
ECM - Extracellular matrix
F-actin - Fibrous actin
FDM - Fused deposition modelling
GelMA - Gelatin methacryloyl
OC - OrmoPrime coated
IL-10 - Interleukin 10
IR - Infra red
LMP - Laminin coated micropillar
LNP - Laminin coated nanopillar
LS - Laminin coated substrate
MP - Micropillar
ND - Neurodegenerative disease
NP - Nanopillar
PCL - Polycaprolactone
Ped - Pedestal
PD - Parkinson's disease
PEGDA - Polyethylene glycol diacrylate
PLA - Polylactic acid
PLLA - Poly(L-lactic) acid
P(TMC-CL) - Poly(trimethylene carbonate-co-1-caprolactone)
RT - Room temperature
SC - Small cage
SC-MP - Small cage micropillar decorated
SD - Standard deviation
SEM - Scanning electron microscopy
Sub - Substrate
UMP - Uncoated micropillar
UNP - Uncoated nanopillar
US - Uncoated substrate
UV - Ultra violet

List of Figures

List of Tables

Contents

1 Introduction

In this chapter, we provide an introduction to the biological background regarding the brain and the immune system of the central nervous system. Microglia cells are the focus of this study and therefore the behaviour of this cell type in different out-of-body (***in vitro***) environments, is described. In particular, we will draw attention to the physical cues that affect cell morphology. Then, we will show an overview of state-of-the-art culturing techniques and materials to identify a combination of techniques and materials enabling a more ***in vivo*** representation of the microglia cell. At the end of this chapter, we describe the research question, together with the required steps of the research plan.

1.1. Motivation

Research done in the field of the immune system of the central nervous system (CNS) has never been as far developed as it is today. But still, the cause of neurodegenerative diseases (ND) such as Alzheimer's and Huntington's disease is not well enough understood to provide a cure. However, it is known that microglia cells (the macrophages of the CNS) play a role in NDs [1]. Unfortunately, the exact relation between the two is under debate. For this reason, it is important to understand exactly what role microglia have in NDs. Extensive ***in vivo*** (within the body) research has been performed on mice to study the role of microglia in NDs, but the translation of mice to humans is poor and not sufficient enough to provide breakthroughs [2, 3]. Therefore, instead of using mice, studies are performed on the rhesus macaque which is a primate that is more evolutionary close to humans [4]. However, these studies are not as efficient as desired, because the microglia cells when taken out of the body(***in vivo***) and cultured in Petri dishes (***in vitro***), show differences in both the gene expression and cell morphology [5]. This makes it difficult in some cases to make concrete conclusions. The differences are caused by the change of environment (from ***in vivo*** to ***in vitro***) in which the cells are cultured [5]. The biochemical and physical cues in these environments play a huge role in the behaviour of the cell [6, 7]. These differences prove to be a hurdle that is difficult to overcome in the field of neurodegenerative disease studies because what might be the cause of a disease, traced back to the gene expression of ***in vivo*** cells, might be expressed differently for ***in vitro*** cells [5]. The goal of this study is therefore to create a platform on which homeostatic (resting) ramified microglia can be cultured, which are proof of a healthy brain, providing a reference point for the comparison of ND affected microglia cells. Furthermore, the morphology of primary ***in vitro*** microglia cells is documented, then compared to primary ***in vivo*** microglia cells and an attempt to reduce the morphological differences is made. This goal is to be achieved using a combination of structural mechanics(material geometry), biocompatible material(material stiffness) and micro/nanoscale textured topography. The realisation of such a platform will result in a decrease of both animal and human donors and hopefully act as a stable basis to increase the efficiency of research in this field.

1.2. Microglia cell behavior

1.2.1. Biological background

The brain, together with the spinal cord, make up the central nervous system (CNS). Most of the functions of the body and mind are controlled by the CNS, with the brain processing all internal and external information

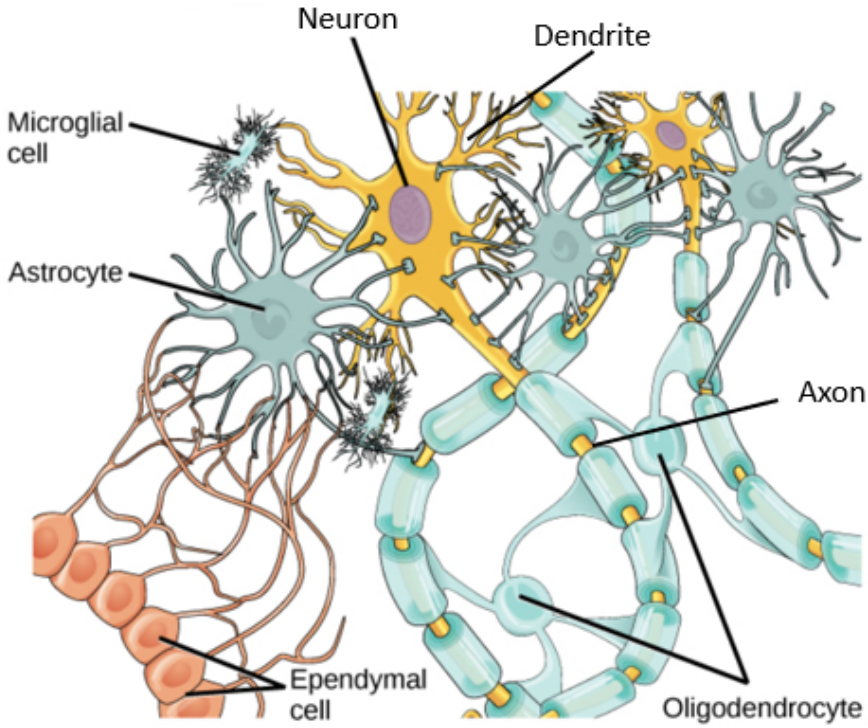

Figure 1.1: Depiction of the cell composition of the CNS, showing neurons with axon and dendrite, and the 4 glial cells: astrocytes, oligodendrocytes with myelin sheet around the axon, ependymal cells, and microglia cells. Image adapted from [8].

and the spinal cord acting as a bridge between the body and the brain to process this information. The information processing in the brain is performed by neurons. These cells process information, received by chemical or electrical synapses through dendritic trees, by using electrical signals that are generated within the cell and are transmitted via axons (typically 0.1 μm to 10 μm in diameter for primates [9]) to the spinal cord or other neurons [10]. To maintain this steady state of constant exchange of information in the healthy brain or homeostasis, a variety of support cells called glial cells exist. There are a total of four types of glial cells in the CNS (see fig. 1.1), each with its functions. **Astrocytes** are the most abundant glial cell types in the human brain, making up 20-40% of all glial cells [11]. This cell helps in maintaining the integrity and permeability of the brain-blood barrier [12]. Also, astrocytes perform CNS repairs and regulate neurotransmitter (chemical signals) uptake and release [12]. **Oligodendrocytes** produce myelin sheaths that isolate segments of neuronal axons, which enables signal transduction at high velocity that is necessary for signal processing through axons [13]. **Ependymal cells** are neuronal support cells that form the ependyma, an epithelial lining of the ventricles in the brain and the central canal of the spinal cord [14].

Microglia cells are the macrophages of the CNS, and play a key role in homeostasis and innate immune responses [15]. These cells maintain the homeostasis of the brain by interacting with astrocytes and clearing cellular debris, such as damaged axons and dead neurons through phagocytosis [16], which is translated from Latin as cell eating. Activation and dysfunction of microglial cells are associated with neurodegenerative diseases, such as Alzheimer's disease (AD) and Parkinson's disease (PD) [15]. However, how this contributes to neurodegeneration is not well understood. Good microglia ***in vitro*** models are instrumental in obtaining this knowledge.

Primary microglial cell cultures, extracted from macaque brains, can provide insights into innate immune responses that are possibly relevant for neurodegenerative disease [17]. Rhesus macaques are evolutionarily close to humans and can be bred to be free of certain neurological diseases [17], giving the advantage to culture healthy microglia. Recent studies have however demonstrated that primary microglia only partially recapitulate microglia ***in vivo*** [18]. The gene expression levels of a large variety of gene products were found to differ and the morphology did not recapitulate the morphology of healthy microglia ***in vivo***. Also, the method to extract microglia from brain tissue is a long and careful process, taking approximately 6 hours [19]. This process might even affect gene expression because of the chemicals and separation steps that are needed [19]. In addition, recent studies have shown that CNS-specific cues are important to recapitulate the microglia signature ***in vivo*** [7]. Furthermore, classical ***in vitro*** culturing of cells is performed in Petri dishes, which is considered to be a 2D culturing environment. This 2-Dimensional way of cell culturing shows a mismatch in the environment of microglia in the brain, wherein microglia are located in a 3D environment. Besides, the mechanical stimuli of the traditional ***in vitro*** culturing environments, such as Young's modulus of glass coverslips or microscope slides (~70 GPa [20, 21, 22]), are several orders of magnitudes higher than that of the brain (1-2 kPa [23, 24, 25]). This material property is known to affect cell adhesion, migration, differentiation and phenotype polarity [26]. For example, astrocytes prefer stiff substrates, whereas cortical neurons show more branched morphology on softer substrates (200 Pa vs 9000 Pa) [26].

As a result, a better way of culturing cells in a more ***in vivo*** like environment is desired for ***in vitro*** cell cultures. Culturing microglia cells in 3D scaffolds that mimic the ***in vivo*** environment both in terms of geometry and stiffness, is expected to increase the knowledge on the effect of three-dimensional structures on the morphological representation and gene expression of microglial cells. This might contribute to better microglia ***in vitro*** models to study the role of microglia in health and disease.

1.2.2. Microglia Phenotypes

Multiple microglia phenotypes are present ***in vivo*** and ***in vitro***, and they differ slightly in morphology. Here below, we present a graphical representation and a short description of the phenotypes present both ***in vivo*** and ***in vitro***. In addition, we show a table that sums up characteristic dimensions of ***in vivo*** human microglia phenotypes existent in the white matter of the brain and operates as a reference during the cell experiments to categorize the cells.

Table 1.1: Important properties for the morphological analysis of human microglia cells extracted from white matter, data from [19].

	Area (μm^2)	**Min feret's diameter** (μm)	**Max feret's diameter** (μm)	**Total process length** (μm)
Ramified	16.4 ± 1.2	3.6 ± 0.19	6.5 ± 0.5	436.0 ± 42.4
range	9.11 - 24.4	2 - 4.8	4.8 - 9.9	290.3 - 761.7
primed	42.74 ± 3.6	5.8 ± 0.26	10.1 ± 0.7	268.2 ± 44.3
range	25.27 - 64.2	4.7 - 7.3	6.8 - 14.3	123.6 - 594.5
Reactive	59.6 ± 6.4	7.4 ± 0.5	11.0 ± 0.8	107.7 ± 17.0
range	18.3 - 89.9	3.9 - 9.0	6.0 - 16.0	25.9 - 187.8
Amoeboid	70.2 ± 7.0	8.2 ± 0.5	12.3 ± 0.7	6.8 ± 2.5
range	37.3 - 111.9	5.8 - 11.2	8.7 - 16.2	0.0 - 19.5

in vivo **phenotypes**

The microglia phenotypes that appear within the CNS (***in vivo***) can be categorised into 4 different types: ramified, primed, reactive, and amoeboid. In table 1.1 we provide the characteristics for each phenotype present in white matter. The characteristics such as cell area, the minimum and maximum Feret's diameter(the distance between two parallel planes tangent to the cell membrane), and the total process length are helpful during the cell analysis. Furthermore, here below, we present a short description for each phenotype:

- **Ramified** (fig. 1.2a): In the steady-state, ramified microglia are the sensing phenotypes with extensively ramified processes that search for chemical or physical cues that indicate the presence of inflammation. This phenotype is the smallest in surface area, has the smallest, slightly ellipsoid soma/core diameter, but the longest processes (seetable 1.1).

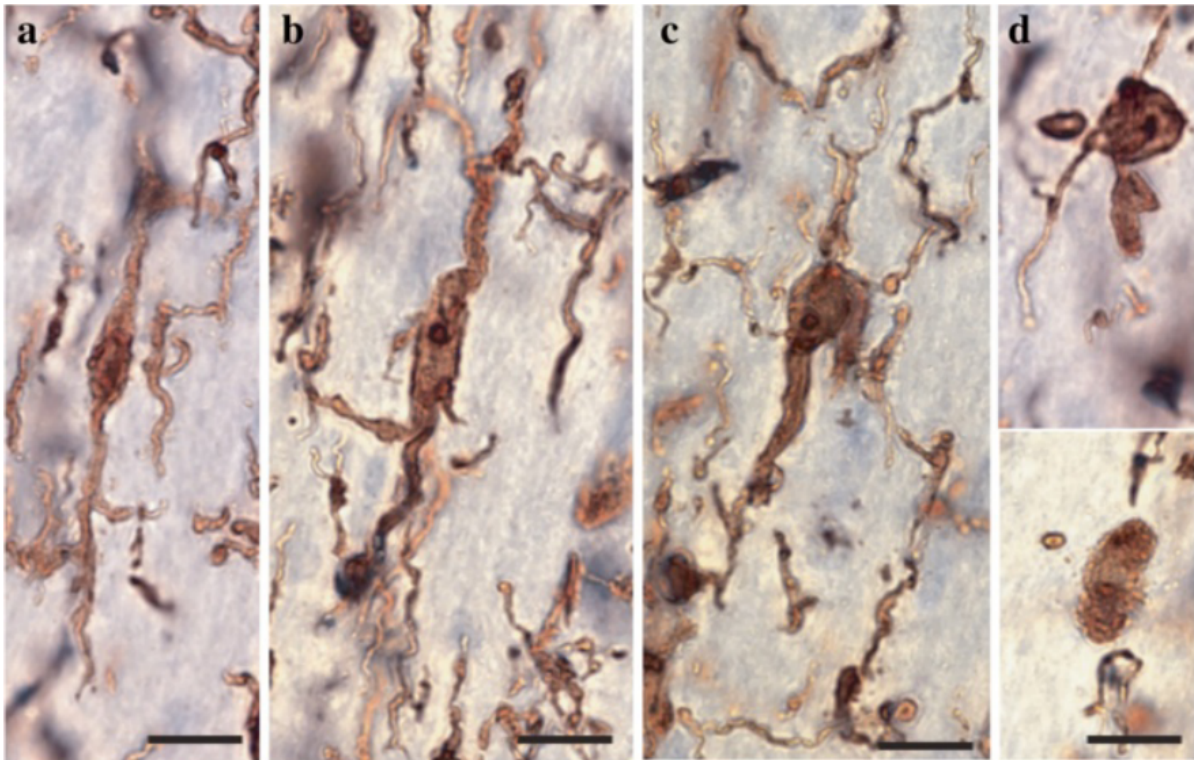

Figure 1.2: Four main phenotypes of microglia cells are present in the white matter tissue of the human brain. **(a)** Ramified phenotype, with highly ramified processes and small soma, **(b)** primed phenotype, with slightly less ramified processes, **(c)** reactive phenotype with a slightly more round soma, **(d)** (upper corner) amoeboid phenotype, round cell body with 2 processes, (lower corner) amoeboid phenotype without processes. Brain sample thickness 500 μm, scale bars 10 μm [19].

- **Primed** (fig. 1.2b): The primed phenotype is an age-induced immune-activated phenotype, that exhibits an increase in immunoreactivity for inflammatory-related microglial markers [27]. This phenotype displays a slightly larger soma diameter, but shorter processes than the ramified ones.
- **Reactive** (fig. 1.2c): The reactive phenotype is a transitional state between ramified and amoeboid. This phenotype still displays some processes, which are in general longer than the cell body diameter. Moreover, it can move inside the brain and secretes pro-inflammatory molecules to signal other cells to proliferate and come to the area of inflammation. These cells have a bigger core but fewer processes than the ramified and primed type.
- **Amoeboid** (fig. 1.2d): The amoeboid phenotype, is the completed phagocytic state of the microglia cells. When in this state, the cell can easily move inside the brain, isolate and then phagocytose cellular debris. At most, this phenotype displays 2 unbranched processes, exhibiting a length within the diameter of the cell body.

in vitro phenotypes

The microglia phenotypes existent within the ***in vitro*** cultures from this study are morphologically different to ***in vivo*** microglia. For this reason, categorising is done in the following way:

- **Flat amoeboid** (fig. 1.3a): The phenotype that is present ***in vitro***, are more round and spread out over the surface (diameter ≈ 40 μm) as compared to the ***in vivo*** counterpart (diameter ≈ 12 μm).
- **Globular** (fig. 1.3b): Cells that are almost spherical in shape. Not to be confused with dead cells, as the cell membrane is still completely intact.
- **Non-amoeboid**:

– **Non-ramified (reactive)** (fig. 1.3c) Numerous morphologically irregular looking ramified-like and non-ramified cells, that do not fit in any of the categories mentioned above. Resembles the ramified cell in morphology, as it has multiple branches but not as long or ramified as the ramified phenotype. Furthermore, it is good to note that for ***in vitro*** cultures no hard description exists for a reactive cell. This is why this "reactive"-like phenotype together with the ramified phenotype are classified as non-amoeboid.

– **Ramified** (fig. 1.3d): Looks morphologically like the ***in vivo*** counterpart in terms of ramified branching that spread in multiple directions. A few criteria were made to classify the cells as ramified cells :

1. A cell is deemed ramified if at least 3 primary branches are present.
2. A branch is considered primary if its length is equal to the minimum Feret's diameter of the cell soma.

- **Bi-polar** (fig. 1.3e): A rod-shaped (polarized) phenotype which looks morphologically like an amoeboid cell but with one process at each pole/ side of the cell soma. Not much is known of the function of this phenotype.

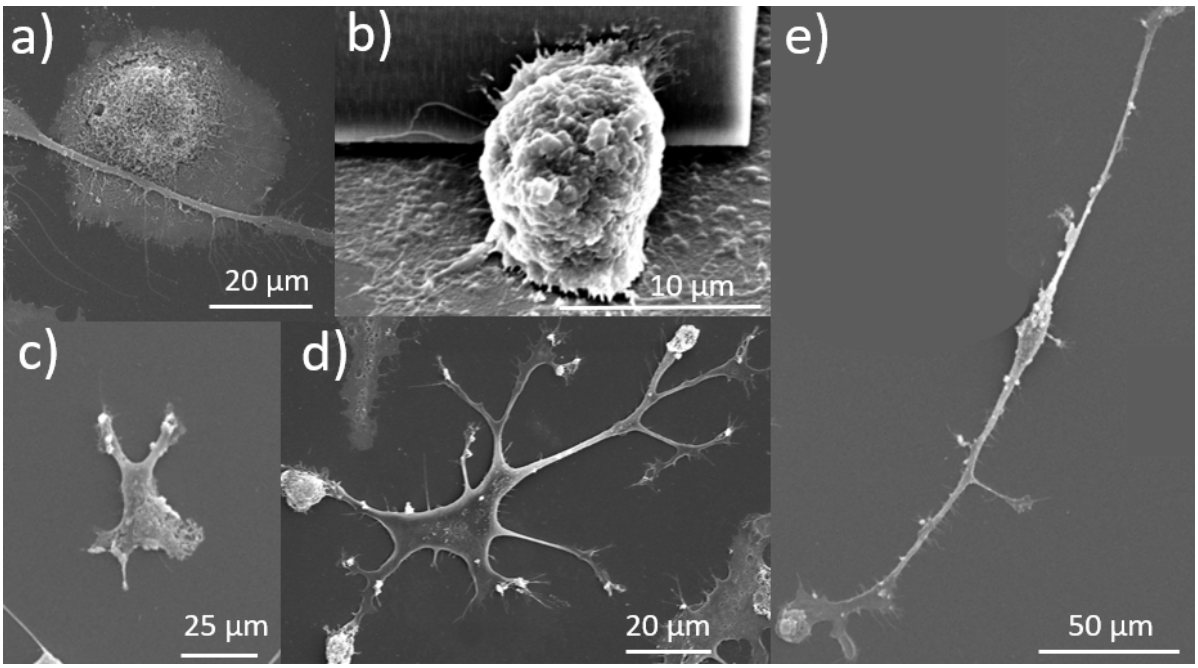

Figure 1.3: The phenotypes of microglia cells that are present in the ***in vitro*** experiments, from SEM images: **(a)** Flat amoeboid cell on a fused silica substrate, a round cell with a flattened cell body. **(b)** Globular cell on a fused silica substrate, spherically shaped cell with a small soma. **(c)** Non-amoeboid (reactive) on a fused silica substrate, a non-ramified cell that does not fit in the other categories. **(d)** The ramified phenotype on a fused silica substrate, showing 6 primary branches with side branches and a relatively small soma. **(e)** Bi-polar phenotype on a fused silica substrate, is a long rod-shaped cell with two poles extending from each side of the soma.

1.2.3. Mechanosensing and the effect of micro-/nano topography on microglia cell morphology

Mechanosensing

Microglial mechanosensing is the process of sensing the environment of the brain for mechanical stimuli (physical cues) [28]. Mechanosensing is performed by lamellipodia and filopodia, which are folds in the cell membrane that are formed by the rearrangement of the complex network of proteins in the skeleton of the cell (the cytoskeleton) [29, 30]. Lamellipodia and filopodia, both consist of the protein fibrous actin (F-actin). Lamellipodia are the leading edge of the cell membrane, whereas filopodia are the protrusions of the cell membrane (see fig. 1.4a), both are present on microglia cell processes [29, 30]. These protrusions sense the environment for both biochemical and physical cues that indicate inflammation or foreign body objects [29, 30].

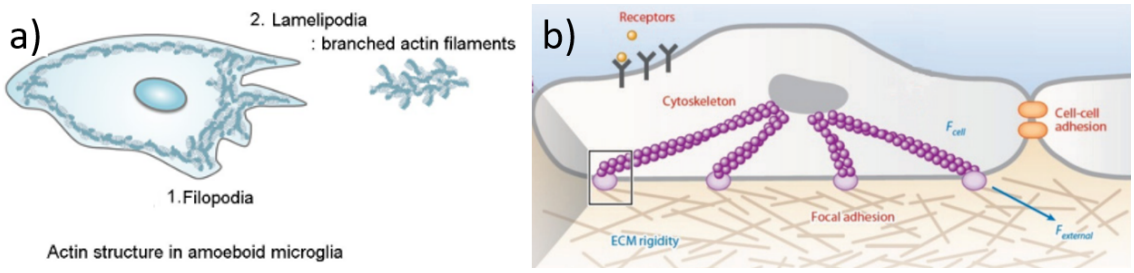

Figure 1.4: **(a)** Representation of filopodia and lamellipodia present in the cytoskeleton of an individual microglial cell [29]. **(b)** Interaction between cell and ECM, through focal adhesion of the filopodia (purple) to ECM. Adapted from [26].

The physical cues are detected through receptors, such as mechanically activated cation channels using a protein called PIEZO1. This protein enables the detection of the shear stiffness of the brain's extracellular matrix (ECM) [31], a 3D network that provides structural and biochemical support to surrounding cells [32]. Through a process called mechanotransduction, the physical detection of the shear stiffness is transduced in a chemical signal, which translates to an increase (stiff material) or decrease (soft material) in F-actin formation [33]. Thus increasing (flattened cell membrane) or decreasing the stress in the cell membrane depending on the stiffness of the environment [33].

The ECM of the brain consists of three major components. The basement membrane lies around the cerebral vasculature, the perineuronal net which surrounds the cell bodies and dendrites of neurons and the neuronal interstitial matrix that surrounds both neurons and glial cells [7]. These components in turn consist of proteins and molecules such as glycosaminoglycans, proteoglycans, glycoproteins, and low-level fibrous proteins such as laminin, fibronectin and collagen [7]. These proteins provide nutrition, protection, maintain the stiffness of the brain and are vital in maintaining the homeostasis of the brain [7].

The Cell-ECM interaction or cell-cell interaction happens through focal adhesion (see fig. 1.4b). Focal adhesion kinase is the process of binding cell-to-cell or cell-to-ECM, through the binding of integrins(the main receptors that connect the cytoskeleton to the ECM [33]) to proteins present in the ECM or cell [34]. The Cell-ECM interaction as seen in fig. 1.5 happens in 5 steps:

1. Protein unfolding after adsorption onto the surface.
2. Filopodial sensing using integrins on the tips.
3. Integrin binds to proteins, exerting force on cell membrane through focal adhesion kinase.
4. Proteins then bind to actin in the cytoskeleton and the forces on actin filaments are transmitted to intermediate filaments.
5. The cytoskeleton and morphology of cells are altered.

The optimal surface topography feature dimensions for BV2 microglia (murine cell line) that promote adhesion are < 70 nm, above this, integrin clustering is disrupted [34]. Taking this knowledge into account, one can hypothesize that it is desirable to create an environment that mimics both the physical and biochemical

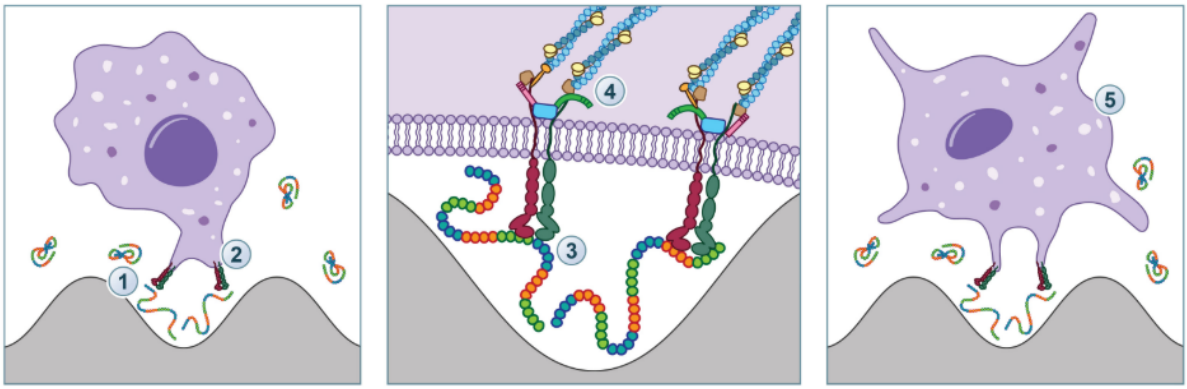

Figure 1.5: The mechanism behind the cell-ECM interaction: 1. Protein unfolding after adsorption onto the surface. 2. Filopodial sensing using integrins on the tips. 3. Integrin binds to proteins, exerting force on cell membrane through focal adhesion kinase. 4. Proteins then bind to actin in the cytoskeleton and the forces on actin filaments are transmitted to intermediate filaments. 5. The cytoskeleton and morphology of cells are altered [7].

cues by simulating the brain's shear modulus, combined with the right ECM proteins. An attempt to simulate the brain's environment is through nanopatterning and using nanopillars/fibres, examples can be seen in the next subsection.

The effect of Nano-/microfibers and nanopatterning on microglia cell morphology

Recent research in the field of brain implants has concluded that inflammation surrounding the area of the implant can be decreased when nanopatterning the surface of the implant [7]. In addition, when using fibres as thin as the proteins filaments in the brain's ECM, a reduction of the inflammatory state of the microglia cells is visible. In this subsection, the effect of nanoscale based surface topography and dimensioning on microglia cell behaviour are discussed.

Micro-/nanofibers

The fibres in scaffolds come in two variations, randomly oriented or aligned. Here below a description of the effect on cells will be given for both:

Randomly orientated

In a study performed by Pieres et al.(2015) on the effect of the surface on microglia function, a comparison was made between primary microglia (obtained from postnatal 1–2 days old Wistar rat pups) cultured on fibrous scaffolds consisting of randomly oriented microfibers with a diameter of 1.46 ± 0.14 μm made from poly(trimethylene carbonate-co-1-caprolactone) (P(TMC-CL)), and on a flat surface of the same material. An increase in Interleukin 10 (IL-10) concentration, an anti-inflammatory cytokine, was seen from the microglia cells cultured on the fibrous scaffold [35]. Additionally, the cells cultured on flat substrates presented a round shape and long protrusions (fig. 1.6a), whereas cells cultured on the electrospun fibres presented a smaller and more elongated cell body (fig. 1.6b). In a different study by Saino et al.(2011), introducing smaller fibres (Poly(L-lactic) acid (PLLA)) that are in the submicron range or nanometer range (0.55 - 0.61 μm) to murine macrophage-like cell line (incubated for 7 days), results in a more elongated cell body with respect to cells on a flat surface (fig. 1.7D andE).

Aligned fibres

Aligned fibres in combination with big enough pores, allows better cell penetration deeply into the structures. In the same study by Saino et al. (2011), it was shown that aligning PLLA nano-microfibers (0.55 - 1.60 μm) on a PLLA scaffold showed a less amoeboid morphology for macrophages (fig. 1.7B and D), when compared to a flat surface (fig. 1.7A) or randomly oriented fibres (fig. 1.7C and E). These immuno-responsive cells have a highly similar cell composition as microglia, and the genes present in the sensome overlap greatly [36]. For this reason, macrophages can be used to predict microglia behaviour.

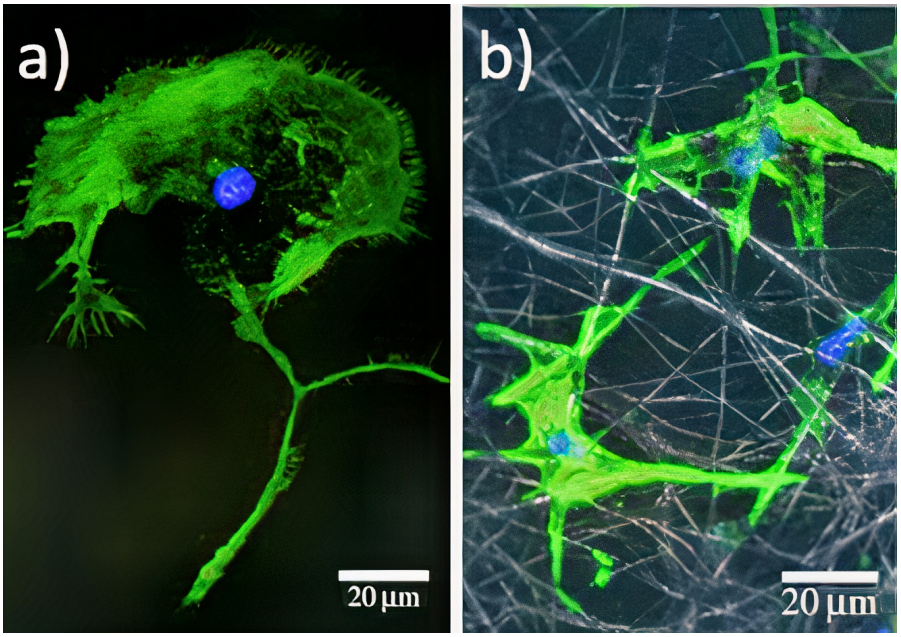

Figure 1.6: **(a)** Microglia cells when cultured (5 days) on flat P(TMC-CL) substrates. Microglia cells cultured on a flat surface displayed a round morphology with 2 long protrusions. **(b)** Microglia cells cultured on the randomly oriented fibrous scaffold displayed a more elongated cell body. The green colour represents F-actin (protein), blue colour cell nuclei. Image adapted from [35].

Nanopatterning

Nanopillars

In a study on microglia cell behaviour on a nanotextured silicon surface, BV-2 microglial cells (murine cell line) were seen to detect nano- and micropatterned structures[38]. When the grain size of these nano/microspikes was increased, the cells display a more elongated and less round morphology (fig. 1.8b), when compared to a flat and untreated surface (fig. 1.8a). The surface roughness of the untreated silicon sample is 1.3 nm (fig. 1.8a)and that of the microspikes surface is 50 nm (fig. 1.8b).

Furthermore, nanopillars can affect the effective stiffness of the substrate through bending in the direction of the force exerted by a cell [39]. Using high aspect ratio nanopillars (large height, small diameter) as compliant wire flexures resulted in an effective shear modulus that was 25,000 times smaller than the bulk shear modulus of the same material [39].
The effective stiffness could be calculated as in eq. (1.1), where $\overline{G}$ is the effective shear modulus, D the diameter of the nanopillar, L the height, f the surface coverage (surface covered by pillars/ total surface in question)

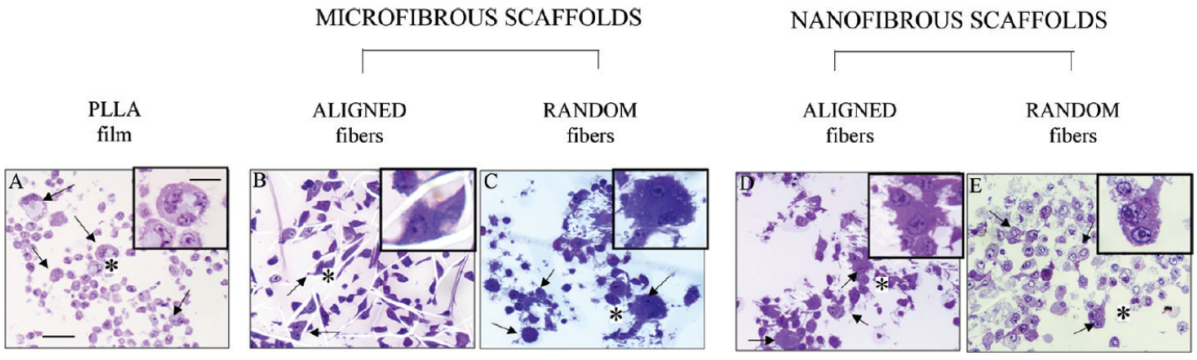

Figure 1.7: Macrophage cells incubated for 7 days on **(A)** PLLA films, **(B)** micro-aligned, **(C)** micro-random, **(D)** nano-aligned, and **(E)** nano-random fibrous scaffolds. scale bar = 45 µm, scale bar in zoomed-in rectangle = 20 µm [37].

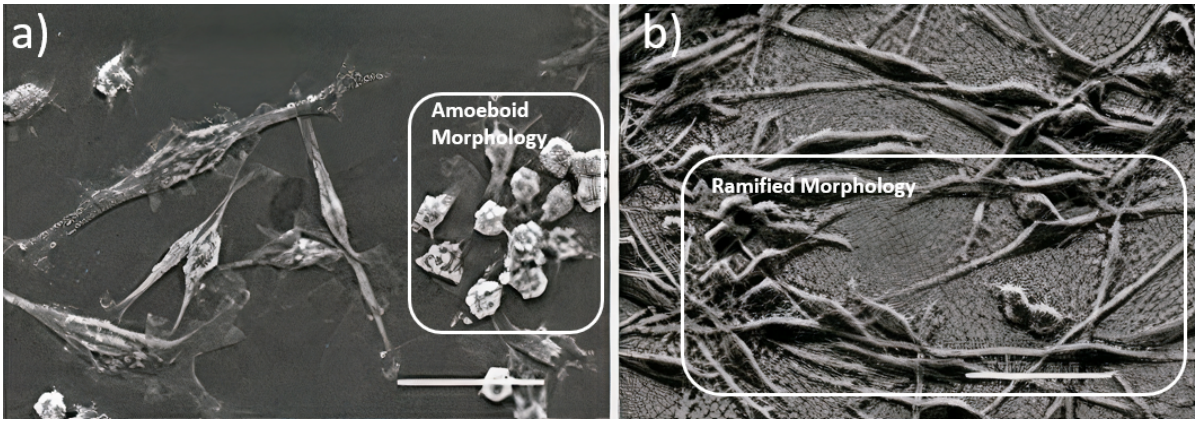

Figure 1.8: SEM images of BV-2 microglial cells. **(a)** Amoeboid morphology cultured on amorphous silicon, roughness 1.3 nm. **(b)** Laser-processed silicon with microspikes, showing a more ramified morphology at a roughness of 50 nm. Both scale bars 50 μm, image resolution enhanced, adapted from [38].

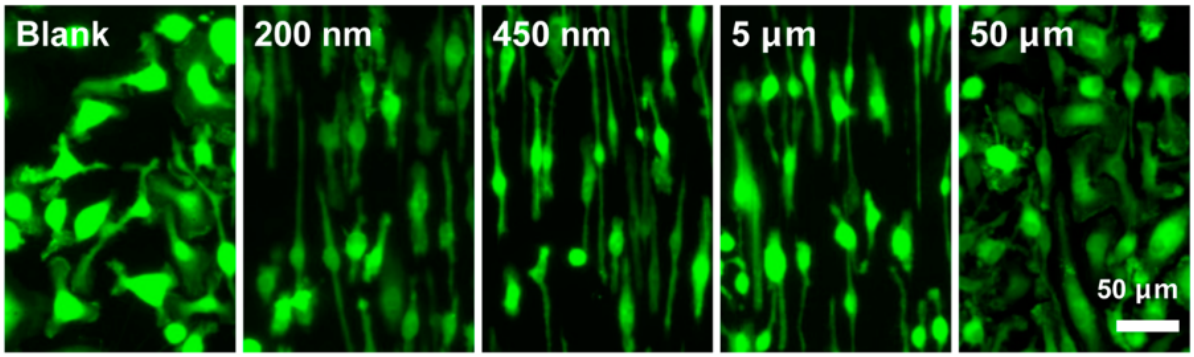

Figure 1.9: Fluorescence micrographs of BMDM after 24 h culture on bulk Ti substrate with 200 nm, 450 nm, 5 μm, and 50 μm grating patterns and nonpatterned control [40].

and E the Young's modulus of the bulk material [39].

$$\overline{G} = \frac{3}{16}\left(\frac{D}{L}\right)^2 fE \tag{1.1}$$

Nanogrooves

A study by Luu et al. (2015), showed that using nanogrooves on a flat Titanium surface changes the amoeboid morphology of bone marrow-derived macrophages (BMDM) (cells derived from femurs of C57BL/6 mice, cultured for 1 day) to a more elongated morphology (fig. 1.9). Here again, macrophages (BMDMs) are used as an indicator to show the behaviour of immune-response cells on a 2D nanopatterned surface. Due to the similarity of macrophages to microglia cells, it is expected that nanopatterning will affect microglia morphology as well. The BMDMs showed higher expression of pro-healing phenotypic markers and alignment in the direction of the grooves, for grooves sizes ranging between 400 nm to 5 μm in width [40].

Prediction of microglia behaviour in 3D

Based on the above-mentioned statements, about the effect of micro-/nanoscale structures and patterning on the behaviour of microglia, a behavioural prediction of microglia cells in a 3D engineered environment can be made: Using micro-/nanopillars, with spatial features mimicking the diameter of both axons and filopodia (200 nm - 10 μm range), and a controlled structure made out of aligned micro-/nanofibers, will provide a three-dimensional cell morphology that mimics ***in vivo*** microglia in general. However, even if the ***in vivo*** cell morphology is mimicked, the gene expression might still be different. This gap might be closed by

using a coating that mimics the composition of the brain's ECM (e.g. biochemicals and proteins), this topic will be covered later.

1.3. State-Of-The-Art: Micro-manufacturing techniques for *in vitro* 3D microglia cell culturing

1.3.1. Manufacturing Techniques

Classical cell cultures are 2D cultures performed in a Petri dish, usually made out of borosilicate glass or soda-lime glass. Newer culture methods include: 3D polymeric structures, hydrogels, micro/nanofibre meshes, or porous materials. The corresponding manufacturing methods and materials used, are described in the sections below.

3D Micro-manufacturing techniques for in vitro 3D cell culturing

Extrusion based printing, electrospinning and two-photon polymerization were investigated because of the wide adoption in the medical industry for tissue engineering and specifically cell culturing. The reasons for wide adoption are the possibility of rapid prototyping, high controllability of spatial features, and because the materials that are used with these techniques provide material properties that are favourable for culturing microglia cells. Furthermore, the order in which we present the techniques shows the development of the techniques utilized in the biomedical industry for tissue engineering. The printing of scaffolds is performed on increasingly smaller scales, with the two-photon polymerization (2PP) technique being able to control features on even the smallest scale (nanometer scale). Eventually, a comparison of important parameters, such as the resolution (smallest increment of movement) and the minimum feature size (smallest spatial dimension of a physical body), point out why the 2PP technique is ideal for printing 3D microstructures to culture primary homeostatic microglia.

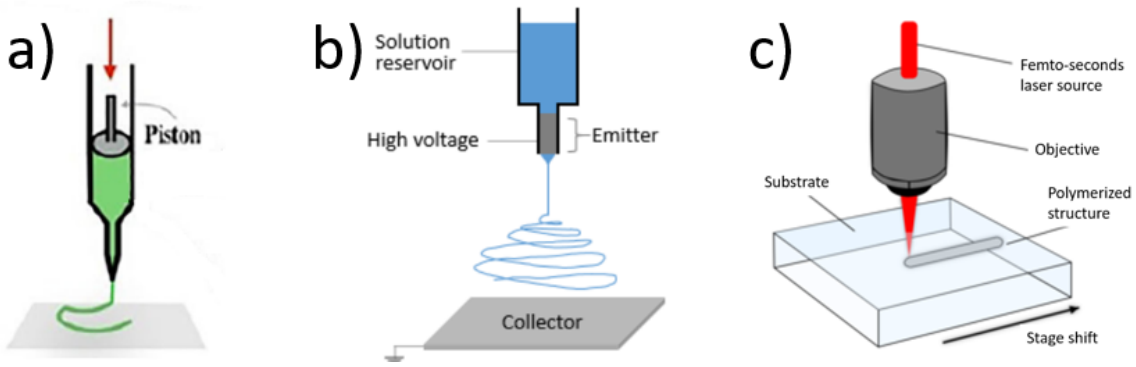

Figure 1.10: Additive manufacturing techniques for ***in vitro*** 3D cell culturing. **(a)** Extrusion based printing [41]. **(b)** Electrospinning setup [42]. **(c)** Schematic of 2PP writing process [43].

Extrusion based printing

In extrusion-based printing, a filament is extruded through a nozzle to create cross-sectional layers of a part using computer-aided design (CAD), enabling controllability of three-dimensional structures and rapid prototyping [44, 45](fig. 1.10a). This technique is classified as an additive manufacturing (AM) technique and applied in the tissue engineering industry for its ability to directly print organic material into the desired 3D configuration [46], such as hydrogel based vascularized tissue printing [41], or biocompatible polymers through fused deposition modeling (FDM) [44]. However, this technique provides low fabrication speed, on a scale that is undesirable for microglia culturing (mesoscale mm-cm and macroscale >cm), as this scale does not have the desired effect on microglia morphology as compared to nanopatterning which is on the nanoscale. Additionally, the minimal feature size (smallest size of a printable line) is limited by the nozzle diameter, resulting in both the resolution (smallest movement the laser/printer can make) and feature size (both >150 μm [41, 47]) not being of the desired accuracy.

Electrospinning

This method is a good first effort to create a structure that resembles the fibrous environment of the brain ECM. Fibrous scaffolds are created through the usage of a liquid polymer resin, that is pumped through a nozzle on which an electrical potential is applied. This electrical potential creates an electric field between the nozzle tip and the collector. This electric field in turn creates an electrostatic repulsive force on the surface of the liquid, and when this force is higher than the surface tension of the liquid, the charged liquid is ejected towards the collector. During the flight time, when the liquid is ejected towards the collector, the solvent is evaporated and a solid fibre remains [42, 48] (fig. 1.10b). The smallest feature size is dependent on the diameter of the fibre, which can be both micro- or nanofibers. This technique also allows the fabrication of meso- and macroscale scaffolds. Although the fibre diameter can be precisely controlled, no spatially controllable complex 3D structures can be produced with this technique as the collected fibres are randomly oriented [49]. This results in the pore size not being uniform, inhibiting cell penetration in the scaffold [49].

Two photon polymerization

Two-photon polymerization, also known as two-photon lithography, is a direct-laser writing (DLW) AM technique that employs liquid photosensitive material and polymerizes said liquid through photon absorption by laser light exposure [50] (example of 2PP setupfig. 1.10c). This AM technique enables rapid prototyping using CAD with high controllability of the spatial features in three dimensions. Moreover, 2PP displays a smaller feature size (<200 nm [51, 52]) than the aforementioned techniques, which in combination with CAD software enables better design repeatability and part consistency. Disadvantages are a limited amount of off-the-shelf photosensitive biocompatible materials and a high production time.

Comparison of techniques

When comparing the techniques based on the smallest feature size, resolution, the scale of the scaffold, and the 3D controllability of the desired design, it is apparent from table 1.2 that 2PP is the most promising candidate for the manufacturing of 3D scaffolds for culturing primary microglia cells.

Table 1.2: Comparison of additive manufacturing techniques for cell culturing.

	Extrusion based printing	**Electrospinning**	**2PP**
Smallest feature size	150 μm [47, 41]	<100 nm [7, 48]	<200 nm [51, 52]
Resolution (smallest increment of movement)	150 - 600 μm [47]	-	500 nm [51]
Scaffold scale	meso/macro [41, 47, 45]	meso/macro [48, 49]	nano/micro/meso [50, 53]
3D controllability	yes	no	yes

1.3.2. Biocompatible Materials

In this section, we list suitable materials for 2PP fabrication of structures for ***in vitro*** microglia cell culturing in an overview. For the materials to be suitable, each has to be biocompatible. In other words, non-cytotoxic or bio-inert so that cells may attach to the structure and even proliferate. Additionally, for immunofluorescence imaging to be possible, these materials need to have a low autofluorescence at the wavelengths of the used fluorescent markers, else the cell and structure cannot be discriminated. Furthermore, ideally, the Young's modulus should be closely mimicking the stiffness of real brain tissue (≈1 kPa [23, 24]), while still allowing the fabrication of stable structures. The suitable materials for the 2PP technique can be categorized as polymers or hydrogels. Both the Young's modulus and fluorescence properties (e.g. excitation and emission peak) will be presented in table 1.3. A coating can also be applied as a third option, to increase cell adhesion and may isolate the cell from potentially cytotoxic materials as well.

Polymers

Polymers represent a multitude of materials usable for 2PP. Some of the IP series materials from Nanoscribe GmbH & Co. KG (a company that builds 3D printers that employ 2PP technology and provides the respective printable materials) are especially useful for culturing microglia cells as these materials are proven to be biocompatible. IP-Dip and IP-L780 are both used in tissue engineering. For example, IP-Dip was employed by

Accardo et al. (2017), to culture neuroblastoma cells. The Young's modulus of IP-Dip ranges from 0.75 - 3.5 GPa depending on the laser power and writing speed [54, 55]. IP-L780 was utilized by Olsen et al. (2013) for its biocompatible properties in the fabrication of a woodpile structure which enabled to direct the migration of monocyte-derived dendritic cells in a microfluidic chip [56]. The Young's modulus of IP-L780 ranges from 1 - 4.73 GPa depending on the laser power [57, 55] Both materials are biocompatible in the sense that no cytotoxicity was observed [58].

IP-S was employed by Kramer et al. (2020) to print a microfluidic AFM cantilever that enables precise fluid manipulation near or in cells through fluid pipetting. The Young's modulus of IP-S ranges from 4.2 - 5.11 GPa depending on the laser power [59, 60, 61]. This material is considered to be non-cytotoxic according to ISO10993-5 [59].

One of the newest IP materials from Nanoscribe is IP-Visio. This material is mainly implemented for research in cell culture, as this material displays low autofluorescence in the range of visible light with regard to other IP series, and is thus perfect for fluorescence imaging [62]. However, the smallest feature size is not as low as the IP-Dip variant. This material is classified as non-cytotoxic according to ISO10993-5 [62], and has a Young's modulus of around 1.5 GPa [63].

Polycaprolactone (PCL) & polylactic acid (PLA) are widely employed materials in the biomedical industry as well, mainly because of the biocompatibility of these two materials [64]. Furthermore, they provide high stiffness. PLA was used by Ongaro et al.(2019), for organ-on-chip and microfluidic applications, as this material provides optically transparent (92% in the visible spectrum) and biocompatible properties, which are desired for this application [64]. The Young's modulus ranges from 2.3 - 3.5 GPa [65, 66].

PCL displays a lower Young's modulus than IP-Dip, 0.25 - 0.44 GPa [67, 68], which shows more promise for fabricating biomimetic culturing environments. Moreover, this commercially available material is intrinsically not fluorescent [69]. However, both materials need a photoinitiator to initiate polymerization and this might affect the fluorescent properties as the photoinitiator requires light at a certain wavelength to be excited and thus might cause interference in immunofluorescence imaging at the same wavelengths. Furthermore, PCL/PLA blends exist that are both biocompatible and exhibit a Young's modulus lower than either of the two materials separately, 0.03 - 2.6 GPa depending on the PLA mass fraction of the blend [70, 71].

Hydrogels

Hydrogels are materials that mainly consist of water trapped by cross-linked chains of polymers. This entrapment of water, caused by the cross-linking and the hydrophilic nature of the polymers, is what provides the low Young's modulus in the kPa to MPa range [72]. Another advantage of hydrogels is that by increasing the degree of cross-linking (cross-link density), one can increase the Young's modulus [72]. Increasing the molecular weight of the cross-linking agent (or decreasing molecular weight of the polymer in the solution) allows for more inter-fibre space (space between fibres) which results in increased crosslink density (decrease in water absorption capacity) and an increase in material stiffness follows [73, 74]. The polymers implemented in hydrogels, are not intrinsically photosensitive and therefore need a photoinitiator to be usable for 2PP.

Polyethylene glycol diacrylate (PEGDA) is a hydrogel commonly used as a biocompatible material, capable of closely replicating the material stiffness of the brain. This material was used by Accardo et al. (2018) to fabricate woodpile structures for neuroblastoma cell cultures. Additionally, PEGDA was used by Ovsianikov et al.(2010), to print a sort of microwell structure for the culturing of endothelial cells. The Young's modulus can be influenced by changing the molecular weight of PEGDA present in the resin [72], which permits a material stiffness ranging between 100 - 3300 kPa [75, 76].

Another hydrogel that is worked with in the tissue engineering industry, is Gelatin methacryloyl (GelMA). This material is a biocompatible hydrophilic hydrogel consisting of gelatin, an organic material made out of collagen (a protein present in the ECM) [7], closely mimicking the stiffness of the brain (4.32 - 30 kPa)

enables high cell viability when used for cell culturing [77, 78]. Depending on the applied photoinitiator, the fluorescent properties might variate.

Although the low stiffness of hydrogels is favourable for tissue engineering and brain cell culturing, the low stiffness is a disadvantage when fabricating complex 3D structures as low stiffness materials often create structure instability under larger loads.

Table 1.3: Comparison of biocompatible materials.

	Young's modulus	**Excitation peak**	**Emission peak**
IP-Dip	0.75 - 3.5 GPa [54, 55]	405 nm [79]	478 - 480 nm [75, 79]
IP-L780	1 - 4.73 GPa [57, 55]	405 nm [80]	450 - 550 nm [80]
IP-S	4.2 - 5.11 GPa [59, 60, 61]	390 nm [62]	430 - 520 nm [62]
IP-Visio	1.5 GPa [63]	390 nm [62]	425 - 450 nm [62]
PCL(bulk)	0.25 - 0.44 GPa [67, 68]	-	-
PLA(bulk)	2.3 - 3.5 GPa [65, 66]	-	-
PCL/PLA	0.03 - 2.6 GPa [70, 71]	-	-
PEGDA	100 - 3300 kPa [75, 76]	375 nm [75]	480 nm [75]
GelMA	4.32 - 30 kPa [78, 77]	365 nm [81]	unknown

Biochemical Coatings

To increase the cell viability and adhesion to the structure, a coating could be applied post-process. The coatings should consist of materials that are present in the brain ECM, to mimic the biochemical cues of the environment. Commonly used coatings for increased cell viability, are glycoprotein based, such as fibronectin, laminin, collagen IV, and vitronectin. These proteins adhere to proteins in the cell membrane [7]. MaxGel ECM Hydrogel is a more promising candidate. Although it is an ***in vitro*** human cell-derived basement membrane extract and consists of ECM components derived from skin tissue [82], it consists of a combination of glycoproteins (e.g. collagens, laminin, fibronectin, tenascin and elastin), proteoglycans and glycosaminoglycans [82] and is, therefore, better than just using a single material as a biochemical coating (the brain has multiple glycoproteins as well).

The coating thickness might have a negative effect on the nanopatterning if the layer is too thick. When using laminin the coating is thin enough for the cells to detect the underlying surface topography [75]. This is true for fibronectin and vitronectin as well, but not for collagen IV and gelatin. This is because, for the first three, only a single molecular layer is present. As for the last two, the layer thickness increases with increased exposure to water, as both materials absorb water [83, 84]. Taking this into account and knowing that laminin is a low cost and easily acquirable material, the decision was made to use this material as a biochemical coating for the cell experiments.

Material choice

Firstly, to be able to print complex structures of choice and culture-sensitive microglia cells, the decision was made to use IP-Dip due to the sheer amount of data that is already available on this material, making the interaction with cells predictable. Also, this material is proven to be biocompatible and already used with other cells (neuroblastoma cells). Furthermore, due to the relatively high material stiffness, this material allows for complex 3D structures and structural instability is kept at a minimum. Combined with the 2PP technology, it is possible to print small features in the nanometer range, making it possible to integrate nanofibre and nanopillar sized objects/structures to interact with the microglia cells. Additionally, this materials autofluorescence in the green channel can be used to identify the structures during fluorescence imaging.

Secondly, the decision to use laminin as a biochemical coating was easy due to its ability to increase cell adhesion. Besides, this material is relatively cheap and due to it being a single material, the concentration is easier to control as compared to the MaxGel ECM Hydrogel, of which the constituents variate between batches. in addition, the thin layer of laminin (monolayer) will not interfere with the structural effects of the desired structures.

1.4. Research question and project plan

1.4.1. Research question

Using the structural features of the created microstructures combined with their respective surface topography to develop an ***in vitro*** culturing model wherein primary ramified microglia cells can be cultured that resemble microglia ***in vivo***, results in the following problem statement:

In light of the mentioned limitations of the current ***in vitro*** microglia culture models due to the scarcity of studies on primary microglia coming from humans or primates, we can summarize the research question of this project in the following way:

"Is it possible to culture ***in vitro*** primary ramified microglia cells that mimic microglia ***in vivo*** by controlling the stiffness and surface topography of an engineered 3D micro-scaffold?"

To find an answer to the above-mentioned research question, a series of sub-research questions can be set up to break down the statement into smaller pieces to make it easier to find a solution:

- What is the effect of nanopatterning on microglia cell morphology?
- What is the effect of material stiffness on microglia cell morphology?
- What is the effect of a post-processing biochemical coating on microglia cell morphology and its viability?
- Do ***in vitro*** microglia when cultured on 3D structures, mimic the morphology of ramified ***in vivo*** microglia?

1.4.2. Project plan

The project is divided into several parts in order to keep an overview: the structure fabrication process, the cell culturing and imaging part, and the data analysis part. We provide a graphical representation in fig. 1.11 of the research process steps that are followed for the fabrication of each structure and the respective cell culture and analyses that follow. After a structure is fine-tuned, determined non-cytotoxic by employing a sacrificial cell culture, and the microglia cells are successfully cultured, the process restarts at the structure design phase for the new structure in line.

The structure choices are described here below, with a short description of its function. Also, the biochemical coating laminin is added to increase cell adhesion and to see the effect on microglia behaviour as compared to uncoated structures.

1. **Pedestal (2D):** Acts as a control surface for the comparison between microglia cells cultured on a flat IP-Dip substrate and the surface reference, the fused silica substrate. An area of 500 μm x 500 μm should be large enough for statistical analysis of cells while keeping the printing time of the structure as low as possible.
2. **Micropillars (2.5D):** The first 2.5D structure that is employed serves as an intermediate step for the nanopillar fabrication, as the dimensions of this design (a diameter of 1 μm and a length of 2.5μm) are not pushing the limits of the 2PP technique. It is expected that it will be easier to fabricate this design as compared to the nanopillars.
3. **Nanopillars (2.5D):** This design is the desired goal for the 2.5D structures. The diameter is set to 200 nm, in order to replicate nanometric dimensions of the brain's ECM. Additionally, the length of 2.5 μm should provide a reasonable reduction in the effective shear modulus while still providing enough structure stability to not collapse during the development procedure. The expectation is that the bending pillars cause a decreasing effect on the stiffness of the material as sensed by the microglia cells, and thus make it possible to bypass the need for soft material for microglia culturing.
4. **Cage (3D):** This design is integrated into the project to see how the microglia cells will react to a 3D ***in vitro*** environment. The cubical structure was chosen with a width between 25 and 50 μm to allow cell penetration and high visibility inside the cage from all sides, as well as the ease of adaptability and possibility to link multiple structures together for larger arrays (for future studies). The round beams were chosen to be 5 μm, as this shape and dimension enable the primary branches to wrap around

the beams in an easier way as compared to square beams, providing a more evenly distributed force exerted by the cell on the structure.

5. **Cage with micropillars (3D):** The micropillars are integrated into the cage as an intermediate step before nanopillar integration and to identify any problems beforehand.
6. **Cage with nanopillars (3D):** Finally, the nanopillars are integrated into the cage. This design is expected to provide a better representation of the 3D environment of the brain as compared to the normal cage due to the nanoscale dimensions added. Also, the same pillar bending effect in the 2.5D case is expected to reduce the stiffness of the structure as sensed by the microglia cell.

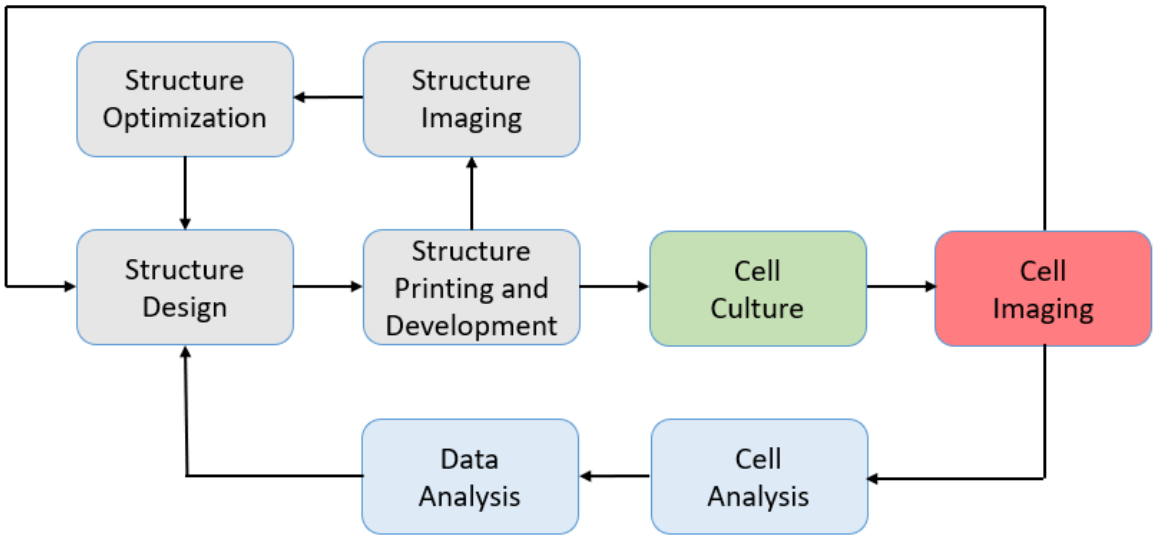

Figure 1.11: Project planning. Grey depicts structure fabrication process, green the cell culture, red the cell imaging part and blue the cell and data analysis.

2

Methodology and Materials

In this section, we provide a description of the structure design, the utilization of two-photon lithography, the machine that applies this technique and the corresponding material implemented for the development of microglia cell culturing scaffolds. Also, we show a simplistic flowchart of the fabrication process of the structures in fig. 2.1. Furthermore, we describe in detail the cell lines put into practice combined with a flowchart (fig. 2.7) and a detailed explanation of the cell handling processes. We continue with the description of the imaging techniques employed for the imaging of cells and structures. Lastly, we provide an overview of the cell analysis methods used in this project.

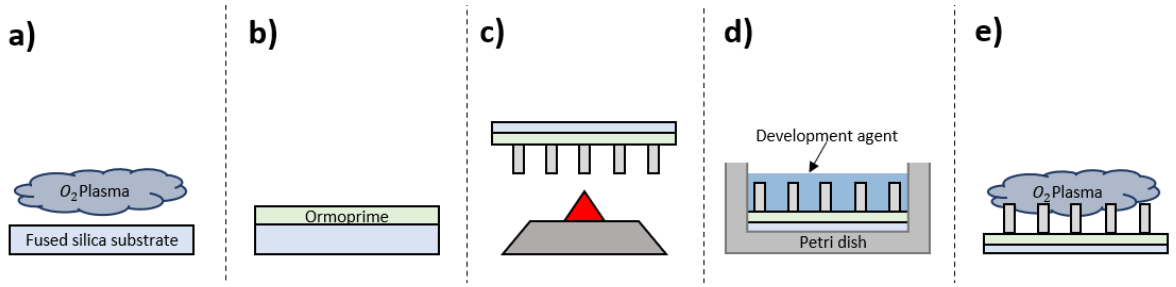

Figure 2.1: Fabrication process of structure: **(a)** Oxygen plasma cleaning of substrate, **(b)** added Ormoprime coating by spin coating, **(c)** 2PP printing of the structures, **(d)** development of structure, **(e)** oxygen plasma functionalization of substrate surface.

2.1. Structure Design

The structures intended for the cell culturing part were designed using SOLIDWORKS 2019 (DS SolidWorks Corp.), a 3D CAD modelling software. A step-by-step structure fabrication plan was followed in order to create a nanopillar decorated 3D structure. Firstly, a pedestal (2D structure) was designed to act as a control surface to indicate the differences between microglia cultured on a flat fused silica substrate and microglia cultured on a flat surface made out of IP-Dip. The parameters that are of importance for the design of the 2D structure are the length (l), the height (h) and the width (w) (fig. 2.2a). This was followed by the fabrication of the 2.5D pillar structures to see the effect of the reduced effective shear modulus (with respect to the bulk modulus) on the microglia morphology behaviour. Here the variable parameters are the pillar diameter (d), the pillar height (h) and the gap between pillars (p) (fig. 2.2b). Lastly, the 3D cage was printed with and without nanopillar decoration. Here the parameters that play a role in the design are the height (H), the width (W), the beam diameter (D), the angular spacing between pillars (ϑ), the lateral spacing between pillars (δ), see fig. 2.3. The same parameter symbols are applied for the pillar diameter (d) and the pillar height (h). The chosen dimensions for each structure type are shown in section 3.1.

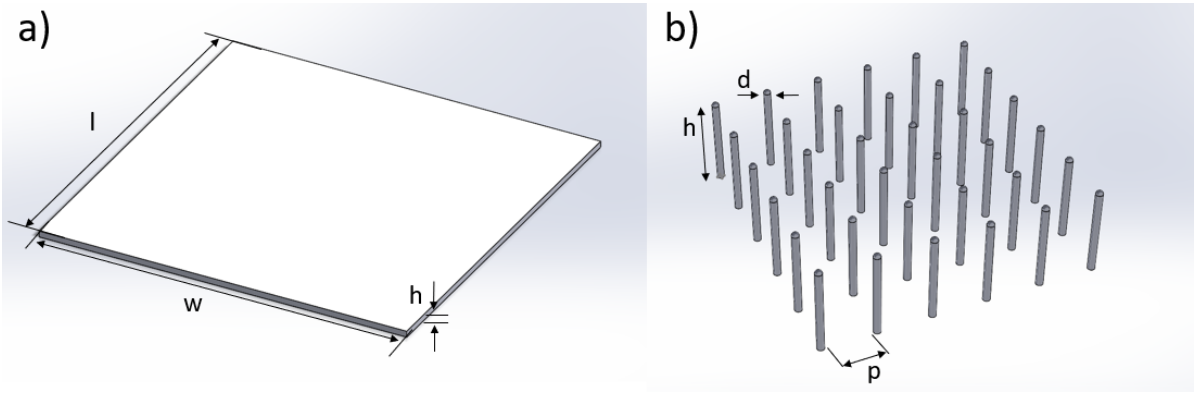

Figure 2.2: (a) Pedestal (2D) design, l represents the length, h represents the height and w represents the width. **(b)** 2.5D pillar array design, d represents the pillar diameter, h the pillar height and p the spacing between pillars.

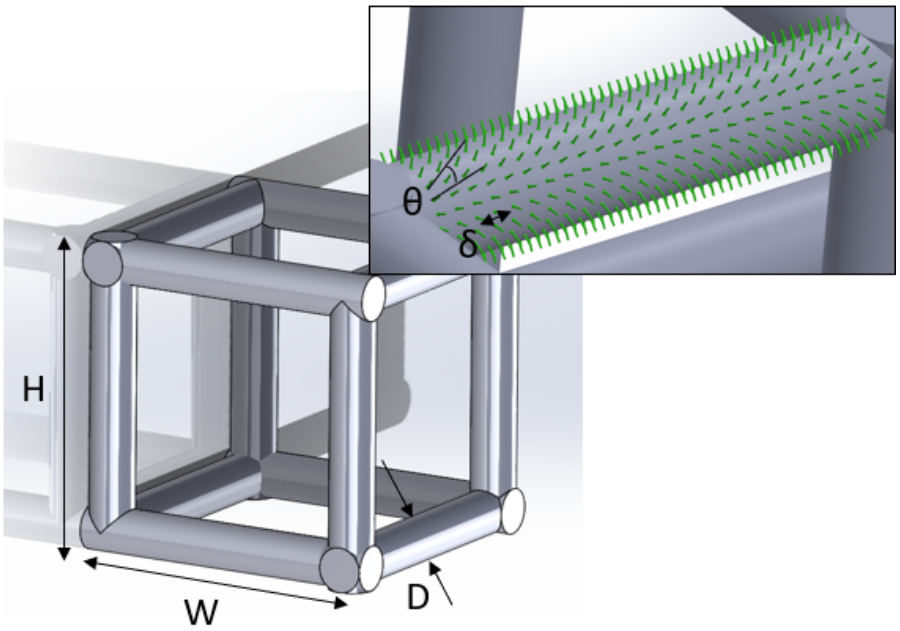

Figure 2.3: Cage design with nanopillar decoration. H represents the height, W represents the width, D represents the beam diameter, ϑ represents the angular spacing between pillars and δ represents the lateral spacing between pillars.

2.2. Structure Fabrication Process using Two-Photon Lithography

The fabrication of the structures was performed by employing two-photon lithography technology. This technique was chosen because of the advantages it has with respect to traditional photon polymerization. One of the advantages is that the feature size of 2PP is smaller than that of traditional photon polymerization. Traditional one-photon-polymerization uses ultraviolet (UV) light photons to cross-link, i.e. solidify the photosensitive material. Whereas, in 2PP, two photons, each featuring twice the wavelength (IR) but half the energy of UV light, are employed. Shooting two photons in the focal spot of the IR-transparent resin, by using a laser with a pulse width of 100 femtoseconds, leads to the excitation of the same energy transition as UV photons employed in traditional one-photon polymerization [53]. But the difference is a significant decrease in the voxel size (the polymerized part of the sample in the focal spot) for the 2PP technique (see fig. 2.4b). The three main components of a photosensitive resin are: a monomer, a solvent, and a photoinitiator which is a molecule that creates reactive species (e.g. free radicals) upon exposure to radiation. When the photoinitiator is exposed to light, the free electron and thus the molecule becomes excited (higher energy state), the photoinitiator becomes a free radical that breaks the double bond of the carbon atoms present in the monomer, thus becoming a radical monomer. The radical monomer binds to other monomers and creates a polymer chain [53], see fig. 2.4c for the chemical process. The chain linking terminates when two chains

combine to form a dormant bigger chain [87].

Project set up

For this project, we employed the Nanoscribe Photonic Professional GT+ setup, with a Ti:sapphire femtosecond pulsed laser working at a wavelength of 780 nm. Furthermore, a 63x objective with a numerical aperture of 1.4 was operated in Dip-in Laser Lithography mode (DiLL) (DiLL configuration seen in fig. 2.4a), in order to polymerize the negative tone resist IP-Dip resin(acrylate-based polymer) provided by Nanoscribe. As said earlier, SOLIDWORKS 2019 (DS SolidWorks Corp.) enabled designing the structures of choice. Then, the 3D models were imported into Describe as .stl files (using the "import stl" tool) which is the printing preparation software of Nanoscribe GmbH [89]. Within Describe, the 3D model is divided into horizontal and vertical slices, which is called slicing and hatching respectively. The slice thickness is what determines the resolution of the printed 3D model and are indicated by the slicing distance and hatching distance for the horizontal and vertical slices respectively [89]. Also, in this program, other printing parameters can be changed to optimally print the structure's dimensions as close as possible to the intended ones. The printing parameters consist of the laser power with a maximum power of 50 mW, which is controllable by using a percentage of the maximum power. The scanning speed (or writing speed) of printing is controlled by the moving speed of the moving stage or the galvo mirrors. By controlling the angle at which the mirror reflects the laser, the position of the focus spot of the laser can be controlled. Controlling the galvo mirrors is called Galvo mode, and this mode is put in practice for the fabrication part for its higher printing speed as compared to the moving stage (PIEZO mode) which enables a higher resolution print but takes significantly more printing time. When printing structures with an area greater than 130 μm x 130 μm, stitching of the structures is needed, which is the smooth transition of overlapping printing areas controlled by the block overlap and shear angle. Also, a parameter exists called the interface position that controls the depth at which the voxel is printed with respect to the surface of the substrate. The parameters that were just mentioned, all have an effect on the linewidth or smallest feature size of the printed structure. The linewidth can be further decreased than the 200 nm given by Nanoscribe, through post-processes such as pyrolysis or plasma etching [50]. This is dependent on the printing material, and also on the combination of the following processing parameters: laser power, writing speed and exposure time. As can be seen in fig. 2.5, when the laser power is increased, the voxel size increases as well. Furthermore, the same is true for increasing the exposure time.

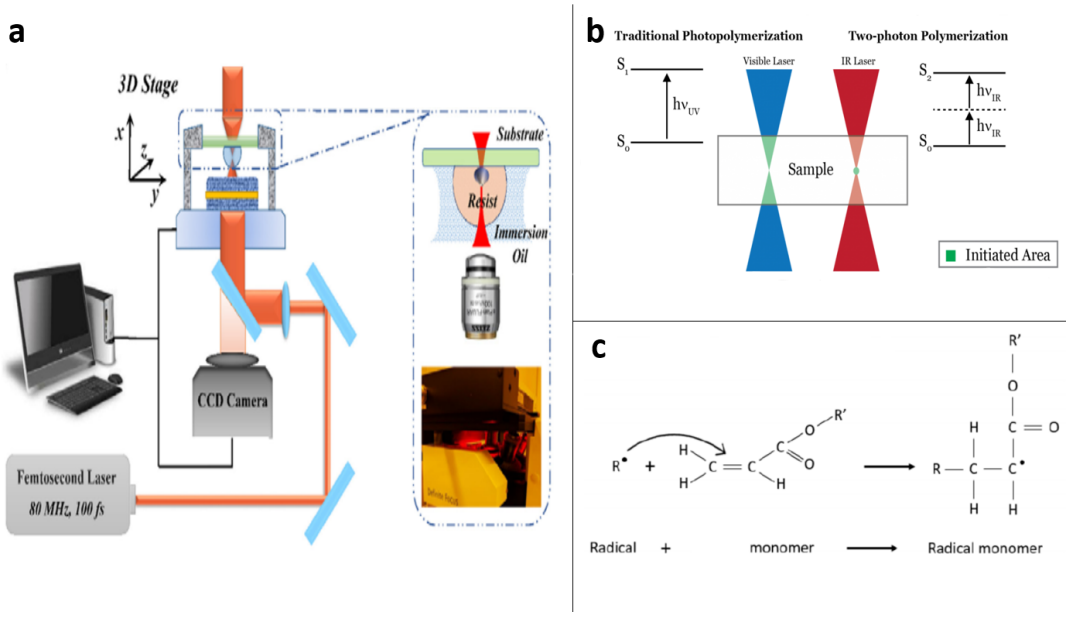

Figure 2.4: **(a)** 2PP setup in DiLL mode. **(b)** Traditional photopolymerization vs. 2PP, electron excitation is done in 1 step vs. 2steps for 2PP. **(c)** Polymerization process initiated by a radical and a monomer. Adapted from [85, 86, 50].

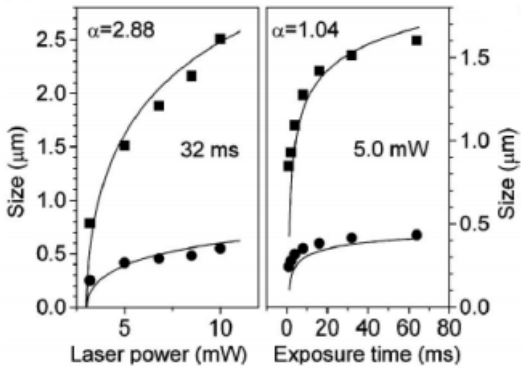

Figure 2.5: Relation between voxel size and laser power, and voxel size and exposure time [88].

Substrate preparation

In preparation for printing, the fused silica substrate (the elastic modulus is ≈ 72 GPa [90]) was first cleaned with a fine cloth covered with some acetone, secondly cleaned with the same fine cloth and some isopropanol (IPA), and then dried with an air-drying gun to remove dust from the surface. Hereafter, the cleaned sample went into the Diener oxygen plasma cleaner (fig. 2.1a), which cleaned and functionalised the surface of the sample for 5mins at 80W (80% of an RF max power of 100W) with a gas flow rate of 5 sccm. Depending on if the attachment of the structures to the fused silica substrate was sufficient, an OrmoPrime® 08 (micro resist technology GmbH) coating of around 130 nm was additionally added (fig. 2.1b), by spin-coating followed by post-baking to harden the coating (see appendix A.3 for the full process). Finally, after the cleaning steps and the added OrmoPrime®08 coating (OC) (if applicable), the fused silica substrate was placed into the sample holder, and one droplet of IP-Dip resin was deposited in the middle of the substrate before going into the Nanoscribe.

Development procedure

Once the printing process was finished, the substrates with polymerized structures were carefully placed horizontally in a borosilicate Petri dish filled with propylene glycol methyl ether acetate (PGMEA, from SIGMA-ALDRICH) for 25 min to remove the unpolymerized resin (fig. 2.1d). This was followed by submersion in a Petri dish with IPA for 5 min to rinse off excess PGMEA. And lastly, submersion for 30 s in Novec 7100 Engineered Fluid (SIGMA-ALDRICH), which has lower surface energy than IPA resulting in a decrease of collapsed nanopillars caused by wet-to-dry transitions. The development optimization procedure is reported in appendix A.3.

Post-processing

Post-processing of the IP-Dip structures was done, while again using the Diener oxygen plasma cleaner for 20 seconds at 80W with a gas flow rate of 5 sccm (fig. 2.1e). This would additionally functionalise the polymer surface as oxygen bonds are broken, enabling chemical bonds with the cell membrane in an attempt to increase the attachment of the cell to the structure. A different application of the Diener oxygen plasma cleaner was to use plasma etching in an attempt to smooth out the shape of the pillars and change dimensions after printing. However, the results were unsatisfactory and required further optimization.

Material Young's modulus

In order to test and confirm the material's Young's modulus, a series of four compression tests were completed using the Femtotools (fig. 2.6a and b). The compression test was performed at a compression distance (distance of indentation/compression)/deflection of 10% of the material height. The flat silicon tip, model FT-S200,000, has a 50 μm x 50 μm tip size and a force range of ± 200,000 μN.

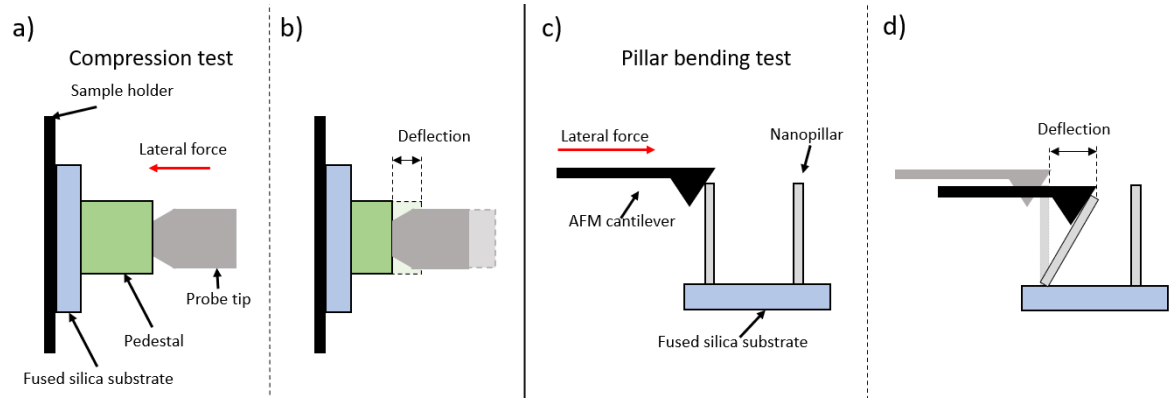

Figure 2.6: Schematic of the compression test using the Femtotools. **(a)** Femtotools probe tip applies a lateral force on the pedestal. **(b)** Deflection of pedestal caused by the applied force of probe tip. Schematic of the AFM pillar bending test: **(c)** AFM probe tip applies a lateral force on the nanopillars. **(d)** Deflection of nanopillar caused by the applied force of AFM tip.

A secondary method of determining the Young's modulus was performed to rule out instrument measurement errors. This was accomplished with an atomic force microscope (AFM) pillar bending test (fig. 2.6c), using the cantilever tip to bend the nanopillars (cantilever stiffness 14.4 N/m) (fig. 2.6d), resulting in a force vs. displacement diagram from which the structure's spring constant can be derived [91]. Using beam deflection theory, and assuming a cylindrical shaped cantilever beam with an external force at the tip, the material's stiffness was experimentally obtained by Dr. Livia Angeloni. The results of both the compression test and the pillar bending test are in the results section, whereas the raw data is in appendix B.2.

2.3. Cell culture

In this section, we describe the employed cell lines and cell donors and also explain the cell handling protocols such as the isolation, sterilization, and culturing procedures. Furthermore, we show a simplified flowchart of the cell culturing process in fig. 2.7.

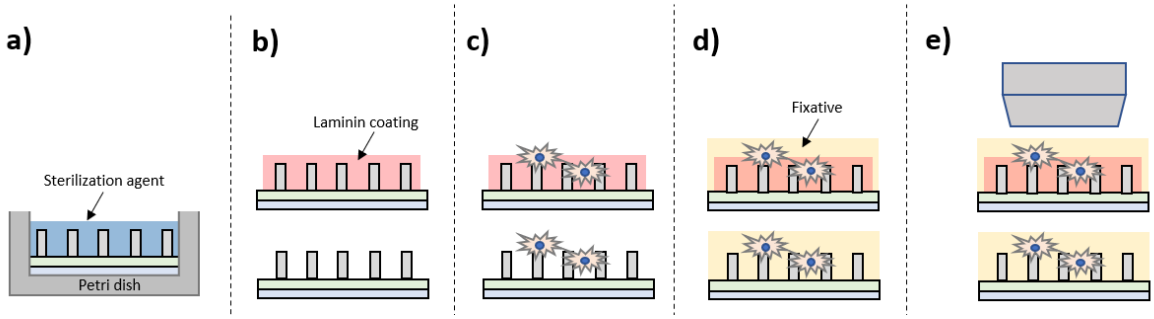

Figure 2.7: Cell culturing process: **(a)** sterilization of substrate and structures, **(b)** added laminin coating if applicable, **(c)** cell seeding and culturing, **(d)** fixation of cells, **(e)** imaging of cells.

2.3.1. Cell Lines and Animal Donors

THP-1 cells

THP-1 cells are human-derived monocytes, that can be differentiated into macrophages through specific culture methods. These cells were employed to see if the IP-Dip material was cytotoxic and to see if complications arose with the structures during the cell culture or cell seeding part. The reasons for the implementation of these cells are that this cell line is quite resilient to changes in the environment, are easy to acquire and are relatively cheap.

Animal Donors

Primary microglia were derived from isolated brain tissue (white matter) that was obtained from adult rhesus macaques (Macaca mulatta) without neurological disease, that became available from the outbred breeding colony. No animals were sacrificed for the exclusive purpose of the initiation of microglia cell cultures. Better use of experimental animals contributes to the priority 3Rs program of the Biomedical Primate Research Centre. The overview of donors can be seen in table 2.1.

Table 2.1: Overview of animal donors

Isolation date	Donor	Age (years)	Gender	Weight (kg)	Origin
20-07-20	R07007	13	F	7.6	India
17-08-20	R07110	13	M	10.7	India
09-11-20	R01068	19	M	13.1	India
03-12-20	R17045	3	M	7.85	India
18-01-21	R15059	5	F	4.6	India
15-02-21	R09153	11	M	17.4	India

2.3.2. Cell Handling Protocols

In this section, we provide an accurate description of the used cell handling protocols. The descriptions will be about the microglia cell isolation, the sterilization protocol of the fused silica substrate, laminin coating application protocol, and lastly the culture protocol for both the THP-1 and the microglia cells.

Microglia Cell Isolation Protocol

Primary cell cultures were isolated as follows: In short, microglia isolations were initiated from cubes of ~4.5 g frontal subcortical white matter tissue that were depleted of meninges and blood vessels manually. The tissue was chopped into cubes of less than 2 mm^2 by using gentleMACS ^{TM} C tubes (Miltenyi Biotec, Bergisch Gladbach, Germany) and then incubated at 37°C for 20 min in PBS containing 0.25% (w/v) trypsin (Gibco Life Technologies, Bleiswijk, The Netherlands) and 1 mg/mL bovine pancreatic DNAse I (Sigma-Aldrich, Saint Louis, MO) and mixed every 5 min. The supernatant (liquid lying above a solid residue after precipitation or centrifugation) was discarded (no centrifugation), the pellet (solid mass consisting of cells and other tissue) was washed and passed over a 100 μm nylon cell strainer (Falcon; Becton Dickinson Labware Europe) and centrifuged for 7 min at 524 g. The pellet was re-suspended in 22% (vol/vol) Percoll, 37 mM NaCl and 75% (vol/vol) myelin gradient buffer (5.6 mM NaH_2PO_4, 20 mM Na_2HPO_4, 137 mM NaCl, 5.3 mM KCl, 11 mM glucose, 3 mM BSA Fraction V, pH 7.4). A layer of myelin gradient buffer was added on top, and this gradient was centrifuged at 1561 g for 25 min (minimal brake). The pellet was washed and centrifuged for 7 min at 524 g. After this final step one is left with a mixture of microglia cells and red blood cells.

Sterilization Procedure

The substrates were sterilized as follows: The substrates with or without structures were transferred to a 6-well plate. Then, the substrates within the 6-well plate were washed twice for 5 minutes with a high volume (~4 mL/ well) of 70% EtOH. Finally, the substrates were washed five times for 1 minute with sterile demi-water or PBS (fig. 2.7a). If applicable, the biochemical coating laminin is applied to the fused silica substrate (fig. 2.7b) before the cell seeding according to the following procedure:

Laminin coating application procedure

The laminin coating was applied in the following manner: A 10 μg/mL working solution of laminin (Sigma-Aldrich) was prepared in DMEM/F-12 (Gibco). Then, the laminin solution was added to cover the entire growth surface of the fused silica substrate (~500 μL/substrate). For uncoated substrates, DMEM/F-12 (Gibco) was added to cover the entire growth surface of the fused silica substrate (~500 μL/substrate). The substrates were then incubated at 37°C and 5% CO_2 for 2 hours (do not let the laminin solution evaporate). The freshly coated substrates were then used for further experiments.

THP-1 Cell Culture Procedure

THP-1 cells were treated with 100 nM phorbol 12-myristiate-12 acetate (PMA; Sigma-Aldrich) and plated at a density of 50,000 cells/cm^2 on either uncoated or laminin-coated substrates (with/without structures) in THP-1 medium, which comprised of RPMI 1640 supplemented with 10% (v/v) FBS (TICO Europe, Amstelveen, The Netherlands), 2 mM GlutaMAX, 1 mM nonessential amino acids, 1 mM sodiumpyruvate, 50 units/mL penicillin and 50 μg/mL streptomycin (all from Gibco). Followed by incubating the cells at 37°C in a humidified atmosphere containing 5% CO_2. After 3 days, the medium was replaced with a fresh THP-1 medium (without PMA). Cells were kept in culture for 5 days total without passaging (the removal of the medium and transfer of cells).

Cell culture method for microglia cells

Primary microglia cells were plated at a density of 50,000 cells/cm^2 on either uncoated or laminin coated substrates (+structures,fig. 2.7c) in SM medium comprised of 1:1 v/v DMEM (high glucose)/HAM F10 Nutrient mixture (Gibco) supplemented with 10% v/v heat-inactivated FBS (TICO Europe, Amstelveen, The Netherlands), 2 mM glutamax, 50 units/mL penicillin and 50 μg/mL streptomycin (all from Gibco). After overnight incubation at 37°C in a humidified atmosphere containing 5% CO_2, the unattached cells and debris were removed by washing with PBS twice and replaced by fresh SM medium supplemented with 20 ng/mL

(≥ 4 units/mL) M-CSF (PeproTech, London, UK). At day 4, cells were washed twice with PBS and replaced by serum-free microglial (SFM) culture medium comprised of DMEM/F12 (Gibco) supplemented with 0.5 mM glutamax, 50 units/mL penicillin, 50 μg/mL streptomycin, 5 μg/mL N-acetyl cysteine (Sigma-Aldrich), 5 μg/mL insulin (Sigma-Aldrich), 100 μg/mL apo-transferrin (Sigma-Aldrich), 100 ng/mL sodium selenite (Sigma-Aldrich), 20 ng/mL (≥ 4 units/ml) M-CSF, 12.5 ng/mL TGF-β (Miltenyi Biotec, Bergisch Gladbach, Germany), 1.5 μg/mL ovine wool cholesterol (Avanti Polar Lipids, Alabaster, AL), 1 μg/mL heparan sulfate (Galen Laboratory Supplies, North Haven, CT), 0.1 μg/mL oleic acid (Cayman Chemical, Ann Arbor, MI), 1 ng/mL gondoic acid (Cayman Chemical). All cells were kept in culture for a total of 15 days without passaging. From day 4, half of the medium was replaced by a fresh SM medium containing new growth factors every 2–3 days.

2.4. Imaging

In order to inspect both the fabricated structures and the cell behaviour, a total of 3 imaging techniques were wielded. The SEM imaging technique was employed for high-resolution imaging of both the cells and structures and the inverted fluorescent and confocal microscope were used to discriminate between cell membranes using immunofluorescent imaging. Here below we elaborate on the usage, instrument specifications and additional processes needed.

2.4.1. Scanning Electron Microscopy

The Jeol JSM-6010LA Scanning Electron Microscope (SEM) was used in high-vacuum SEI mode with an accelerating voltage of 10 kV and magnification range X5 - X15,000, to make high-resolution images for visual inspection of the fabricated structures and cell cultures (fig. 2.7e).
Gold sputtering of the polymeric/IP-Dip structures was necessary as the material is not electrically conductive enough for SEM imaging. Using the sputter coater JEOL JFC-1300 auto-fine coater on auto mode, the sample was kept in an argon-filled chamber at 0.5 mbar at a distance of 25 mm away from the gold crucible with a current of 20 mA. The deposition rate of ~ 0.7 nm/s, for 30 s resulted in a 15-20 nm gold layer. When 45°tilted photos were deemed necessary, the sample was kept in a 45° sample holder and sputtered an additional two times. A non-standard fixation protocol was conducted combining paraformaldehyde (PFA), glutaraldehyde (GA) and hexamethyldisilazane (HMDS) (fig. 2.7d). The reason is that the normal fixation protocol using both PFA and GA on cells cultured on both micro-/and nanopillars caused cell membrane ruptures, and applying HMDS during drying reduced this. The optimization process for the HMDS drying can be found in appendix A.7.

PFA fixation

The PFA fixation was applied in the following way: First, the medium was removed and the cells were washed twice with PBS (Gibco). Then the cells were fixed with 2% PFA (Affymetrix, Santa Clara, CA) in PBS for 30 min at room temperature. Lastly, the PFA was removed and the cells were washed with PBS twice.

GA fixation

In order to prepare for SEM imaging, the following GA fixation protocol was performed: First the PFA fixated samples were post-fixed with 2% GA (Agar Scientific, Stansted, UK) in PBS for 2 hours. Then the fixative was removed and the samples were dehydrated in distilled water for 2x 5 min, followed by 50% EtOH in distilled water for 15 min, 70% EtOH in distilled water for 20 min, and lastly in 96% EtOH in distilled water for 20 min. Then the ethanol was removed from the sample and allowed to dry in HMDS (Sigma-Aldrich): Firstly, 2 parts of 96% EtOH were used on 1 part HMDS for 15 minutes. Secondly, 1 part of 96% EtOH on 1 part HMDS for 15 minutes. Thirdly, 1 part of 96% EtOH on 2 parts HMDS for 15 minutes. Then only HMDS for 20 minutes, twice. Lastly, most of the HMDS was removed and the sample was air-dried for 2 hrs.

2.4.2. Immunofluorescent imaging

The fluorescent images were taken using two different microscopes, an inverted fluorescent microscope and a confocal microscope. We describe the methods here below.

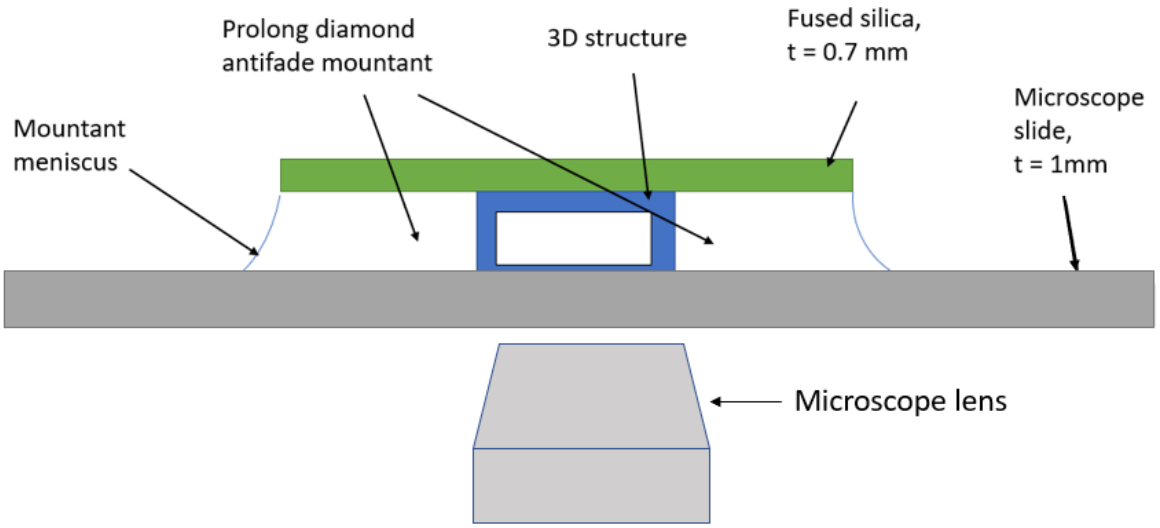

Figure 2.8: Setup of the inverted fluorescent microscope sample. The structure is in-between the fused silica substrate and the microscope slide.

Inverted Fluorescent microscope

The experimental setup depicted in fig. 2.8 is the inverted microscope, in which the fused silica slide with the printed 2D/3D structure is mounted onto a microscope slide with Prolong™ Diamond Antifade mountant (needed to stick the fused silica slide with cells to the microscope slide). Images were acquired using a Leica DMI6000 fluorescence microscope and LASX software. This setup, however, resulted in lower quality images of the cells on top of the pedestals as compared to the images from the confocal microscope, so instead, confocal imaging was applied.

In vitro trypan blue staining

The trypan blue staining was carried out in order to perform a live/dead assay on the THP-1 and microglia cells to determine cell viability. The cells grown on substrates were washed with PBS for 3 minutes. 0.2% Trypan Blue solution (Sigma-Aldrich) was added to cover the entire growth surface of the substrate and incubated for 2 min at room temperature (RT). The Trypan blue solution was removed and rinsed 3-4 times with PBS with gentle shaking until the PBS was clear of any residual blue colour. Cell viability was analyzed using an Olympus CKX41SF Inverted Phase Contrast Microscope.

Immunofluorescence staining

To visualize individual cells, both the cell membrane and nuclei needed to be stained. Therefore, cells grown on substrates were fixed for 30 min at room temperature in 2% PFA, washed with PBS and PBS + 0.02% Tween20 respectively, and a-specific binding was blocked by incubation for 30 min in PBS containing 2% normal goat serum. To be able to detect the cell membrane, samples were incubated overnight at 4°C with CX3CR1 (a protein that binds to the cell membrane) (or CD11b for THP-1 cells) in antibody (1:400, Abcam, Cambridge, UK) in PBS containing 0.1% BSA, washed with PBS + 0.02% Tween20, and incubated for 1h at RT with goat anti-rabbit Alexa 647 (1:250, Jackson ImmunoResearch Laboratories, Weste Grove, PA) (red channel) in PBS containing 0.1% BSA. For the inverted fluorescent microscope, after extensive washes with PBS, substrates were mounted using ProLong™ Diamond Antifade + 4',6-diamidino-2-phenylindole (DAPI, Thermo Fisher Scientific), a blue fluorescent DNA stain used for cell nuclei staining. The PFA fixation protocols are the same as described above in the SEM section.

Confocal microscopy

For the confocal images, the Leica SP5 confocal microscope was used in combination with the respective Leica software. The channels that were observed were blue, green and red and the excitation wavelengths were 405 nm, 488 nm and 633 nm. The Objective used was the 507701, Leica Microsystems GERMANY HCX

APO L 20.0 X1.00 WATER lens with a working distance of 1.95 mm, in water dipping mode. The setup for the samples using the confocal microscope can be seen in fig. 2.9.

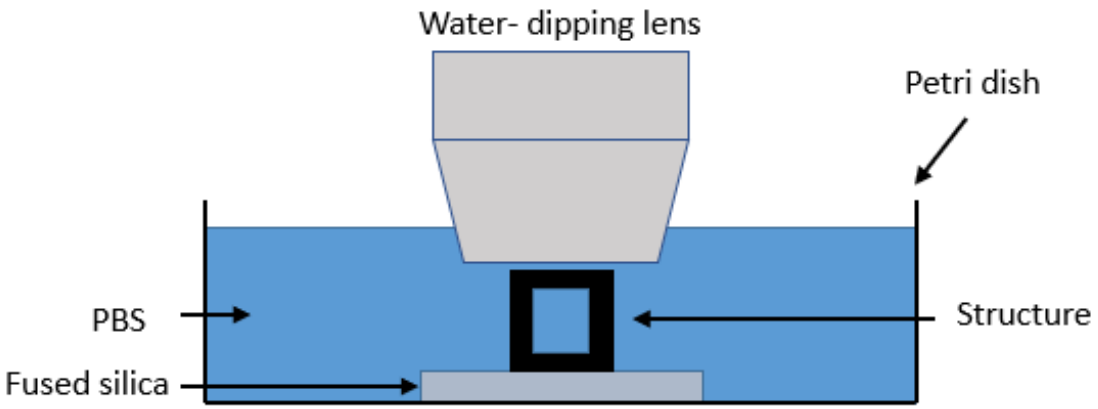

Figure 2.9: The configuration for the confocal microscope, using a 20x immersion lens in water-dipping mode. The structure on the fused silica substrate is submerged in a petri dish filled with PBS.

Immunofluorescence staining

The cells grown on substrates were fixed for 30 min at room temperature in 2% PFA, washed with PBS and PBS + 0.02% Tween20 respectively, and a-specific binding was blocked by incubation for 30 min in PBS containing 2% normal goat serum. Samples were incubated overnight at 4°C with CX3CR1 antibody (1:400, Abcam, Cambridge, UK) in PBS containing 0.1% BSA, washed with PBS + 0.02% Tween20, and incubated for 1h at RT with goat anti-rabbit Alexa 647 (1:250, Jackson ImmunoResearch Laboratories, Weste Grove, PA) (red channel) in PBS containing 0.1% BSA. For the confocal microscope, after extensive washes with PBS, the substrates were incubated in 2 μM Hoechst 33342 (Thermo Fisher Scientific™, blue fluorescent dye with excitation wavelength range: 361-497 nm, emission wavelength range: 460-490 nm) for 10 min, washed with PBS twice and then stored in PBS. The PFA fixation protocols are the same as described above in the SEM section.

2.5. Cell Analysis Methods

The analysis of the cells is divided into quantitative and qualitative analysis methods and we describe both here below.

Quantitative analysis

To determine if a certain structure or coating does promote more ***in vivo*** behaviour or provides more ramified cells, the following aspects are investigated:

1. **The phenotype distribution** is quantified by visual inspection and manual counting of the cells present in the fluorescent images. Using the multi-point selection tool (ImageJ) it is possible to select and add a colour code to the nuclei or a specific phenotype and the ROI (region of interest) manager function (ImageJ) stores that data, as shown in fig. 2.10. This produces an accurate quantification of the cell phenotypes and nuclei.

   For this project the following colour codes were used:

   (a) Red: nuclei
   (b) Orange: flat amoeboid cells
   (c) Cyan: bi-polar cells
   (d) Magenta: globular cells
   (e) Green: non amoeboid cells
   (f) Black:ramified cells

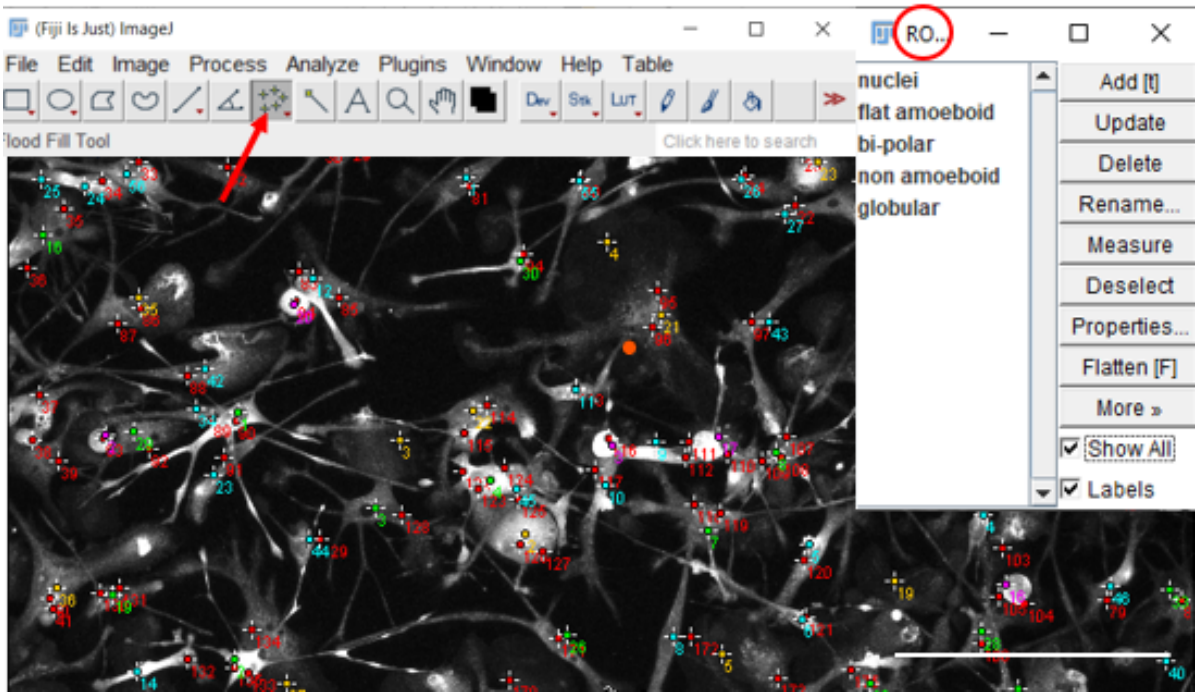

Figure 2.10: Phenotype selection using ImageJ's multi-point selection tool (red arrow) to select and give colours to, and ROI manager window (encircled in red) to store selections, scale bar 180 μm.

2. **The degree of ramification** is a method to define how ramified or complex a ramified cell is (more branches with ramifications equals a more complex cell). This was determined by the morphological analysis of around 3-5 ramified cells for each sample, by employing the Sholl analysis algorithm (ImageJ) on both SEM and immunofluorescence images. First, the perimeter of the cell was traced with the Neurite tracer (ImageJ) tool and skeletonized. Then, using the Sholl analysis, concentric circles were drawn around the centre of the cell (see fig. 2.11), with a radial increment of 5 μm. This tool measures the number of intersections the perimeter of the cell has at each concentric circle. The number of intersections is plotted against the distance from the cell centre. A high amount of intersections translates to a high degree of ramification of ramified cells. A graph showing a steep peak at a distance of 10 - 40 μm from the centre, is usually an indication of a ramified cell with a relatively small soma (5 - 20 μm) and multiple branches. Sholl plots mainly tell something about the morphological complexity (how many ramifications has the cell) of a cell, and can be used to confirm if manually picked cells are indeed ramified cells. The plot should look like a spike at the beginning with multiple intersections, indicating a small soma with multiple primary processes. But the possibility might exist that a cell exists with a morphology that is not ramified but still shows the Sholl plot of a ramified cell. Therefore, this analysis method should only be applied to cells that are known to be ramified as this method is not reliable enough to be used as a phenotype identifier.

3. **The area under the curve (AUC, of the Sholl plot)** analysis for ramified microglia cells, is an additional indicator that might be helpful in determining the complexity/degree of ramification of a ramified cell. Normally a higher AUC means a more complex cell (more ramifications), but cells with long processes and no ramifications also have a high AUC value as these cells also occupy a large area. Therefore, this method should only be used in addition to the Sholl plot, as a verification of a more complex ramified cell and not on other phenotypes.

4. **The number of primary processes** of a ramified cell is also an indication of a cell being more ramified than cells cultured under different conditions, where a higher amount is desirable. The counting of these primary branches was performed manually by the implementation of the multi-point selection tool (ImageJ) on the same cells that were administered for the Sholl analysis.

5. **Cell occupancy on 3D structures** was assessed to see if the added micro-/nanopillar decoration on the 3D structures had any effect on the location of the cells within the 3D structures with respect to

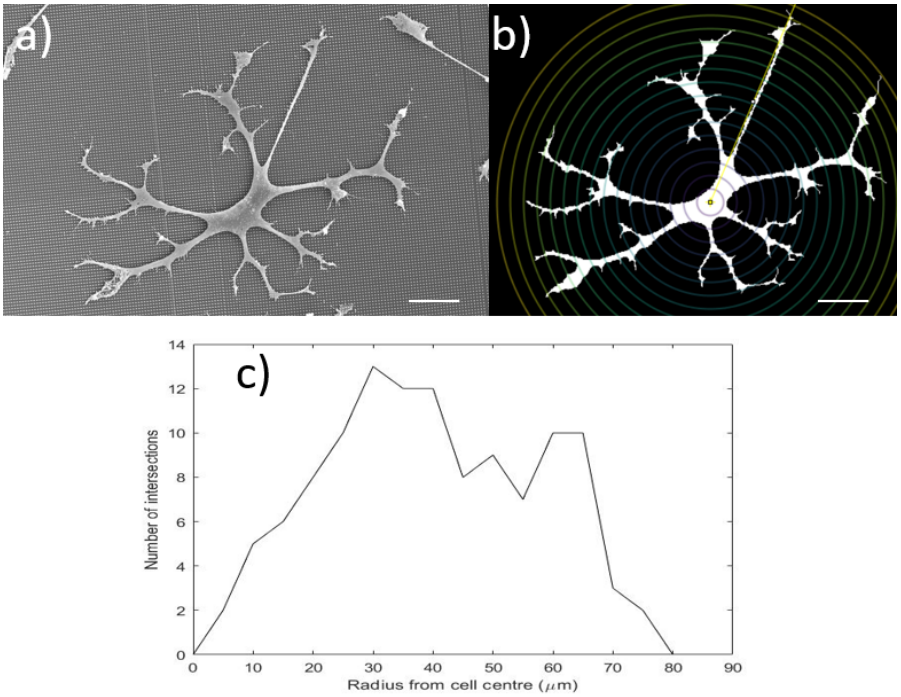

Figure 2.11: Process using Sholl analysis: **(a)** SEM image of a ramified cell (scale bar 20 μm). **(b)** Cell traced and skeletonized with Neurite tracer tool and concentric circles drawn using Sholl analysis (scale bar 20 μm). **(c)** Output graph of the Sholl analysis, showing the number of intersections on the y-axis against the distance of the drawn concentric circles from the soma (cell centre) on the x-axis, with a high peak close to the soma indicating a ramified cell.

undecorated 3D structures. The cells were counted in the fluorescent images using the multi-point selection tool (ImageJ) and using MATLAB (coding software), a self-made algorithm was made to count the cells per cage analogous to the height of the cage, which was divided into steps of 15 μm (range 0-60 μm).

Qualitative analysis

A qualitative analysis was performed on the cells cultured on the 3D structures (cages). Through visual inspection of the SEM and 3D rendered fluorescent images, using Imaris viewer, the following aspects were inspected:

1. **Cell phenotype morphology in a 3D environment (cages)**. The morphology of microglia cells in a 3D environment is inspected visually. We will be looking for similarities and differences in phenotype morphology between 2D and 3D cultured cells, to see if for example flat amoeboid cells (2D culture) also reoccur on 3D structures or take on different cell morphology, or if ramified cells extend their primary branches in multiple directions or remain planar.
2. **Filopodia interaction with 2D, 2.5D and 3D (also with micro-/nano decoration) structures.** It is known that filopodia play a role in sensing the stiffness of the environment. Through visual inspection of SEM images, the differences and similarities between filopodia interacting with flat surfaces, 2.5D and 3D structures will be documented to see if the structure type has an effect on the morphological behaviour of the cell.

2.6. Risk prevention

At the beginning of this project, we identified the following possible problems that might have occurred during fabrication of the scaffolds, during the seeding of the cells, or concerning imaging.

Adhesion problem of structure to substrate:

Increasing the adhesion of structures can be solved by:

1. Coating the substrate with Ormoprime (silanization technique), increases the adhesion of the IP-Dip structures to the substrate through chemical bonds.
2. Optimizing the interface position value (printing depth of laser with respect to substrate), enables a greater contact area of the printed voxel with the substrate.
3. Plasma treatment of the surface.
4. Increasing the surface area of the structure in contact with the substrate.

Structure instability for very thin beams:

This problem arises when combining a high writing speed with low laser power. This problem can be solved by introducing a single layer pedestal of a certain thickness, to act as a strong foundation on which the structure can be built. This may promote adhesion between structure and substrate, as the total contact area is increased, and thus increasing the probability of fabricating a stable structure. Furthermore, an adaptation of the structural designs, towards a more shear force resistant design may solve this problem as well. Also, building a cage of a larger beam thickness around the smaller beam diameter microcage, will result in a more stable structure.

Warping of the fabricated structure:

Can be caused by uncontrolled shrinkage of the structure when exposed to an abrupt change of wet to dry environment. This can be solved by using different solvents that evaporate at slower rates or fabricate structures in a controlled environment in which the structure slowly adapts to the desired environmental conditions (this is similar to critical point drying).

Coating technique affecting the nanopatterning effect:

If the applied coating is thick enough, it may pose problems to the nanopatterning effect of nanostructures, as the cells will not be able to sense the nanopatterning. This is probably not the case when using laminin, as this coating is only a single molecule thick.

Culture contamination:

Careful handling of the microglia cultures is necessary to prevent contamination by external sources. Thorough disinfection of structures and scaffolds, pre-culturing should prevent this problem. Also, some of the photo-initiators in unpolymerized resin are cytotoxic and can cause cell death, thorough rinsing of the substrate is needed to solve this problem.

Fluorescence imaging:

The intrinsic fluorescent properties of the chosen materials might influence the fluorescence microscopy images more than foreseen. Implementing confocal microscopy or 2-photon microscopy might solve this.

3

Results & Discussion

In this chapter, the results will be divided into two sections: the section 3.1 will show the fabrication of Polymeric Micro/Nano-Structures using Two-Photon-Polymerization, describing the final printed structures used for cell culture. Section 3.2 will provide an overview of the Cell Behaviour on Micro-Engineered Structures, describing if the adoption of micro-/nanopillars on 2D surfaces and 3D structures, with or without a laminin coating, positively affects the morphology of primary microglia cells.

3.1. Fabrication of Polymeric Micro-/Nanoscale Structures using Two-Photon Polymerization

In this section, the dimensions of the printed structures and the corresponding writing parameters used by the 2PP Nanoscribe machine are summed up. This is provided for the 2D, 2.5D (table 3.1), and for the 3D (table 3.2) structures:

- Pedestal (2D)
- Micropillars (2.5D)
- Nanopillars (2.5D)
- Cage 25 μm sides (3D)
- Cage 50 μm sides (3D)
- Cage 25 μm sides, micropillar decorated (3D)
- Cage 50 μm sides, micropillar decorated (3D)
- Cage 50 μm sides, nanopillar decorated (3D)

Furthermore, we summarize the detected issues that occurred during the fabrication process and the respective solutions.

3.1.1. 2D Structures: Pedestals

The pedestals that were printed and were ultimately involved in the largest part of the cell culture experiments differ from the initially designed model (Ped 1, see fig. 3.1 top row). This was a 390 μm x 390 μm area, consisting of an array of 3x3 individual blocks of 130 μm x 130 μm and 20 μm in height, with a gap between the blocks of 5 μm. The block area dimensions are the maximum allowable areas in Galvo mode and the respective gaps in-between the blocks were chosen so that stitching of the structures could be avoided, as this was believed to be less complex. The pedestal was printed with a laser power of 85% and writing speed of 60 mm/s at a hatching and slicing distance of 0.2μm, and interface position of 1 μm. The resulting dimensions were a width of 372 ± 1.07 μm, and a height of 19.4 ± 0.36 μm. The Young's modulus was measured to be 1.28 ± 0.18 GPa (N=4), by compression test with the Femtotools.

The final pedestal design (Ped 2, see fig. 3.1 bottom row) embodied a stitched area to increase structure uniformity as the Ped 1 design had the issue of individual blocks detaching from the array. The structure consisted of a 500 μm x 500 μm stitched area with a block shear angle of 17°, a block overlap of 2 μm, and a height of 5 μm. This larger area was chosen so that a higher number of cells could cover the area for a more statistical significant analysis. Also, the reduced height resulted in a reduced printing time. The design was printed

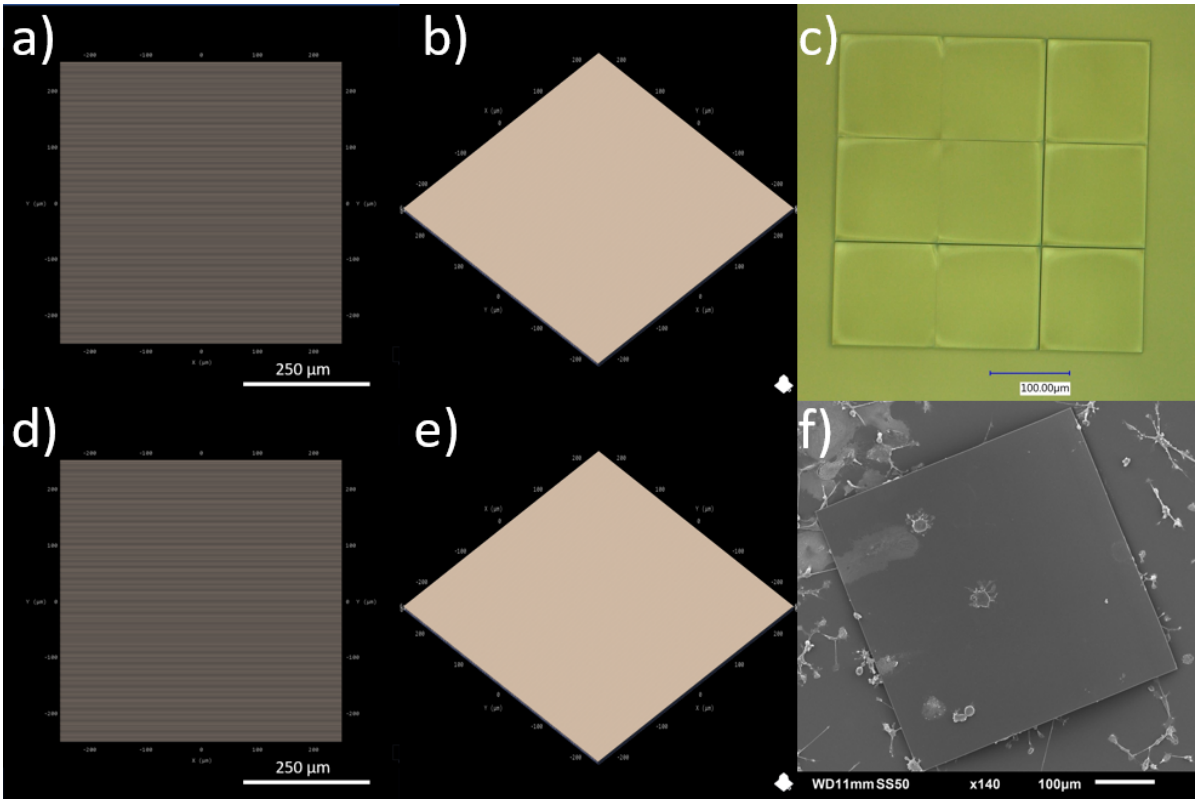

Figure 3.1: Images of: Ped 1 top view Describe model **(a)**, isometric view Describe model **(b)**, Keyance microscope image containing the isometric view of printed design **(c)**. Ped 2 top view Describe model **(d)**, isometric view Describe model **(e)**, SEM image containing the isometric view of printed design **(f)**.

with a 70% laser power, 30 mm/s writing speed, at a hatching distance of 0.2 µm, a slicing distance of 0.25 µm and an interface position of 1µm. These settings resulted in a width of 497 ± 5.00 µm and a height of 4.22 ± 0.07 µm. The Young's modulus was measured to be 0.87 ± 0.39 GPa (N=4), by compression test with the Femtotools.

Table 3.1: 2D and 2.5D structures: Overview of measured dimensions and printing parameters

	Ped 1	**Ped 2**	**MP 1**	**MP 2**	**NP 1**	**NP 2**
Width (μm)	374 ±1.07	497 ±5.00	485 ±0.77	493 ±1.40	495 ±1.53	497 ±1.80
Diameter (μm)	-	-	0.97 ±0.04	1.06 ±0.07	0.39 ±0.02	0.29 ±0.01
Height (μm)	19.4 ±0.36	4.22 ±0.07	1.97 ±0.04	1.87 ±0.05	1.90 ±0.07	1.82 ±0.06
Spacing (μm)	-	-	1.01 ±0.02	0.97 ±0.05	0.83 ±0.04	0.76 ±0.03
Laser power (%)	85	70	85	70	85	70
Writing speed (mm/s)	60	30	60	30	60	30
Hatching distance (μm)	0.2	0.2	0.2	0.2	0.2	0.2
Slicing distance (μm)	0.25	0.25	0.25	0.25	0.25	0.25
Estimated printing time	00:29:41	00:26:58	03:13:16	02:10:55	02:10:58	01:48:02
Effective shear modulus	-	-	11.4 (MPa)	11.9 (MPa)	911.5 (kPa)	204.8 (kPa)

3.1.2. 2.5D Structures: Micro- and Nanopillar arrays

The pillar arrays were designed to cover an area of 500 μm x 500 μm, in order to provide a sufficient area to culture microglia cells while keeping the printing time low. The micropillar array consisted of a 10 x 10 array of 25 x 25 micropillar arrays. Each pillar was designed to have a diameter of 1 μm, a 2.5 μm height and a spacing of 1 μm (minimum distance measurement). The first micropillar array (MP 1, see fig. 3.2 top row) was printed at a laser power of 85%, a writing speed of 60 mm/s, a hatching distance of 0.2 μm, and a slicing distance of 0.25 μm. These parameters resulted in an array width of 485± 0.77 μm, a pillar diameter of 0.97 ± 0.04 μm, a pillar height of 1.97 ± 0.04 μm, a spacing of 1.01 ± 0.02 μm, and an effective shear modulus of 11.4 MPa (≈ 115 times less than the bulk modulus of IP-Dip), calculated using eq. (1.1).
The final micropillar array (MP 2) was designed for the purpose of having the same printing parameters for all structures while optimizing the cylindrical shape. This new design was printed at a laser power of 70%, a writing speed of 30 mm/s, a hatching distance of 0.2 μm, and a slicing distance of 0.25 μm. This induced an array width of 493± 1.40 μm, a pillar diameter of 1.06 ± 0.07 μm, a pillar height of 1.87 ± 0.05 μm, a spacing of 0.97 ± 0.05 μm, and an effective shear modulus of 11.9 MPa (≈ 100 times less than the bulk modulus of IP-Dip), calculated using eq. (1.1).

The nanopillar array was also designed to cover a 500 μm x 500 μm area. It consisted of a 5 x 5 array made of an array of 86 x 86 nanopillars. The first version (NP 1, see fig. 3.2 middle row) was designed to be 0.2 μm in diameter, a height of 2.5 μm and also a spacing of 1 μm. Printing was done laser power of 85%, a writing speed of 60 mm/s, a hatching distance of 0.2 μm, and a slicing distance of 0.25 μm. The printed structure had an array width of 495 ±1.53 μm, a pillar diameter of 0.39 ± 0.02 μm, a pillar height of 1.90 ± 0.07 μm, a spacing of 0.83 ± 0.04 μm. By means of a pillar bending test using an Atomic Force Microscope, the Young's modulus was determined to be 1.80 ± 0.18 GPa, and an effective shear modulus of 911.5 kPa, calculated using eq. (1.1), which is 2,000 times less than the bulk modulus of the same material.
The final version (NP 2) was printed on top of Ped 2 (see fig. 3.1 bottom row), so that pillar collapse and

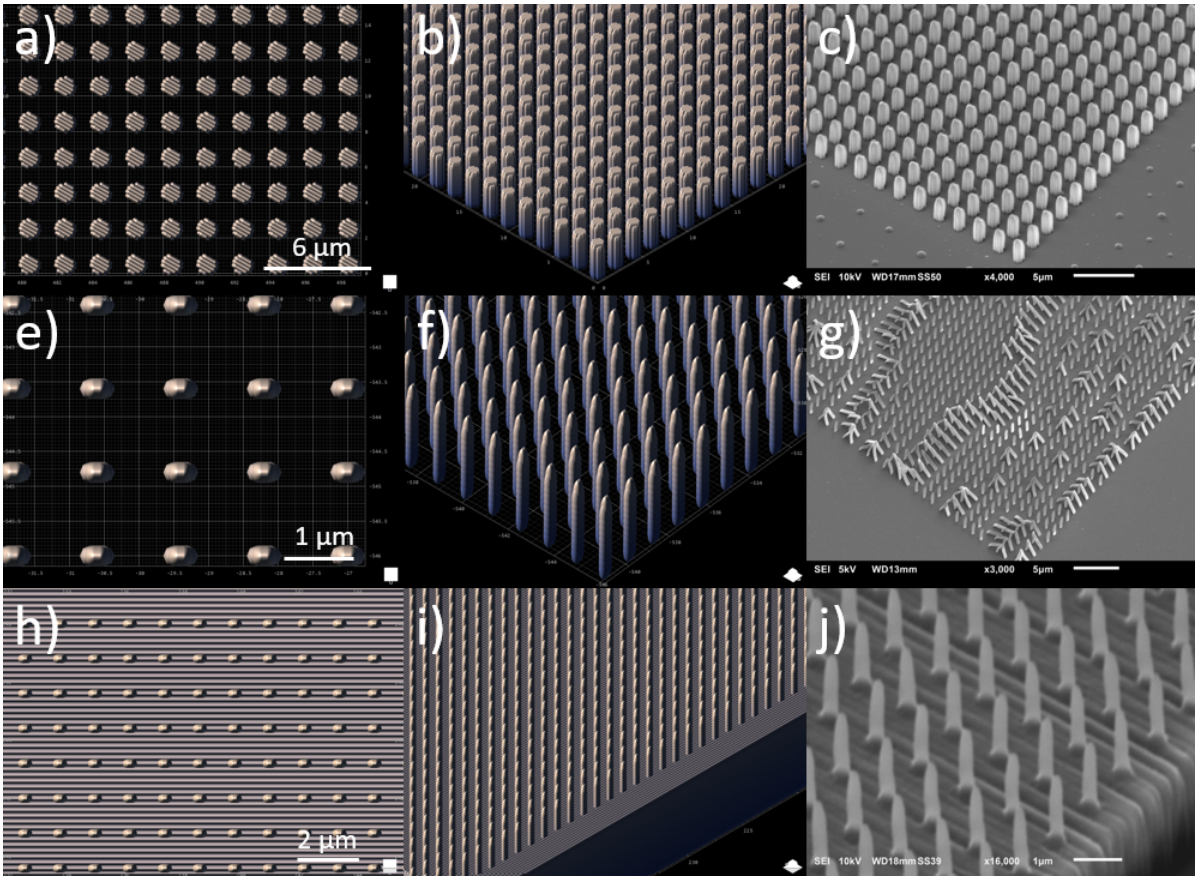

Figure 3.2: Graphical representation of the top view (Describe model), the isometric view (Describe model), and SEM image of the printed structure (isometric view): Micropillar array (MP 1) **(a, b, c)**. Nanopillar array (NP 1) **(d, e, f)**. Nanopillar array on pedestal (NP 2) **(g, h, i)**.

detachment during the development and cell seeding step could be kept at a minimum. This design was printed with a laser power of 70%, a writing speed of 30 mm/s, a hatching distance of 0.2 µm, and a slicing distance of 0.25 µm. The structure, when printed had an array width of 497 ± 1.83 µm, a pillar diameter of 0.29 ± 0.01 µm, a pillar height of 1.82 ± 0.06 µm, a spacing of 0.76 ± 0.03 µm, and an effective shear modulus of 204.8 kPa, calculated using eq. (1.1), which is around 4,250 times less than the bulk modulus of the same material (0.87 GPa).

3.1.3. 3D Structures: Cubic non- and Micro- /Nano-Decorated Cages

The printing and design process of the non-decorated 3D cages proved to be no hurdle. All cages were printed with a z-position offset of 2.5 µm so that the lower beam was cut in half to provide a higher contact area between the structure and substrate in order to increase attachment by surface forces. The 25 µm wide cages (SC, see fig. 3.3 top row) were designed to cover a 500 µm x 500 µm area in a 7 x 7 array, with a height of 25 µm and a beam diameter of 5 µm. The cage was printed using a laser power of 70%, a writing speed of 30 mm/s, a hatching distance of 0.2 µm, and a slicing distance of 0.25 µm. This resulted in an array width of 500 ± 0.92 µm, a cage width of 24.2 ± 0.09 µm, a beam diameter of 4.92 ± 0.05 µm, and height of 24.3 ± 0.04 µm.
The 25 µm wide cages with micropillar decoration (SC-MP, see fig. 3.3 second row) were also designed to cover a 500 µm x 500 µm area in a 7 x 7 array, with a height of 25 µm and a beam diameter of 5 µm, a pillar height of 2.5 µm, a diameter of 1 µm, an angular spacing of 30°, and a lateral pillar spacing of 1 µm. The cage was printed using a laser power of 70%, a writing speed of 30 mm/s, a hatching distance of 0.2 µm, and a slicing distance of 0.25 µm. This resulted in an array width of 499 ± 0.99 µm, a cage width of 24.1 ± 0.15 µm, a beam diameter of 4.90 ± 0.05 µm, a height of 23.7 ± 0.20 µm, a pillar diameter of 1.01 ± 0.04 µm, a pillar height of 2.20 ± 0.02 µm, an angular pillar spacing of 29.4 ± 0.22 °, and a lateral pillar spacing of 0.97± 0.02 µm.

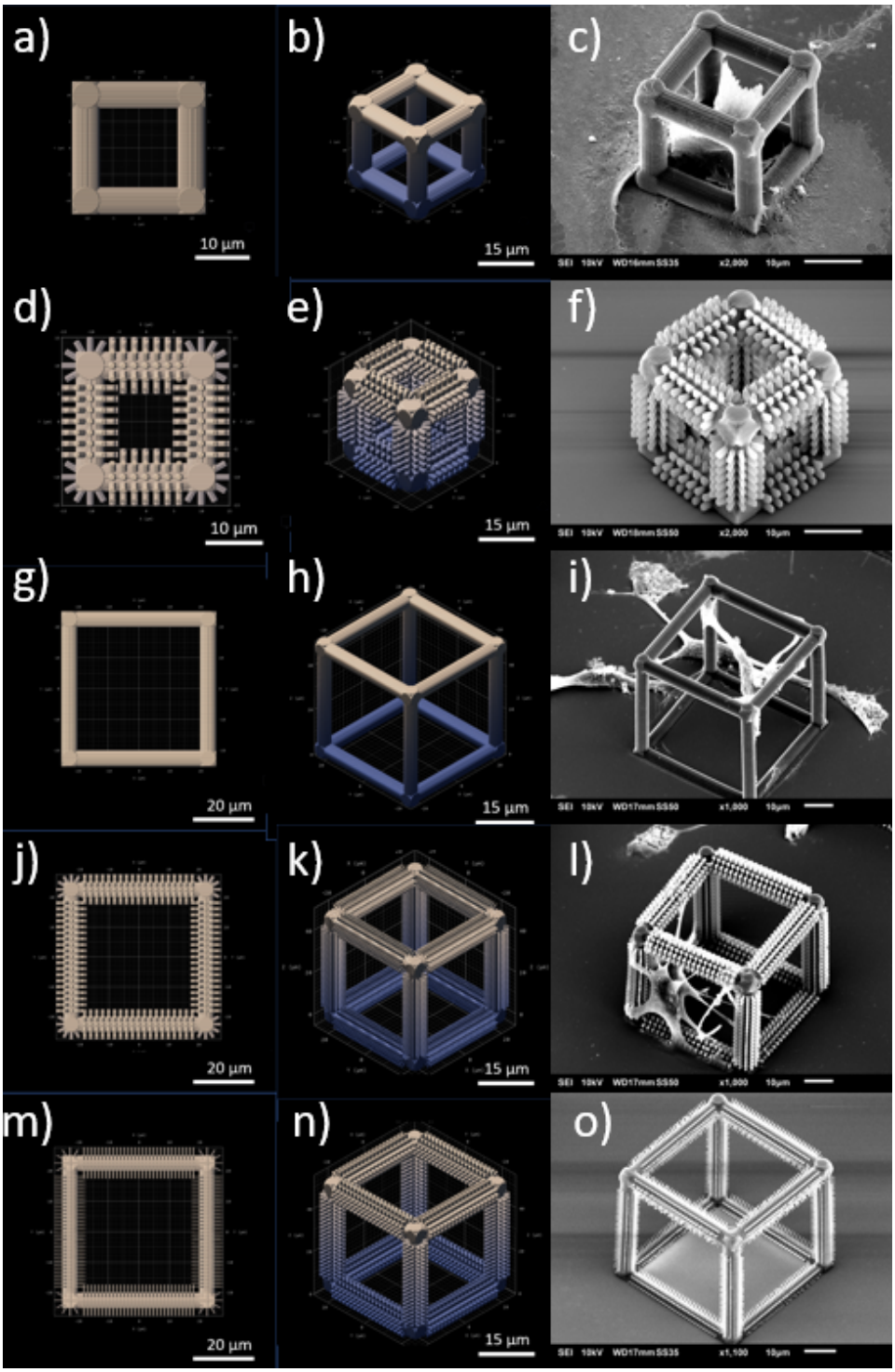

Figure 3.3: Graphical representation of the top view (Describe model), the isometric view (Describe model), and SEM image of the printed structure (isometric view): Small cage (SC) **(a, b, c)**. Small cage with micropillar decoration (SC-MP) **(d, e, f)**. Big cage (BC) **(g, h, i)**. Big cage with micropillar decoration (BC-MP) **(j, k, l)**. Big cage with nanopillar decoration (BC-NP) **(m, n, o)**.

Table 3.2: 3D structures: Overview of measured dimensions and printing parameters

	SC (25 μm) 7x7	**SC-MP 7x7**	**BC (50 μm) 5x5**	**BC-MP 5x5**	**BC-NP 5x5**
Array width (μm)	500 ±0.92	499 ±0.99	542 ±1.84	544 ±1.72	544 ±0.52
Width (μm)	24.2 ±0.09	24.1 ±0.15	49.0 ±0.07	46.9 ±0.44	46.1 ±0.33
Beam diameter (μm)	4.92 ±0.05	4.90 ± 0.05	4.98 ±0.05	4.75 ±0.06	4.89 ±0.03
Height (μm)	24.3 ±0.04	23.7 ±0.20	48.8 ±0.11	43.7 ±0.68	46.0 ±0.34
Pillar diameter (μm)	-	1.01 ±0.04	-	0.88 ±0.05	0.24 ±0.02
Pillar height (μm)	-	2.20 ±0.02	-	2.27 ±0.03	1.86 ±0.02
Angular spacing (°)	-	2.94 x 10 ±0.22	-	3.01 x 10 ±0.52	3.10 x 10 ±0.88
Lateral spacing (μm)	-	0.97 ±0.02	-	1.00 ±0.08	0.83 ±0.02
Laser power (%)	70	70	70	70	70
Writing speed (mm/s)	30	30	30	30	30
Hatching distance (μm)	0.2	0.2	0.2	0.2	0.2 (cage) 0.1 (NP)
Slicing distance (μm)	0.25	0.25	0.25	0.25	0.25 (cage) 0.2 (NP)
Estimated printing time	00:29:02	04:35:29	00:40:04	02:20:43	03:03:00

The 50 μm wide cages (BC, see fig. 3.3 middle row) were designed to cover a 550 μm x 550 μm area in a 5 x 5 array, with a height of 50 μm and a beam diameter of 5 μm. The cage was printed using a laser power of 70%, a writing speed of 30 mm/s, a hatching distance of 0.2 μm, and a slicing distance of 0.25 μm. This resulted in an array width of 542 ± 1.84 μm, a cage width of 49.0 ± 0.07 μm, a beam diameter of 4.92 ± 0.05 μm, and height of 24.3 ± 0.04 μm.

The 50 μm wide cages with micropillar decoration(BC-MP, see fig. 3.3 fourth row) were designed to cover a 550 μm x 550 μm area in a 5 x 5 array, with a height of 50 μm and a beam diameter of 5 μm, a pillar height of 2.5 μm, a diameter of 1 μm, an angular spacing of 30°, and a lateral pillar spacing of 1 μm (minimum distance). The cage was printed using a laser power of 70%, a writing speed of 30 mm/s, a hatching distance of 0.2 μm, and a slicing distance of 0.25 μm. This resulted in an array width of 542 ± 1.72 μm, a cage width of 46.9 ± 0.44 μm, a beam diameter of 4.75 ±0.06 μm, a height of 43.7 ± 0.68 μm, a pillar diameter of 0.88 ± 0.05 μm, a pillar height of 2.27 ± 0.03 μm, an angular pillar spacing of 30.1 ± 0.52 °, and a lateral pillar spacing of 1.00± 0.08 μm.

The most difficult part was the integration of the cage with the nanopillar decoration because the ideal printing parameters were different for the cage as compared to the nanopillars. So a compromise had to be found by reducing both the accuracy of the print with respect to the desired dimensions and the writing speed in order to have a printing parameter set that enabled the fabrication of the micro/nano-decorated cage. Two solutions were identified to enable the integration of pillars onto the cage structure:

1. Print complete structure with the same printing parameters directly (both pillars and cage)
2. Print cage and pillars separately (sequentially) with 2 different .stl files (one .stl file for each structure, see fig. 3.4)

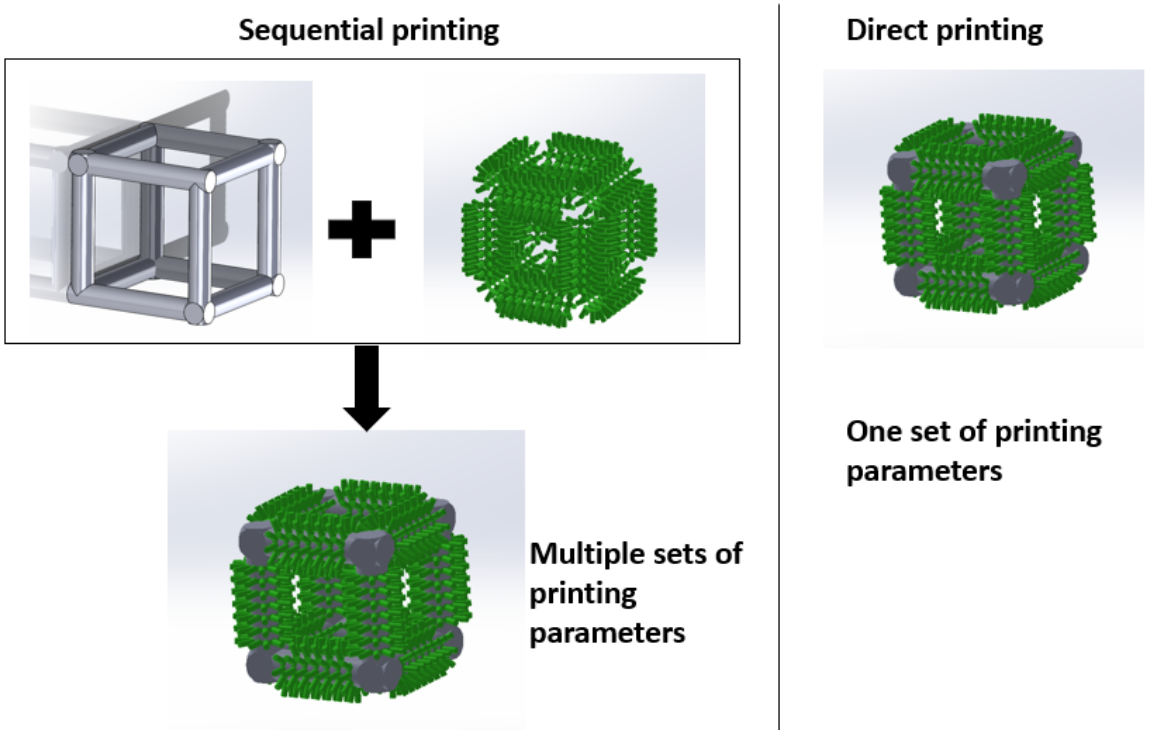

Figure 3.4: Sequential and direct printing of decorated cage.

The problem of the first solution was that both pillars and cage were printed with the ideal printing parameters of the cage resulting in undesired dimensions for the pillars. Solution 2 on the other hand provided individual tweaking of the printing parameters of the pillars. However, for this second method, the already printed top of the cage caused shadowing meaning that the laser could not reach certain positions underneath the top of the cage, resulting in unprinted pillar structures on the vertical beams and underneath the top of the cage. This problem was solved by printing the top, the vertical beams and the bottom, with the respective pillar decoration in steps (see fig. 3.5).

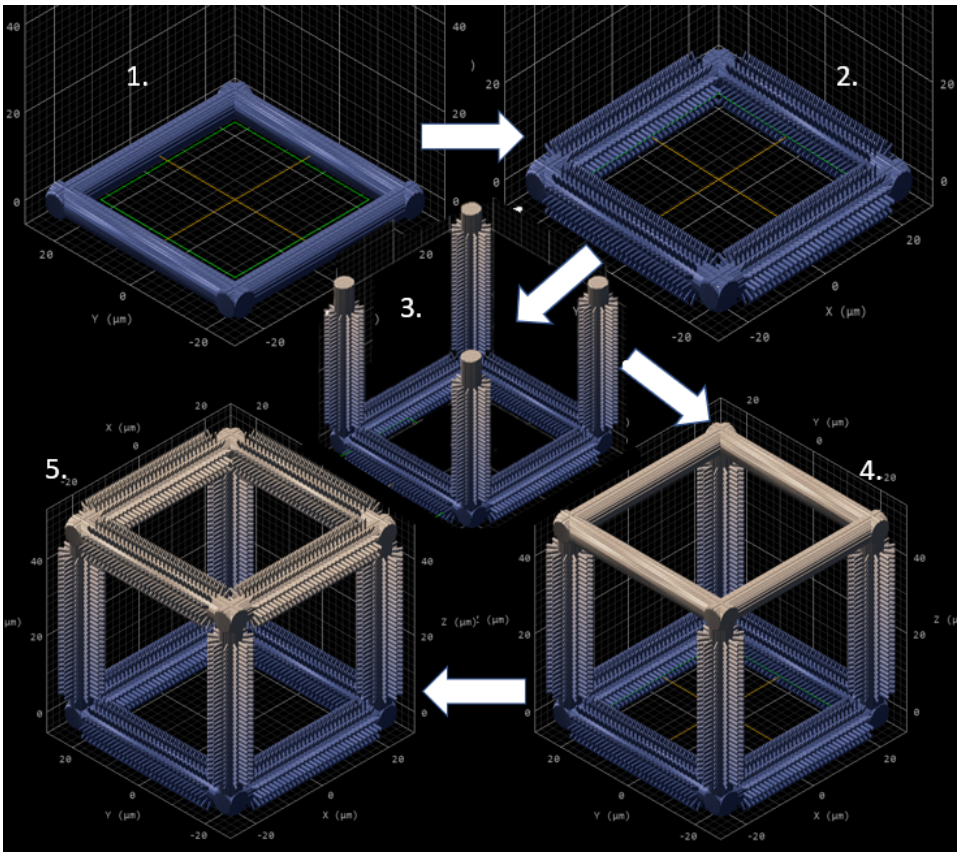

Figure 3.5: Final sequential printing technique, using 5 steps. 1) Base printed. 2) Pillars printed on the base. 3) Vertical beam with pillars printed. 4) Top printed. 5) Pillars printed on the top.

Using the new printing approach, the 50 µm wide cages with nanopillar decoration(BC-NP, see fig. 3.3 bottom row) were designed to cover a 550 µm x 550 µm area in a 5 x 5 array, with a height of 50 µm and a beam diameter of 5 µm, a pillar height of 2.5 µm, a diameter of 0.2 nm, an angular spacing of 30°, and a lateral pillar spacing of 1 µm (minimum distance). The cage was printed using a laser power of 70%, a writing speed of 30 mm/s, a hatching distance of 0.2 µm, and a slicing distance of 0.25 µm. The nanopillars were printed with the same laser power and writing speed but the hatching distance was 0.1 µm and the slicing distance was 0.2 µm. This resulted in an array width of 544 ± 0.52 µm, a cage width of 46.1 ± 0.33 µm, a beam diameter of 4.89 ± 0.03 µm, a height of 46.0 ± 0.34 µm, a pillar diameter of 0.24 ± 0.02 nm, a pillar height of 1.86 ± 0.02 µm, an angular pillar spacing of 31.0 ± 0.88 °, and a lateral pillar spacing of 0.83± 0.02 µm.

3.2. Cell behaviour on micro-engineered structures

In this section, we present the results of the cell experiments obtained on the fused silica substrates with or without a laminin coating and on the different IP-Dip structures (2.5D and 3D) with both THP-1 and primary microglia cells.

3.2.1. THP-1 cells

The analysis that was performed on THP-1 behaviour on the fused silica substrates and the different IP-Dip structures is only qualitative. This cell line was used to determine whether the used IP-Dip structures have a cytotoxic effect on macrophages and microglia cells.

THP-1 cells on laminin-coated and uncoated fused silica substrate

By visual inspection of the fluorescent photos in fig. 3.6, one can state that both the uncoated and the laminin-coated fused silica substrate are not cytotoxic for the THP-1 cells. This can be reasoned as few cells are present that show destroyed cell membranes (in fig. 3.6, red colour, nuclei shown in blue) which is an indicator of dead cells. Also, the live/dead assay (using Trypan blue) showed a >95% survival rate for the cells. Using the live/dead assay we could detect dead cells as these were highlighted in a darker colour under a brightfield microscope. Unfortunately, the highlighted cells were almost not visible on the images so these cells were encircled in blue in fig. 3.7. However, The THP-1 cells seem to proliferate less homogeneously on the laminin-coated fused silica substrate as compared to the uncoated counterpart. This is based on the cell clumping that can be seen in fig. 3.6a, which may be caused by cell overgrowth or simply because the cells attach better to different areas on the substrate. Due to cell clumping on the laminin-coated substrate and to limit the number of viability experiments, the choice was made to culture THP-1 cells on uncoated IP-Dip samples only.

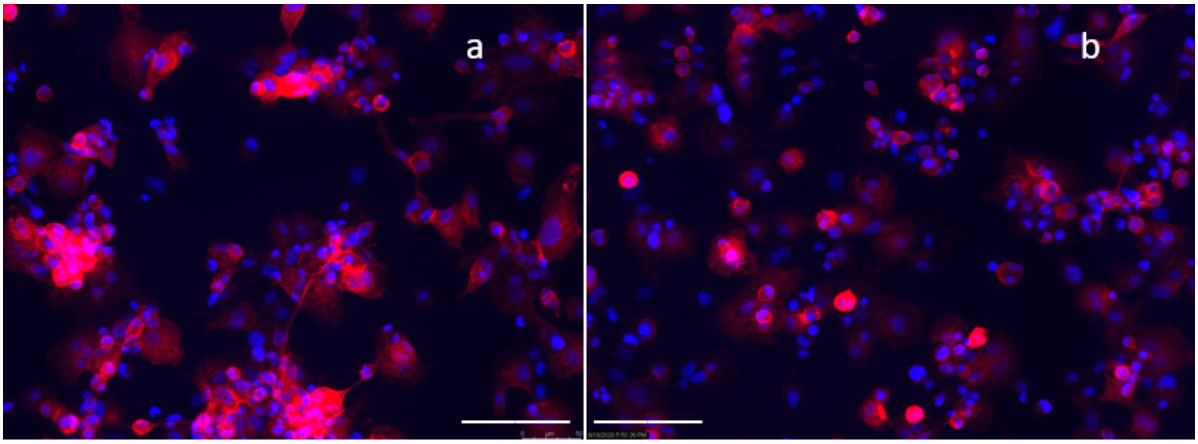

Figure 3.6: Fluorescent image of **(a)** THP-1 cells clustering on laminin coated fused silica substrate, **(b)** THP-1 cells homogeneously distributed on uncoated fused silica substrate. red= macrophage marker CD11b, blue= DAPI staining of cell nuclei. Scale bars 100 μm.

THP-1 cells on 2D and 2.5D structures

As a verification of the survivability of the cells on 2D and 2.5D structures, the same live/dead assay (using Trypan blue) was performed on the IP-Dip pedestal and micro-/ nanopillar structures. The results of the viability test, a >95% survival rate for the cells show that both the pedestal (see fig. 3.8) and the micro-/ nanopillar structures (no image taken) are deemed safe for microglia cultures. A visual representation of the THP-1 cells on the different 2D and 2.5D structures can be seen in fig. 3.10a, fig. 3.10b and fig. 3.10c. The morphology of the THP-1 cells on the uncoated pedestal (Ped 1) is similar to that of the roundly shaped cells cultured on the uncoated fused silica substrate. However, the THP-1 cells cultured on the micro-/nanopillar (MP1 and NP2) arrays show a slightly different morphology, as the cells exhibit multiple branches (highlighted by the red arrows in fig. 3.10b and fig. 3.10c) extending from the cell membrane, this is not commonly seen in literature.

THP-1 cells on 3D structures

As the material and the pillar structure both prove not to show any adverse/negative effects on the cell proliferation, it can be predicted that the 3D cage structure with/without nanopillar decoration will also not

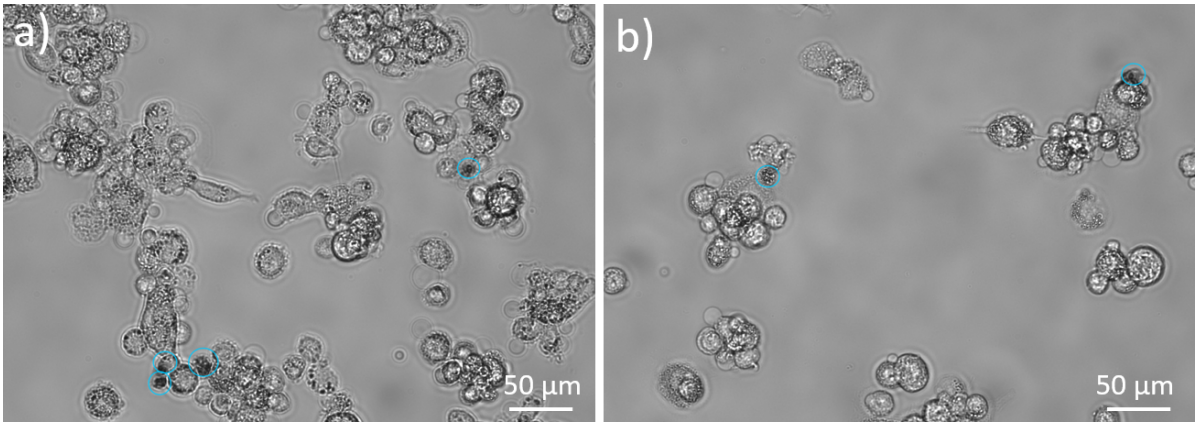

Figure 3.7: Brightfield image of THP-1 cells with Trypan blue staining (encircled in blue) on: **(a)** Laminin coated fused silica substrate. **(b)** Uncoated fused silica substrate.

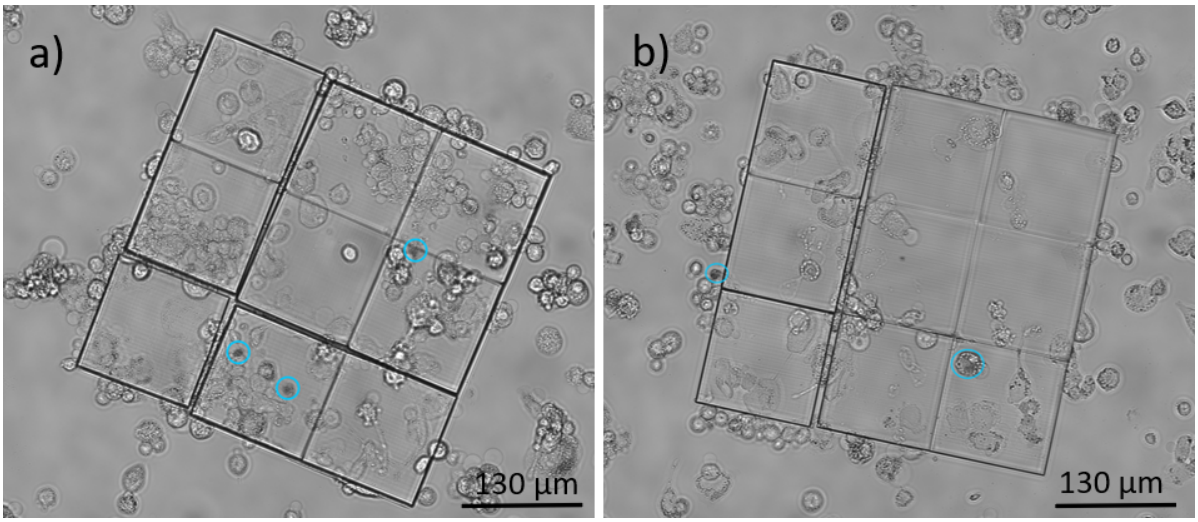

Figure 3.8: Brightfield image of THP-1 cells with Trypan blue staining (encircled in blue) on: **(a)** Laminin coated IP-Dip pedestal. **(b)** Uncoated IP-Dip pedestal.

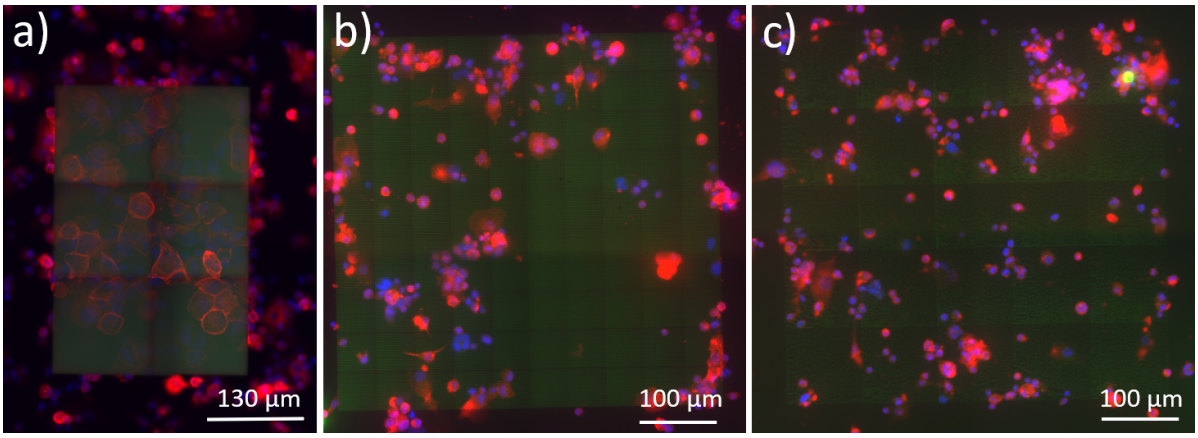

Figure 3.9: Fluorescent image of THP-1 cells on: **(a)** uncoated IP-Dip pedestal. **(b)** Uncoated IP-Dip micropillars. **(c)** Uncoated IP-Dip nanopillars.

pose any cytotoxic effects on the cells. Indeed, THP-1 cells are successfully cultured on the undecorated and micro-/nanopillar decorated cages and show both globular and flat morphologies(fig. 3.10d, e and f). Some

interaction of the cell membrane with the pillar covered cages is present and bending of the nanopillars can be seen. The cells do not seem to have a preference as they are present throughout the cage height.

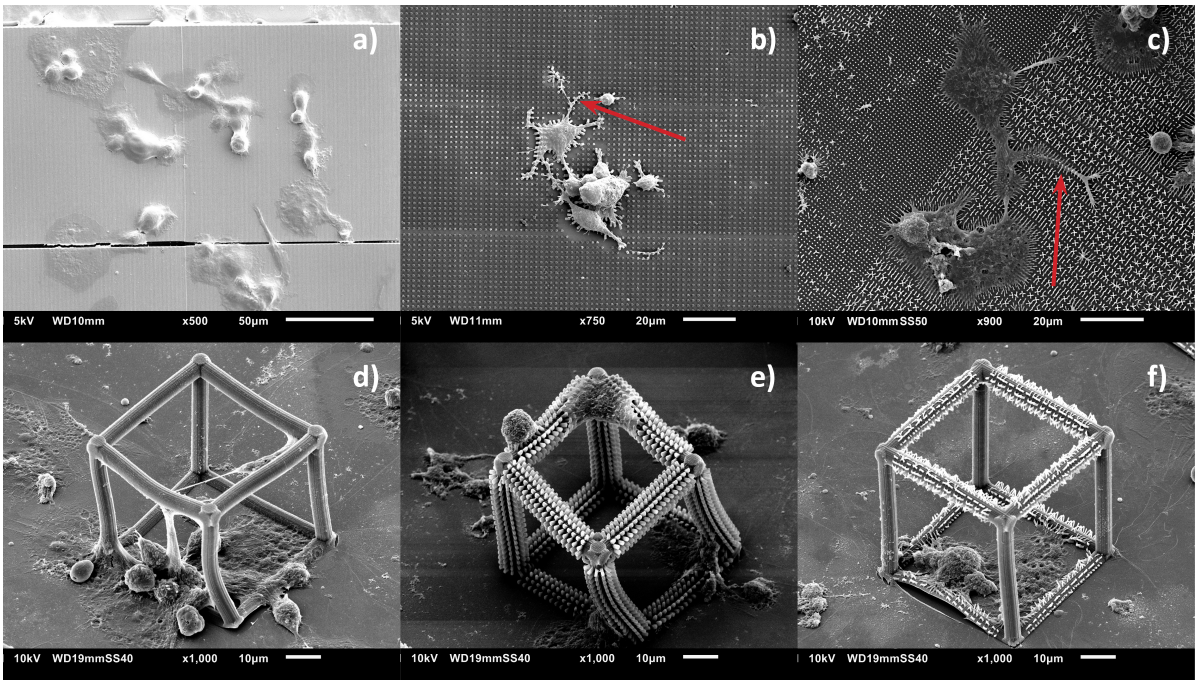

Figure 3.10: THP-1 cells on: **(a)** uncoated pedestal, **(b)** uncoated micropillars (red arrow aims at branch), **(c)** uncoated nanopillars (red arrow aims at branch), **(d)** uncoated 50 µm cage, **(e)** uncoated 50 µm micropillar decorated cage, **(f)** uncoated 50 µm nanopillar decorated cage.

3.2.2. Microglia cell behaviour

In this section, we present the microglia cell experimental results. Firstly, we provide an overview of the donors used for each experiment in table 3.3, showing which structures and conditions were employed. Secondly, we show the distribution of the microglia cell phenotypes present ***in vitro***, for cells on the fused silica substrates, and on the 2D and 2.5D structures. Thirdly, we display graphs that highlight the influence of the surface on cultured ramified microglia cells. Lastly, we talk about the effect of 3D structures on microglia cell morphology.

Laminin coated vs uncoated fused silica substrate

To determine if laminin-coated fused silica substrate (LS) enables a higher percentage of ramified microglia as compared to an uncoated fused silica substrate (US), first the phenotype distribution is determined, followed by the percentage of ramified microglia. A total of 5 donors were employed (R07007, R07110, R17045, R15059, R09153(OC)), and 1-3 samples were used per donor. SEM and fluorescent images were analyzed to extract the average phenotype percentages per donor. Finally, the total average of all the donor's averages was calculated to determine the phenotype percentages. In fig. 3.11a, the phenotype distribution in percentage, present on both LS and US can be seen. On the LS (N_{cells}=1043, 9 samples), the flat amoeboid phenotype amounts to 35.9 ± 22.6%, the bi-polar phenotype represents 30.1 ± 16.6%, the globular phenotype 15.3 ± 12.7% and the non-amoeboid phenotype 18.8 ± 9.57%. Whereas, the phenotype distribution on the US (N_{cells}=1066, 11 samples) was 28.9 ± 21.2% for the flat amoeboid phenotype which is lower than on the LS. The bi-polar phenotype with 30.0 ± 2.74% is almost the same. The globular phenotype covers 19.2 ± 5.04% which is slightly higher. Lastly, the non-amoeboid phenotype is higher showing 22.0 ± 13.4%. The large standard deviation present in most bars is mainly due to the donor-to-donor variance (caused due to differences in age and well-being) and the relatively small data set. Also, it is difficult to determine the general distribution of phenotypes in the brain as microglia cells are plastic cells, which means that the cells are able to change between phenotypes. Additionally, the images used for the cell analysis are only snapshots of the cells at a certain time interval, so dynamic videos of these cells are actually needed to determine anything conclusive. Furthermore, the cell density for the LS was 25.3 x 10^3 ± 20.2 x 10^3 cells/cm^2 versus 25.0 x 10^3 ± 19.8 x 10^3 cells/cm^2 for the US.

Table 3.3: Overview of structures used per donor, both uncoated and laminin-coated. f stands for fluorescent imaging sample, and s stands for SEM imaging samples.

	R07007	R07110	R01068	R17045	R15059	R09153	Total
Substrate	lam: 1x f, 1x s unc: 1x f	lam: 2x f, 1x s unc: 2x f, 1x s	lam: - unc: 1x f, 1x s	lam: 1x f, 1x s unc: 1x f, 1x s	lam: 2x f, 1x s unc: 2x f, 1x s	lam: 1x f, 1x s unc: 1x f, 1x s	**lam: 7x f, 5x s** **unc: 8x f, 5x s**
Ped1	lam: 1x f, 1x s unc: 1x f	lam: 2x f, 1x s unc: 2x f, 1x s	-	-	-	-	**lam: 3x f, 2x s** **unc: 3x f, 1x s**
Ped2	-	-	-	-	-	lam: 1x f unc: -	**lam: 1x f** **unc: -**
MP1	-	-	lam: - unc: 1x f, 1x s	-	-	-	**lam: -** **unc: 1x f**
MP2	-	-		-	lam: 2x f, 1x s unc: 2x f, 1x s	lam: 1x f, 1x s unc: 1x f, 1x s	**lam: 3x f, 2x s** **unc: 3x f, 2x s**
NP1	-	-	lam: - unc: 1x f, 1x s	-	-	-	**lam: -** **unc: 1x f, 1x s**
NP2	-	-	-	-	lam: 1x f unc: -	lam: - unc: 1x s	**lam: 1x f, 0x s** **unc: 0x f, 1x s**
SC	-	-	-	lam: 1x f, 1x s unc: 1x f, 1x s	lam: 1x f, 1x s unc: 2x f, 1x s	-	**lam: 2x f, 2x s** **unc: 3x f, 2x s**
SC-MP	-	-	-	-	lam: 2x f, 1x s unc: 2x f, 1x s	-	**lam: 2x f, 1x s** **unc: 2x f, 1x s**
BC	-	-	-	-	lam: 1x s unc: 1x s	lam: 2x f, 2x s unc: 2x f, 2x s	**lam: 2x f, 3x s** **unc: 2x f, 3x s**
BC-MP	-	-	-	-	lam: 1x f, 1x s unc: 2x f, 1x s	lam: 2x f, 2x s unc: 2x f, 2x s	**lam: 3x f, 3x s** **unc: 4x f, 3x s**
BC-NP	-	-	-	-	-	lam: 2x f, 2x s unc: 2x f, 2x s	**lam: 2x f, 2x s** **unc: 2x f, 2x s**

In fig. 3.11b one can see that using a laminin coating ($N_{RamifiedCells}$=64, 9 samples) results in 7.61 ± 3.29% ramified cells (≈40.5% of the non-amoeboid cells are ramified), which is slightly lower as compared to 9.88 ± 7.68% ramified cells (≈44.9% of non-amoeboid cells are ramified) present on the US ($N_{RamifiedCells}$=83, 11 samples). Although it can be seen that on average the US provides a higher percentage of ramified cells as compared to microglia on LS, a paired t-test showed a two-tailed p-value of 0.58 (significance level 5%), meaning that the difference is not statistically significant. The Sholl plot as seen in fig. 3.11c, indicates that ramified cells grown on an US($N_{RamifiedCells}$=41, 9 samples), have more intersections, and are more complex/ramified than cells grown on LS($N_{RamifiedCells}$=36, 9 samples). However, the range of the branches is shorter. To summarize it can be said that laminin on substrates does not increase cell complexity, but in fact creates cells that are less complex. A representation of the ramified phenotype data employed for the paired t-test is shown in fig. 3.11d. The corresponding area under the curve as given in fig. 3.11e, shows an area of 288 ± 86.1 a.u. for ramified cells on a LS ($N_{RamifiedCells}$=36, 9 samples) and 318 ± 111 a.u. (arbitrary units) for ramified cells on an US ($N_{RamifiedCells}$=41, 9 samples). This confirms that ramified microglia that are cultured on US are more complex than when cultured on LS. Finally, that ramified cells grown on US are more complex is validated when evaluating the number of primary branches per ramified cell in fig. 3.11f. The graph shows an average of 4.45 ± 0.65 branches/cell for cells on LS ($N_{RamifiedCells}$=36, 9 samples) and a higher number of 5.57 ± 2.85 branches/cell, on an US ($N_{RamifiedCells}$=41, 9 samples). The laminin has a negative effect on the percentage of ramified microglia but the difference is not significant.

Laminin coated vs uncoated IP-Dip pedestal

Regarding the experiments of the microglia cells cultured on the IP-Dip pedestals, not enough data was present to perform statistical analysis on the phenotype distribution or any other comparison between the cells cultured on a laminin-coated pedestal versus an uncoated pedestal. This was partially due to the microglia phenotypes in the first two experiments (R07007, R07110) not being able to be distinguished due to the unclear fluorescent images taken by the inverted fluorescent microscope. The other unfortunate reason is that throughout the other experiments (R01068, R17045, R15059 and R09153) only one pedestal remained attached to the substrate (fig. 3.1f).

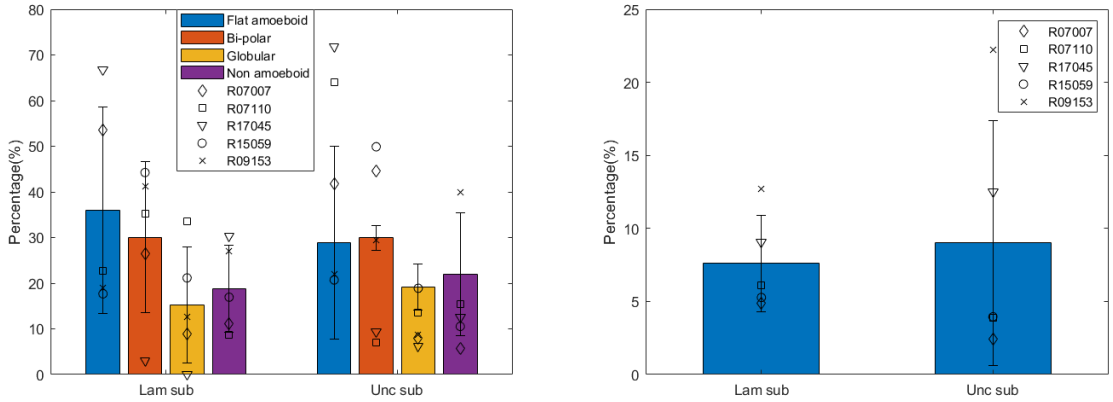

(a)

(b)

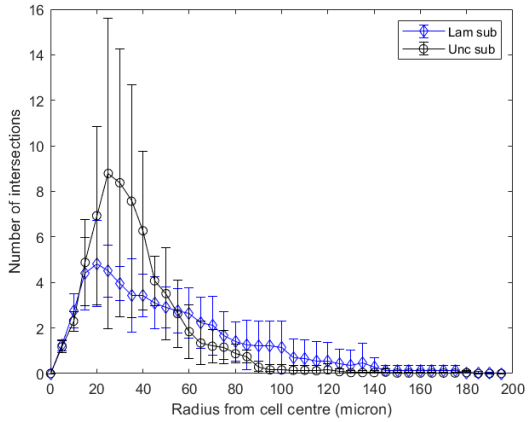

(c)

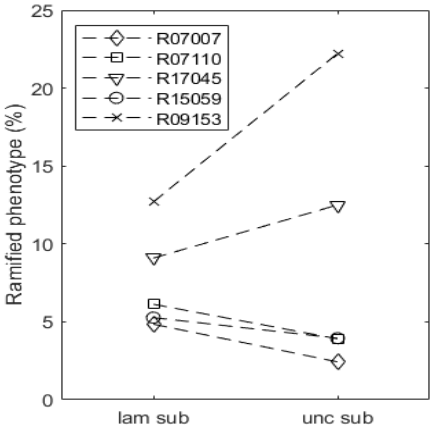

(d)

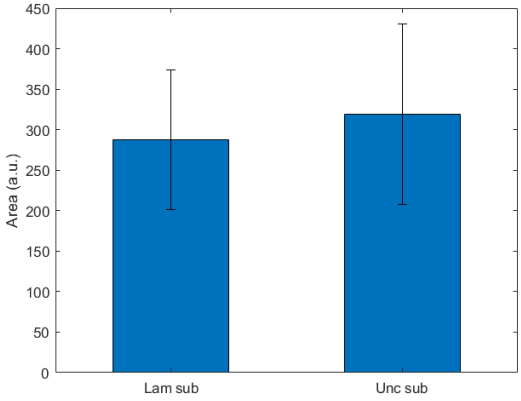

(e)

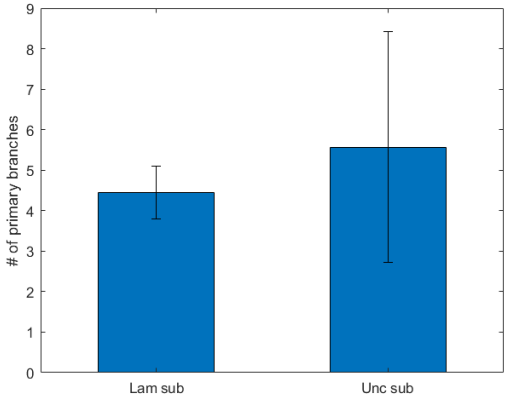

(f)

Figure 3.11: Comparison between LS and US. Bars represent the mean, and error bars the SD. **(a)** Phenotype distribution of the LS(N=1043, 9 samples) and the US(N=1066, 11 samples). **(b)** Ramified phenotype percentage, LS(N=64, 9 samples) vs. US(N=83, 11 samples). **(c)** Sholl plot of the ramified microglia cultured on a LS(N=36, 9 samples) and US(N=41, 9 samples). **(d)** Ramified percentages per donor LS(N=64, 9 samples) and US(N=83, 11 samples). **(e)** Area under the curve for LS(N=36, 9 samples) and US(N=41, 9 samples). **(f)** Primary branches per cell for LS(N=36, 9 samples) and US(N=41, 9 samples).

Laminin coated vs uncoated IP-Dip micropillars

Microglia on laminin-coated micropillars (LMP) are compared with microglia on uncoated micropillars (UMP) to determine which configuration results in a higher percentage of the desired ramified phenotype. Cells of two donors (R15059, R09153 (OC)) were cultured on MP2, with again 1-3 samples per donor consisting of both SEM and fluorescent images. In fig. 3.12a, it can be seen that on the LMP (N_{cells}=525, 5 samples), the flat amoeboid phenotype amounts to 44.1 ± 23.5%, the bi-polar phenotype represents 28.1 ± 19.7%, the globular phenotype 11.1± 5.16% and the non-amoeboid phenotype 16.8 ± 13.4%. Whereas, the phenotype distribution on the UMP (N_{cells}=441, 5 samples) was 36.9 ± 0.89% for the flat amoeboid phenotype which is lower than on the LMP. The bi-polar phenotype with 26.4 ± 0.91% is slightly lower. The globular phenotype covers 12.7 ± 9.72% which is slightly higher. Lastly, the non-amoeboid phenotype is higher showing 24.1 ± 7.99%. When comparing the two groups of bar plots, excluding the standard deviation and the percentages not being the same between LMP and UMP, they seem to be similar in shape. Again, the large standard deviation (SD) for LMP is caused by the donor-to-donor variance and small data set of only 2 donors. This, however, does not explain the small SD for both the flat amoeboid and bi-polar phenotype for the UMP, our best-educated guess is that this is merely a stroke of luck. Furthermore, the cell density for the LMP was 48.9 x 10^3 ± 10.9 x 10^3 cells/cm^2 versus 40.7 x 10^3 ± 24.5 x 10^3 cells/cm^2 for the UMP.

We further show that in fig. 3.12b one can see how using LMP ($N_{RamifiedCells}$=53, 5 samples) results in 12.4 ± 8.75% ramified cells (≈73.8% of the non-amoeboid cells consist of ramified cells), which is on average slightly lower as compared to 15.2 ± 3.55% ramified cells (≈63.1% of the non-amoeboid cells consist or ramified cells) present on the UMP ($N_{RamifiedCells}$=59, 5 samples). A paired t-test gives a two-tailed p-value of 0.60 (significance level 5%), confirming that no statistically significant difference is present. The Sholl plot as seen in fig. 3.12c, shows that ramified cells grown on either LMP ($N_{RamifiedCells}$=19, 4 samples) or UMP ($N_{RamifiedCells}$=20, 4 samples) do not make a difference in terms of cell complexity as both plots are similar, meaning that the cells are similar in complexity. The ramified data used for the paired t-test is shown in fig. 3.12d. The area under the curve as given in fig. 3.12e, shows an area of 287 ± 109 a.u. for ramified cells on LMP($N_{RamifiedCells}$=19, 4 samples) and 295 ± 63.6 a.u. for ramified cells on UMP ($N_{RamifiedCells}$=20, 4 samples). This re-states that the difference in values and thus cell complexity is negligible. Finally, the negligible difference in cell complexity is confirmed when looking at the number of primary branches per ramified cell in fig. 3.12f. The graph shows an average of 5.78 ± 1.03 branches/cell for cells on LMP ($N_{RamifiedCells}$=19, 4 samples) and 5.90 ± 1.13 branches/cell on UMP ($N_{RamifiedCells}$=20, 4 samples).

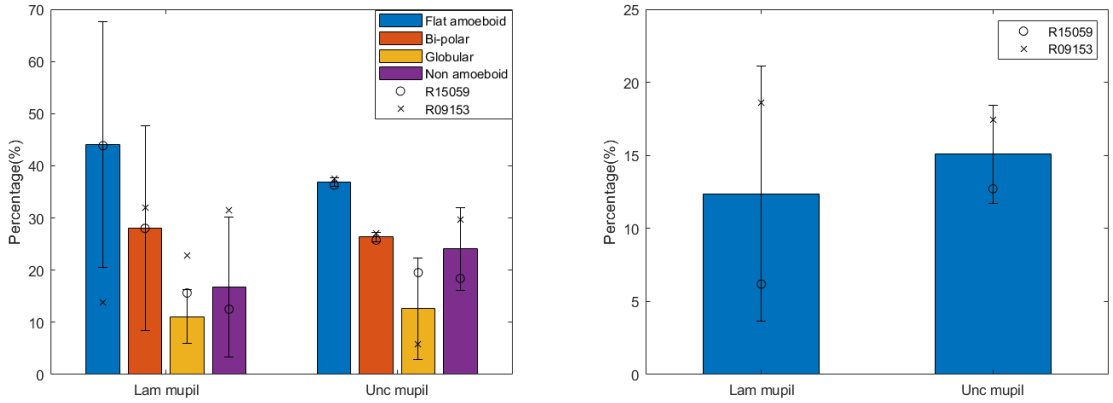

(a)

(b)

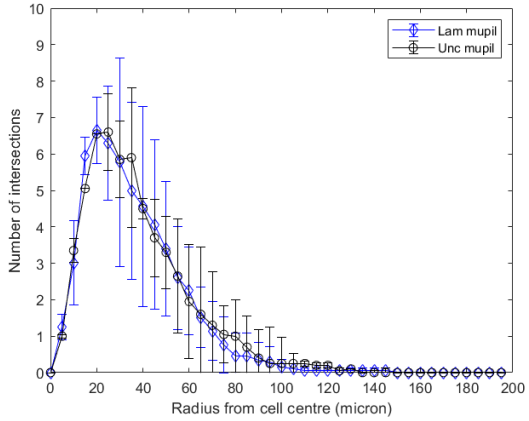

(c)

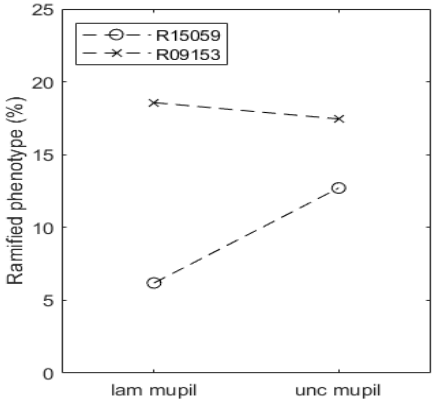

(d)

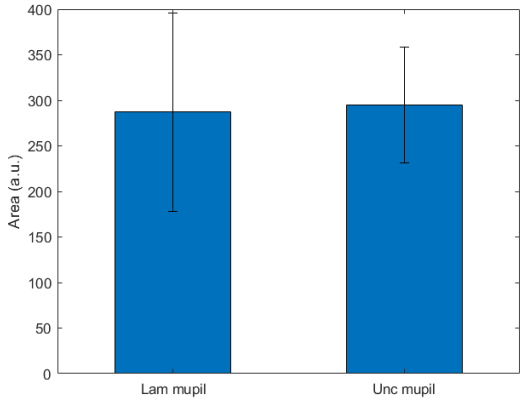

(e)

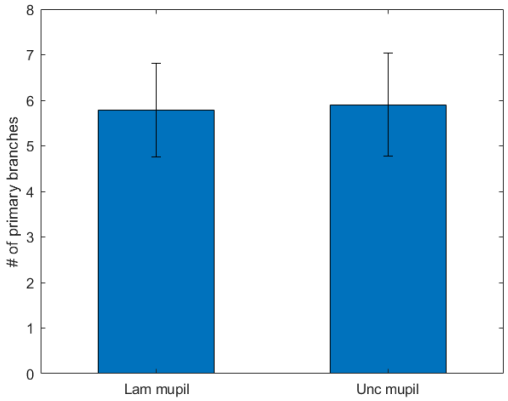

(f)

Figure 3.12: Comparison between LMP and UMP. Bars represent the mean, and error bars the SD. **(a)** Phenotype distribution of the LMP(N=525, 5 samples) and the UMP(N=441, 5 samples). **(b)** Ramified phenotype percentage, LMP(N=53, 5 samples) and UMP(N=59, 5 samples). **(c)** Sholl plot of the ramified microglia cultured on LMP(N=19, 4 samples) and UMP(N=20, 4 samples). **(d)** Ramified cells percentage per donor LMP(N=53, 5 samples) and the UMP(N=59, 5 samples). **(e)** Area under the curve for LMP(N=19, 4 samples) and UMP(N=20, 4 samples). **(f)** Primary branches per cell for LMP(N=19, 4 samples) and UMP(N=20, 4 samples).

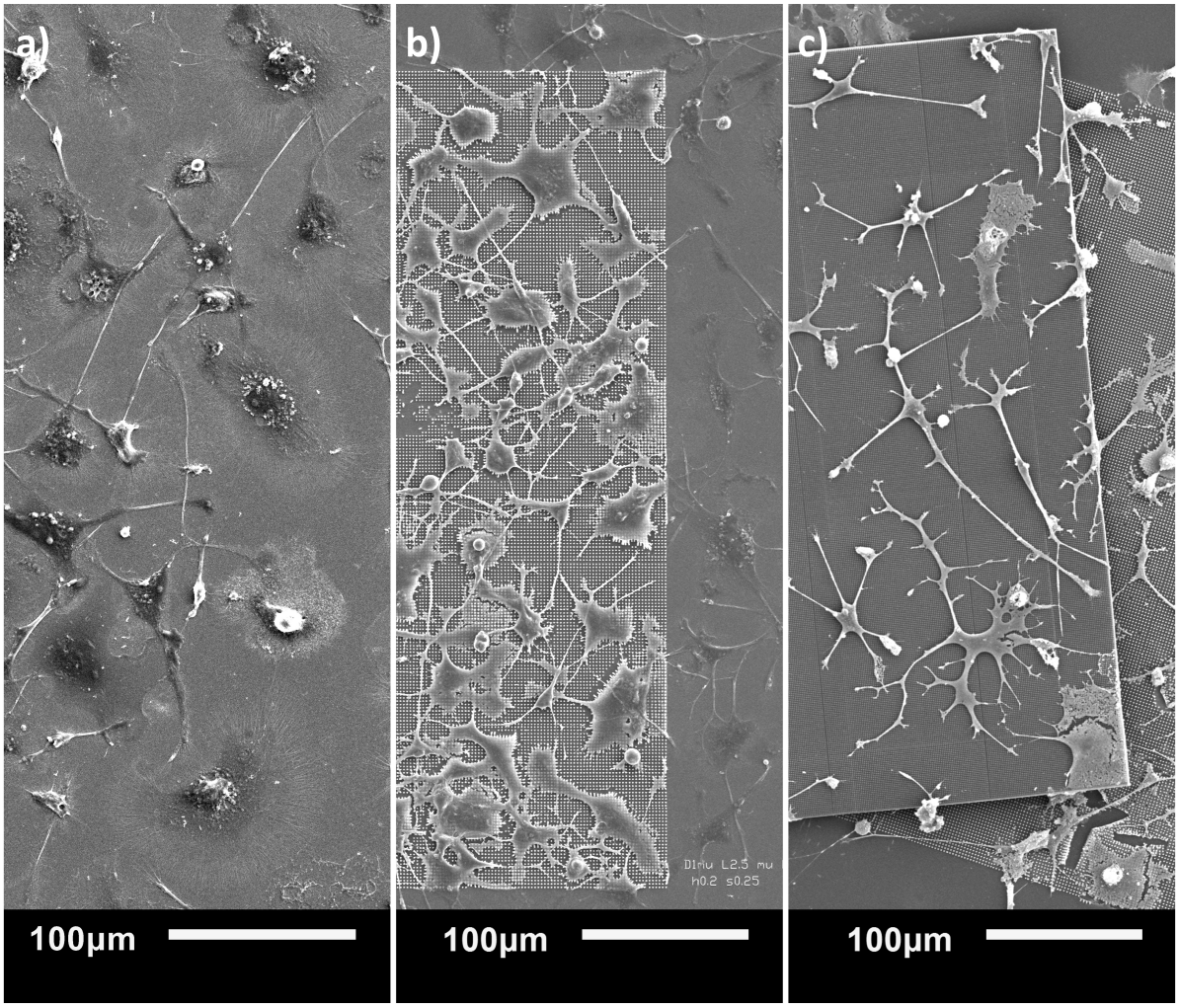

Figure 3.13: SEM photo of the effect of 2.5D structures on microglia morphology with respect to a flat fused silica substrate. **(a)** US with the majority of cells being flat amoeboid cells. **(b)** UMP(MP1) showing branched cells. **(c)** UNP(NP2) showing highly ramified cells.

2Dimensional vs 2.5Dimensional growth environments

Culturing microglia cells on 2.5D structures has an effect on cell morphology. In fig. 3.13a we show that on the flat US, the majority of microglia consist of flat amoeboid cells. Whereas, the microglia on the micropillars show morphologies that are more branched (fig. 3.13b). And lastly, the microglia on the nanopillars (fig. 3.13c) show highly ramified morphology. We also provide SEM images of a 45° tilted view (fig. 3.14 of the microglia that are cultured on the micro-and nanopillars in which it is confirmed that the cells are definitely on top of the pillars. The US, UMP and uncoated nanopillars(UNP) are compared to determine if the structure configuration results in a higher percentage of the desired ramified phenotype. A total of 2 donors were used (R01068(OC, MP1, NP1), R09153(OC, MP2, NP2)), using 1-3 samples per donor, consisting of both SEM and fluorescent images. In fig. 3.15a, it can be seen that on the US (N_{cells}=315, 4 samples), the flat amoeboid phenotype amounts to 26.1 ± 5.9%, the bi-polar phenotype represents 30.5 ± 1.34%, the globular phenotype 12.3± 5.03% and the non-amoeboid phenotype 31.3 ± 12.3%. The phenotype distribution on the UMP (N_{cells}=392, 4 samples) was 32.7 ± 6.70% for the flat amoeboid phenotype which is higher. The bi-polar phenotype with 23.4 ± 5.10% is lower. The globular phenotype covers 17.1 ± 15.9% which is higher. Lastly, the non-amoeboid phenotype is lower showing 26.8 ± 4.14%. Whereas, the phenotype distribution on the UNP (N_{cells}=316, 3 samples) was 16.8 ± 9.56% for the flat amoeboid phenotype which is lower than both the US and the UMP. The bi-polar phenotype with 15.5 ± 7.76% is also lower than both the US and the UMP. The globular phenotype covers 12.3 ± 17.4% which is the same as the US but lower than the UMP. Finally, the non-amoeboid phenotype is higher than both US and the UMP showing 58.4 ± 34.7%. Furthermore, the cell density for the US was 21.3 x 10^3 ± 4.88 x 10^3 cells/cm^2, 43.4 x 10^3 ± 28.3 x 10^3 cells/cm^2 for the UMP, and

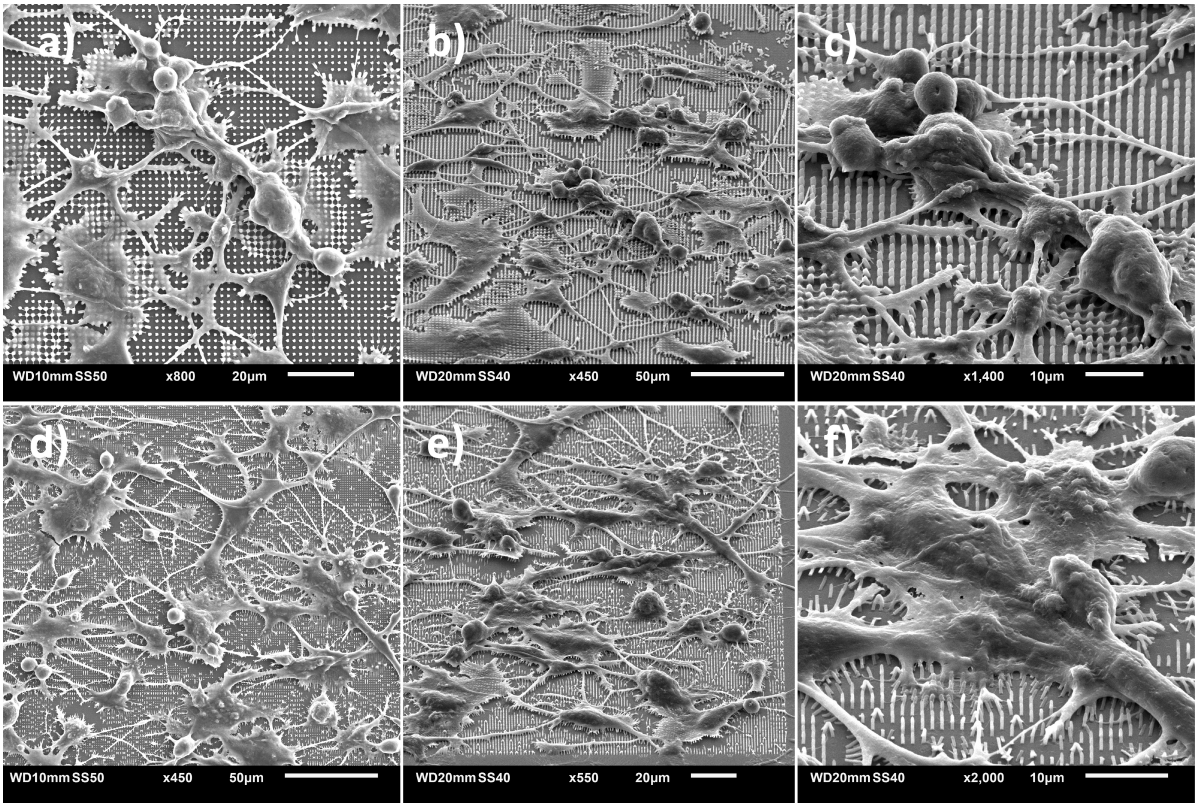

Figure 3.14: SEM images showing: Top view of microglia on MP1 **(a)** and NP1 **(d)**, and a 45° tilted view of: **(b and c)** microglia on MP1, **(e and f)** microglia on NP1 (donor R01068).

$39.8 \times 10^3 \pm 45.0 \times 10^3$ cells/cm^2 for the UNP.

In fig. 3.15b, one can see that cells cultured on the US ($N_{RamifiedCells}$=41, 4 samples) result in 15.6 ± 9.31% ramified cells (≈49.8% of non-amoeboid cells consist of ramified cells), which is negligible when compared to 15.2 ± 3.2% ramified cells (≈56.7% of non-amoeboid cells consist of ramified cells) present on the UMP ($N_{RamifiedCells}$=53, 4 samples). This is significantly less when compared to 42.8 ± 38.4% ramified cells (≈73.3% of non-amoeboid cells consist of ramified cells) present on the UNP ($N_{RamifiedCells}$=62, 3 samples). A paired t-test provided a two-tailed p-value of 0.41 (significance level 5%), confirming that no statistically significant difference is present between cells cultured on the US or cells cultured on the UNP.

Although no comparative ***in vivo*** data exist for the white matter phenotype distribution of the rhesus macaque, human ***in vivo*** white matter data is compared as the resemblance is high. On that account, the flat amoeboid percentage (26.1%) is higher for cells on the US, but the ramified percentage (15.6%) is significantly less than that of human ***in vivo*** white matter phenotypes (18% amoeboid and 43% ramified cells [19]). However, the nanopillar arrays provide on average 16.8% flat amoeboid and 42.8% ramified cells. Although not statistically significant (due to the usage of 2 donors), we can say that the decreased effective shear modulus, due to the NP configuration, affects the microglia cells in a positive way causing them to resemble the phenotype distribution of ***in vivo*** microglia. Additionally, we can see that employing NPs causes the percentage of ramified cells (≈73.3%) within the non-amoeboid group to increase with respect to cells cultured on US (≈49.8%). For these reasons, this structure type is very promising in the quest to culture more ***in vivo*** like homeostatic ramified microglia cells. The data used for the paired t-test is presented in fig. 3.15d, in which the high percentage of ≈70% ramified cells was from donor R09153 and cultured on NP2 (see fig. 3.16 for representation of the cell morphology). The difference in ramified phenotype percentages between cells cultured on the US and the UMP, and between cells cultured on the UMP and the UNP is also not statistically significant. We show in the Sholl plot as seen in fig. 3.15c, that ramified cells grown on the US ($N_{RamifiedCells}$=15, 3 samples) are the least complex cells, followed by ramified cells cultured on the UMP ($N_{RamifiedCells}$=15, 3 samples). The cells cultured on the UNP ($N_{RamifiedCells}$=13, 3 samples) are the most complex, indicated by the highest amount of

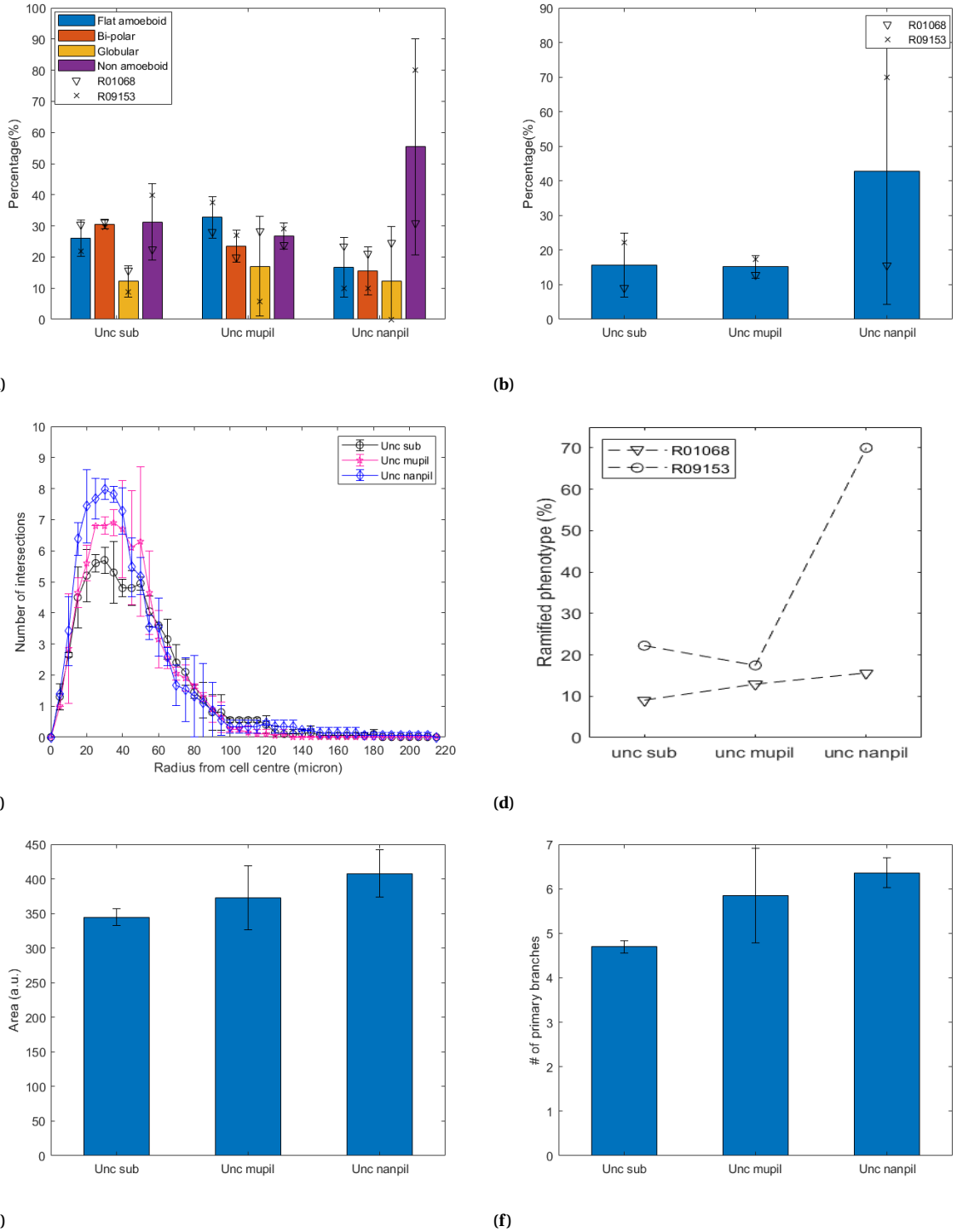

Figure 3.15: Comparison between US, UMP and UNP. Bars represent the mean, and error bars the SD. **(a)** Phenotype distribution of cells on the US (N=315, 4 samples), the UMP (N=392, 4 samples), and the UNP(N=316, 3 samples). **(b)** Ramified phenotype percentage, US (N=41, 4 samples), UMP (N=53, 4 samples), and UNP(N=62, 3 samples). **(c)** Sholl plot of the ramified microglia cultured on US (N=15, 3 samples), the UMP (N=15, 3 samples), and the UNP(N=3, 3 samples). **(d)** Ramified cell percentages per donor for US (N=41, 4 samples), UMP (N=53, 4 samples), and UNP(N=62, 3 samples). **(e)** Area under the curve for US (N=15, 3 samples), the UMP (N=15, 3 samples), and the UNP(N=3, 3 samples). **(f)** Primary branches per cell for US (N=15, 3 samples), the UMP (N=15, 3 samples), and the UNP(N=3, 3 samples).

intersections. The AUC, as given in fig. 3.15e, shows an upward trend, which confirms that the cells cultured

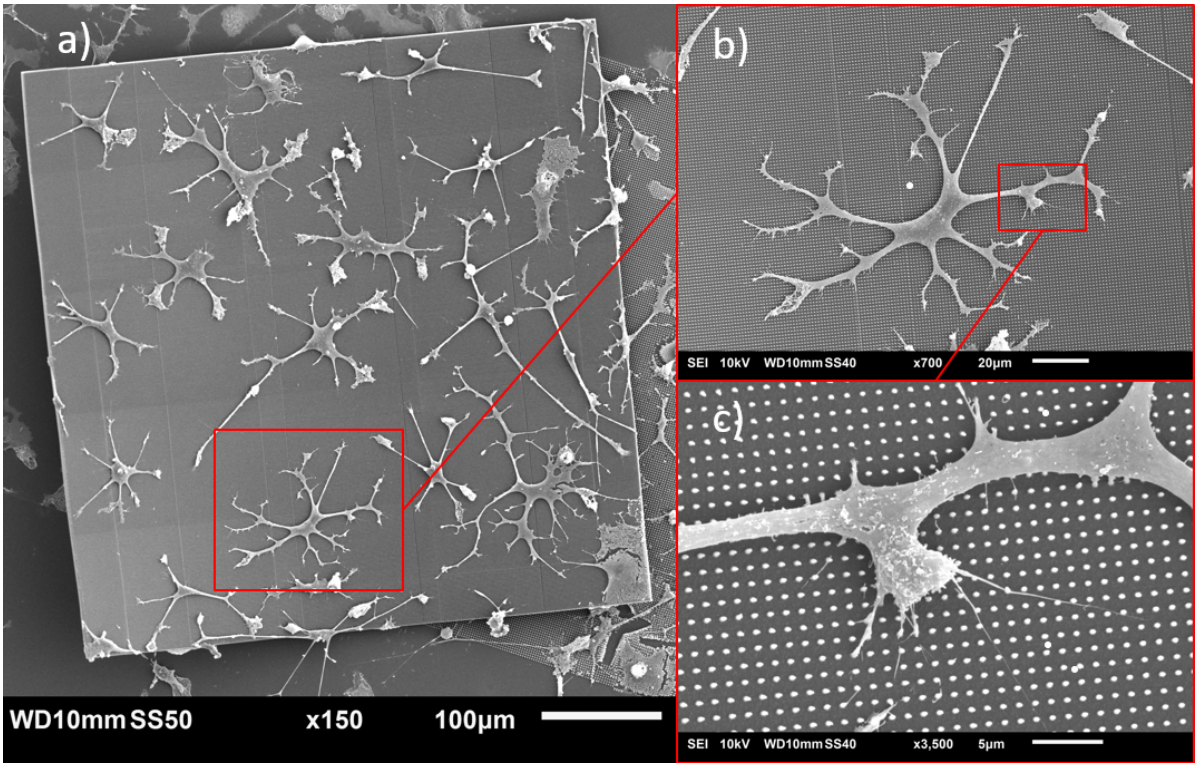

Figure 3.16: SEM photo of: **(a)** Ramified microglia on UNP (NP2, donor R09153). **(b)** Zoomed-in picture of a ramified cell, showing the ramified branches. **(c)** Zoomed-in picture of a primary branch with filopodia extending from the cell membrane and interacting with the NP.

on the UNP are the most complex. The AUC graph in fig. 3.15e shows an area of 345 ± 12.4 a.u. for ramified cells cultured on the US ($N_{RamifiedCells}$=15, 3 samples), 373 ± 46.0 a.u. for ramified cells cultured on the UMP ($N_{RamifiedCells}$=15, 3 samples), and 408 ± 33.9 a.u. for ramified cells cultured on the UNP ($N_{RamifiedCells}$=13, 3 samples). Finally, in terms of primary branches per ramified cell, a similar upward trend is seen in fig. 3.15f. The graph shows an average of 4.70 ± 0.14 branches/cell for cells cultured on an US ($N_{RamifiedCells}$=15, 3 samples), which is resembling that of ***in vivo*** data (4.9 ± 0.6 per cell with a range between 2 and 9 [19]). The number of branches is higher for ramified cells cultured on UMP ($N_{RamifiedCells}$=15, 3 samples) showing 5.85 ± 1.06 branches/cell. Lastly, 6.36 ± 0.34 branches/cell for ramified cells cultured on UNP ($N_{RamifiedCells}$=13, 3 samples), also shows more primary branches as compared ***in vivo*** microglia. A paired t-test was performed, comparing the number of primary branches of cells cultured on the US to cells cultured on the UNP, giving a p-value of 0.053 (significance level 5%) deeming the difference almost statistically significant. The higher number of primary processes for the cells cultured on micro-/nanopillars is most probably because of the high number of anchoring points in multiple directions, providing better support for the cells to exert forces on. The effective shear modulus (11 MPa -200 kPa) of the pillars which is more resembling that of the brain (≈ 1kPa) than the modulus of the fused silica substrate (≈ 70 GPa), also plays a positive role in culturing a homeostatic ramified microglia cell.

Filopodia adhesion

From the SEM images in fig. 3.17, of the ramified microglia on an uncoated fused silica substrate and on the uncoated micro-/nanopillar array it can be seen that the interaction of the filopodia with the different morphologies acts differently. It is observed that the membrane at the end of the primary branch of the ramified microglia on the uncoated fused silica substrate (fig. 3.17a) is flatter and more spread out as compared to the membrane on the less wide branches of the ramified microglia cultured on the micro-and nanopillar array. Because the forces exerted by the filopodia on the substrate surface are not aligned with the stress fibres within the cell membrane, the cell membrane has to distribute the forces in multiple directions in order to

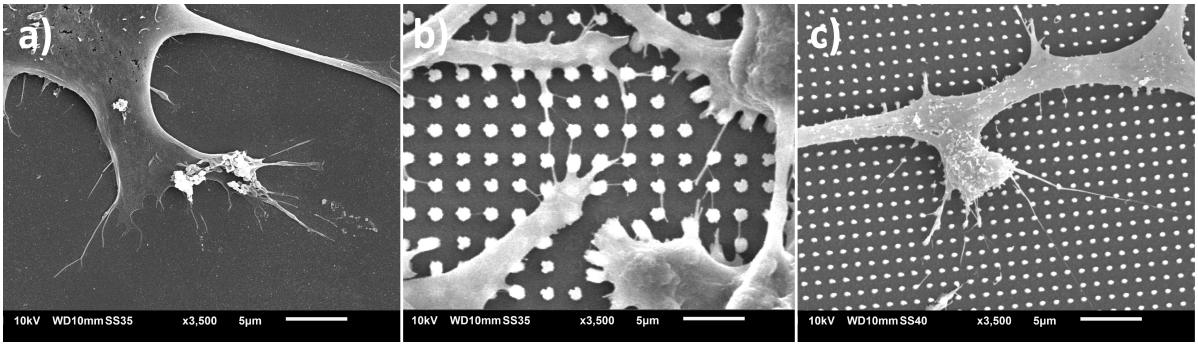

Figure 3.17: SEM pictures of ramified microglia filopodia interacting with: **(a)** uncoated fused silica substrate, **(b)** micropillar array (height 1.97 µm, diameter 0.97 µm), **(c)** nanopillar array (height 1.82 µm, diameter 0.29 µm).

migrate. The stresses on the membrane in multiple directions are what causes the cell membrane to be flat. Furthermore, the filopodia on the micro-and nanopillar (fig. 3.17b and c) array seem to only extend from pillar to pillar and avoid attaching to the fused silica substrate that lies underneath. It seems like the cells deliberately choose to avoid the fused silica substrate, and prefer displacement through using the pillars. Additionally, the pillar structures seem to bend in direction of the forces exerted by the stress fibres in the cell membrane, and therefore the filopodia need fewer anchoring points to distribute the force to migrate, this is also the reason for the cell membrane to be less flat than the cells cultured on a flat surface. We believe that integrating material with a decreased effective shear modulus (low stiffness material), caused by the bending pillars, can trigger an increase in the ramified phenotype by stimulating the filopodia which is the sensing organ of the microglia cell.

3Dimensional vs decorated 3Dimensional IP-Dip micro-environments

The experiments performed with the cells from donors R17045, R15059 and R09153(OC) were used for the qualitative analysis. However, only the cells from donor R09153 were quantitatively analyzed. This is due to the cages on the substrates of the other two donors being largely washed away, piled on top of each other or rotated in an unusable way for analysis.

Qualitative analysis

When we observe the microglia cell covering the 25 µm wide SC in fig. 3.18a, it appears that the cell is attempting to cover/enwrap and phagocytize the entire cage. This is possibly due to the high stiffness of the material and due to small size of the structure, making it possible for the cell to phagocytize the structure in its entirety. In fig. 3.18b some branches can be seen on the 25 µm wide SC-MP, but the cells are still trying to phagocytize the cage, regardless of the added MPs. A reason for this could be that the size of the cage has not increased by much as compared to SC. However, when we evaluate the 50 µm wide BC, both decorated and undecorated, we see that the cells also take on morphologies that do not necessarily try to phagocytize the cage, but that extend primary branches in multiple directions. The reasoning behind this could be that the size difference causes the cells to react differently. In fig. 3.18c, an enwrapping cell can be seen on top of the BC, and on the bottom a ramified cell is seen, extending a primary branch upwards in the third dimension. Looking at fig. 3.18d, next to the enwrapping cell and the ramified cell, also the globular and bi-polar phenotype can be seen on the BC-MP. Lastly, in fig. 3.18e all phenotypes can be seen on the BC-NP, and the ramified cell on top of the cage is also seen extending its branches in three dimensions within the cage. In general in figs. 3.18c to 3.18e, a higher variability of phenotypes can be seen on the 50 µm cages with respect to the 25 µm cages. Also, the decoration increases the phenotype variability even more. Additionally, the cells cultured on these 3D structures exhibit a more three-dimensional morphology as compared to the cells cultured on the flat substrate and 2.5D structures, which is more resembling the 3D morphology of ***in vivo*** cells.

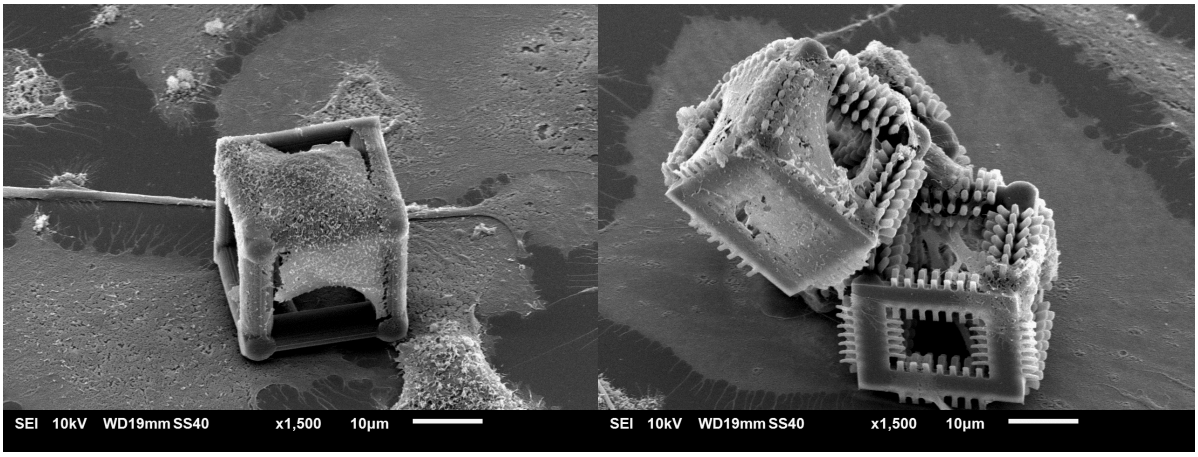

(a) (b)

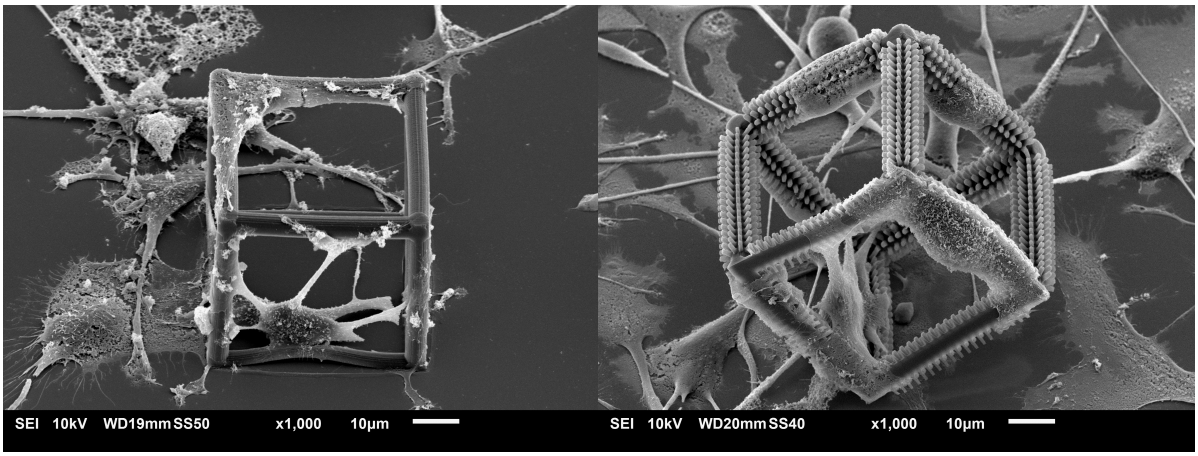

(c) (d)

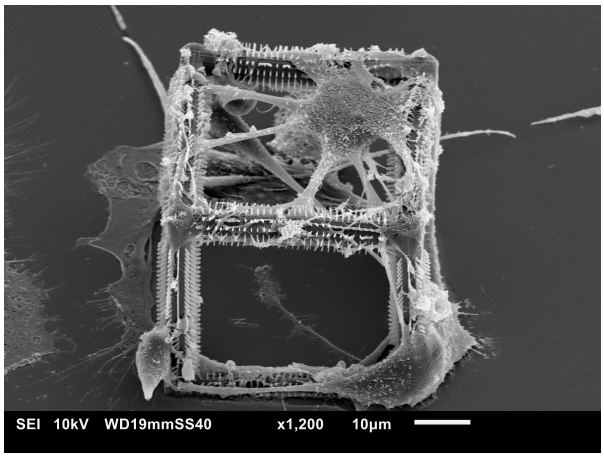

(e)

Figure 3.18: SEM photos of microglia covering different cages. **(a)** Cell wrapping around SM. **(b)** Cell wrapping around SM-MP. **(c)** Enwrapping cell and ramified cell on BC. Ramified cell extending process in the z-direction. **(d)** Globular, bi-polar, enwrapping and ramified cell on BC-MP. **(e)** Globular, bi-polar, enwrapping and ramified cell on BC-NP. Ramified cell extending processes in all directions.

In fig. 3.19a to c, the interaction of filopodia with the surface of an undecorated cage can be seen. It is apparent that the filopodia mostly extend in directions parallel or perpendicular to the hatching lines of the cage. The filopodia on the BC-MP in fig. 3.19d to f, can be seen to extend in multiple directions bridging distances between pillars and are not forced to follow the hatching lines on the cage. The BC-NP in fig. 3.19g to i shows

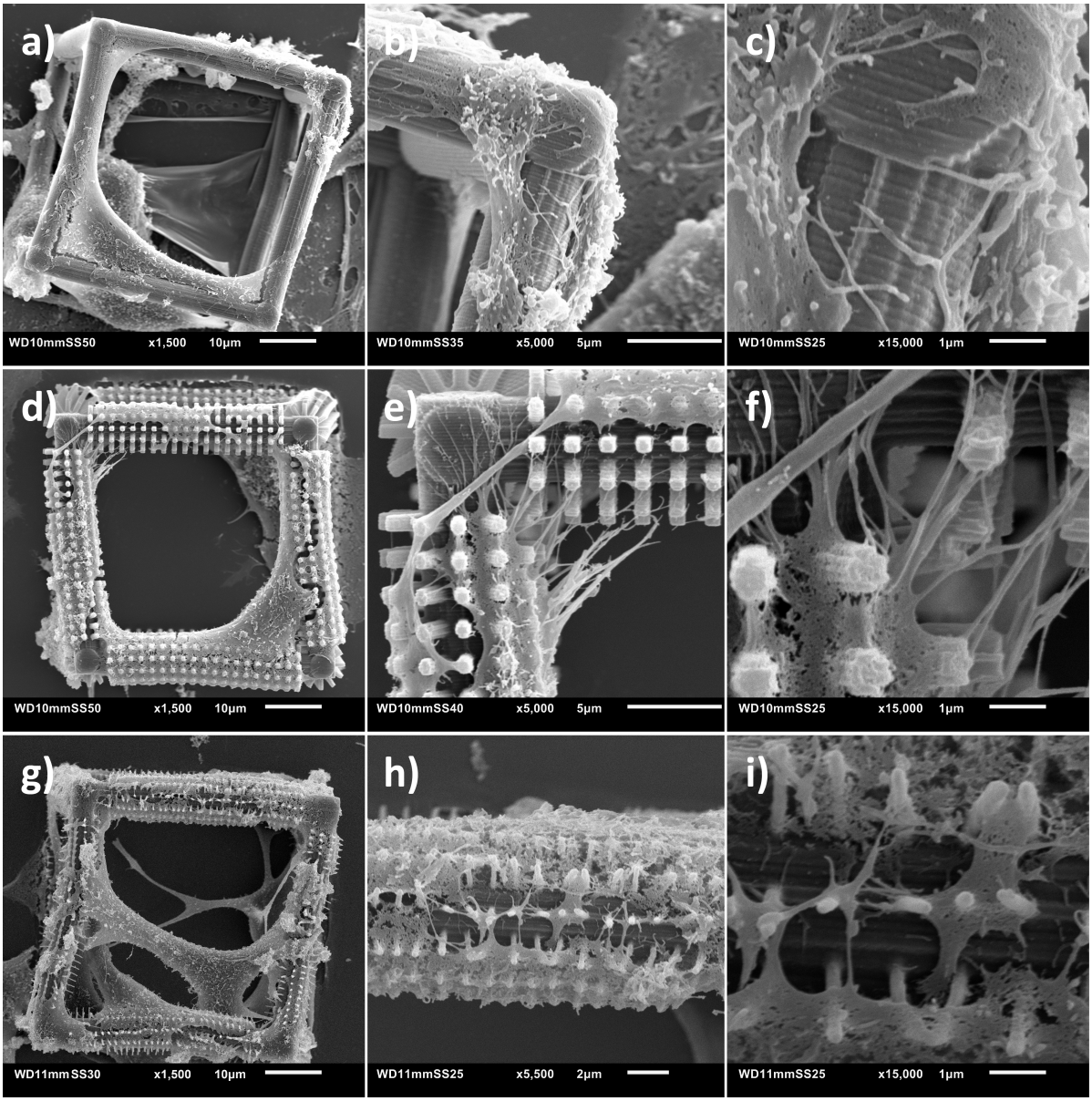

Figure 3.19: SEM photo of microglia filopodia interaction with cages. **(a), (b) and (c)** Filopodia align parallel and perpendicular to the hatching lines on the BC. **(d), (e) and (f)** The filopodia are not constrained by the hatching lines but extend in multiple directions between micropillars on the BC-MP. **(g), (h) and (i)** The filopodia similarly extend between nanopillars on the BC-NP and are not forced to follow the hatching lines of the cage.

the behaviour of filopodia similar to that of the BC-MP, in that the filopodia extend in multiple directions, from pillar to pillar. Another phenomenon that can be seen here, is that the nanopillars also bend in direction of the exerted forces induced by the filopodia and the cell membrane. The filopodia, when introduced to micro and nanopillars, specifically choose to refrain from interacting with the undecorated surface. The reason behind this is that the reduced effective shear modulus of the pillars, probably induce less energy to be consumed when contracting the stress fibres within the cell membrane to transport via the pillars.

Quantitative analysis of the cell occupancy w.r.t. the cage height

This analysis is performed to see if the added micro-/nanopillar decoration has an effect on the cell occupancy throughout the height of the 3D structures.

When observing fig. 3.20a and fig. 3.20b. We notice that the cells cultured on the undecorated cages are mostly located at the bottom of the cage. However, we discover in fig. 3.20c to fig. 3.20f, is that on average for the BC-MP, a displacement of cells takes place from the bottom and are more distributed upwards. The same goes for cells on BC-NP, although less apparent than for the BC-MP, but more than for cells on BC. Although we believe that this effect is caused by the additional anchoring points that are provided by the nanopillars, it can not be concluded as the number of samples is not sufficient. Also, the negative standard deviation in some bars is because of the contribution of cages with zero cells at certain z-ranges. This in combination with a low cell count results in a cell count for a z-range lower than zero.

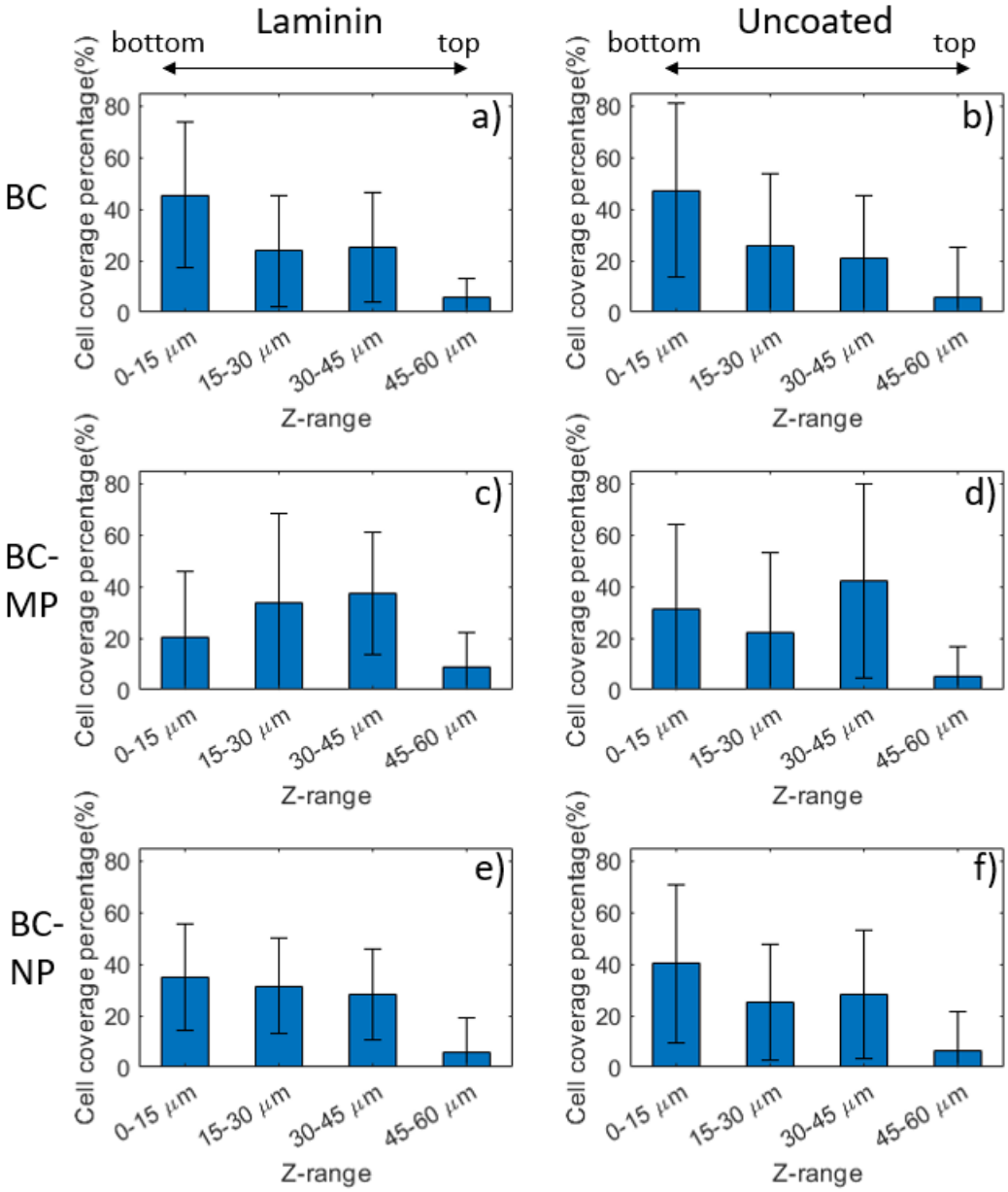

Figure 3.20: The average cell coverage (in %) per cage with respect to the z-range of the cage. Laminin coated in the left column and uncoated in the right column. **a, b** BC, **c, d** BC-MP, **e, f** BC-NP. Donor R09153, with $N_{cages} > 25$ and $N_{cells} > 50$.

The cell density for each cage type is given in fig. 3.21. Here it can be seen that the laminin coated BC(N_{cages}=36,

N_{cells}=378, 2 samples) has on average 3.5 x 10^4 ± 1.61 x 10^4 cells per mm^3, which is higher than the uncoated BC(N_{cages}=27, N_{cells}=108, 2 samples) which has on average 1.92 x 10^4 ± 1.28 x 10^4 cells per mm^3. The laminin coated BC-MP(N_{cages}=50, N_{cells}=288, 2 samples) has on average 2.67 x 10^4 ± 1.56 x 10^4 cells per mm^3, again higher than the uncoated BC-MP(N_{cages}=50, N_{cells}=138, 2 samples) 1.43 x 10^4 ± 8.52 x 10^3 cells per mm^3. The laminin coated BC-NP(N_{cages}=50, N_{cells}=443, 2 samples) has 3.77 x 10^4 ± 1.39 x 10^4 cells per mm^3, which is also higher than the uncoated BC-NP(N_{cages}=30, N_{cells}=127, 2 samples) with 1.96 x 10^4 ± 1.06 x 10^4 cells per mm^3. On average, laminin covered cages have twice as many cells as compared to uncoated cages. Additionally, even though no difference is present in terms of cell density between a non-decorated cage or a nanopillar cage, from the SEM photos it is still obvious that the preference goes to the nanopillar decorated cage as more phenotype variability exists, fewer amoeboid cells are present and more interaction between filopodia and structure exists.

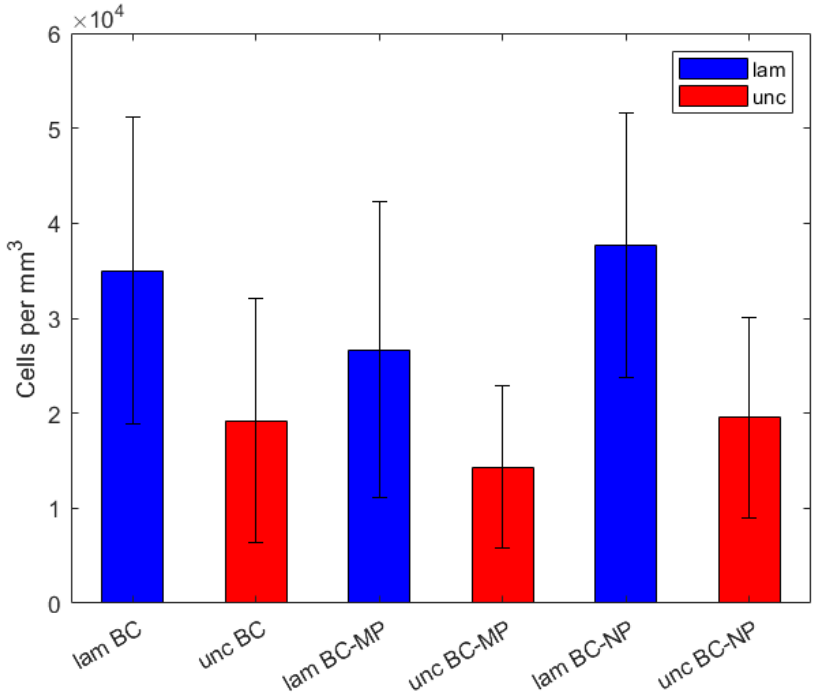

Figure 3.21: Average cell density per cage. Donor R09153, with N_{cages} > 25 and N_{cells} > 50.

Summary of comparison between 2D vs 2.5D vs 3D

The common feature between cells cultured on a flat substrate (2D), on micro/nano-pillar textured substrate (2.5D) and 3D structures, is that all phenotypes appear on the different structures. Still, some inconsistencies exist in cell morphology between the cells cultured on 2D and 2.5D structures, and cells cultured on 3D structures. The 2.5D structures provided a lower effective shear modulus (lower material stiffness), as compared to cells cultured on the 2D fused silica substrate, which contributed to increased cell complexity (+more primary branches) and a higher percentage of ramified cells. The foremost reason for the difference between the cell morphology of 2D and 2.5D, and 3D cell cultures is the third dimension, which allows the cells to extend in an additional dimension. The flat amoeboid phenotype is present on the 3D structures but is wrapped around the structure and therefore does not look flat (2D). The bi-polar and globular phenotypes are also present on both flat substrate and 3D structures, with the morphologies being exactly the same but extending also in the third dimension. The non-amoeboid and ramified cells look similar in morphology in 3D as compared to 2D and 2.5D but now the processes of the cell are not restricted to extending in-plane only but also out-of-plane in the third dimension. Furthermore, the decorated cages provide more variability in phenotypes as compared to the undecorated cages, because the added 2.5D textures provide here again a softer structure and more anchoring points for the cells to attach to.

4

Encountered challenges & Recommendations

In this section, the encountered challenges will be highlighted and if possible the solution for these encountered phenomena will be given. In addition, recommendations will be provided for future studies that are focused on this topic.

4.1. Encountered challenges

In this subsection the mistakes made, technical issues and a tentative explanation of the reported observations are discussed.

4.1.1. Fabrication

Pedestal fabrication

It was discovered through a simulation of the sterilization procedure (see appendix A.6), that structures have a lower chance to detach during the cell seeding step when printed with an interface position of 1 μm instead of the 0.5 μm, therefore this parameter is kept constant for the other structures. Also, using demineralized water instead of PBS decreases the chance of structure detachment, the reason being the lower surface tension of the demineralized water with respect to PBS. The optimization of the dimensions was in favour of the cell experiments. Increasing the area resulted in a better statistical representation of the cell phenotypes present on the pedestal. Also, decreasing the height of the pedestal resulted in a decrease in travel time for the cell to reach the top of the pedestal, and this also greatly reduced the printing time. The printing time is also an important factor that determines the length of the project and is desired to be kept as low as possible. Unfortunately, during the cell seeding step, which is extensive washing of the substrate, the 5 μm thick pedestals mostly detached and curved out of plane. This is probably because the ultra-thin pedestal deforms during prolonged contact with liquid (swelling due to PBS or demi-water) and significant thermal fluctuations (thermal stresses).

Micropillar fabrication

One of the issues that occurred during the micropillar printing, was that the top of the cylindrical-shaped pillars was not round-shaped. Tweaking the printing parameters in a series of dose tests was attempted but due to needing different printing parameters for the addition of the micropillars on top of the cages, this was put to a halt. A different attempt to correct the shape was performed through plasma etching. But unfortunately, this method also did not work, as plasma etching is a homogeneous process as all sides are equally etched, so while the shape of the pillars remained the same, only the dimensions of the pillar did decrease.

Nanopillar fabrication

Collapsing pillars

Large patches of nanopillars collapsed during the developing procedure. This was due to the wet to dry transitions of the samples, that occurred when taking the samples from the PGMEA filled beaker to the IPA

filled beaker and during the evaporation of the IPA. The combination of gravity acting on the droplets (due to the vertical configuration of the sample in the holder) and bending stresses on the pillars (caused by the evaporation of the IPA droplets), is what caused the collapsing pillars. This problem was solved by employing an additional solving agent after the IPA step, called Novec^{TM} 7100 Engineered Fluid (Sigma Aldrich). The lower surface tension of 13.6 Dyne/cm @ 25° for Novec [92] versus 20-22 Dyne/cm for IPA [93] led to less collapsed pillars during the evaporation of Novec. Additionally, a different developing configuration (see appendix A.3) was used for the sample to further reduce collapsing nanopillars. The samples were first placed vertically in the sample holder during the development procedure, but after optimization, the samples were placed horizontally in a Petri dish. This prevented relatively large quantities of droplets from going down through the nanopillar array when displacing the sample into different chemicals during the development steps.

Detachment of nanopillars

Detachment of the nanopillars was encountered during the cell seeding on the finished structures. Although the cells were plated on the structures with care, the applied force was sufficient enough to detach large areas of nanopillars. An attempt was made to solve this problem by using a silanizing chemical called Ormoprime, applied as a thin layer, that would result in better attachment of the structures to the fused silica substrate.
An additional solution was to first print a pedestal and then print the nanopillars on top. The thought behind this was that a pedestal has a larger contact surface with the substrate, and thus a larger force is required to detach the pedestal. Although this solution was promising, the cell seeding proved to still be able to detach the pedestals in most cases, however, some samples with nanopillars survived.
A similar solution was to spin coat a thin film of IP-Dip and then print structures on this layer to increase the adhesion of the structure to the substrate through an intermediate layer. This procedure would take less time to cover the entire area of the substrate with respect to printing a pedestal first for each structure. However, the optimization of this process was deemed too time-consuming, and thus not continued.

Cage fabrication

Cage size

At the beginning of the cage designing process, the lower limit of the structure size was set to a 7 μm wide cage to see what the effect of structure size was on cell behaviour. It was designed with a 1 μm beam diameter so that a 5 μm wide hole would exist in order for the microglia cell to reside in. But based on the cells min Feret's diameter of 2-11 μm, the cell was deemed too large for the 5 μm hole, it was expected that this cage would just be engulfed by the cell instead of providing a stable environment to proliferate. Also, the 1 μm beam diameter seemed to cause structure instability problems during printing due to the beam diameter being too small. For this reason, the lower limit was set to a 25 μm wide cage with a 5 μm beam diameter instead, resulting in a 15 μm hole, which was estimated to be sufficiently large for the cell.
For the upper limit, a 70 μm wide cage was designed with a 10 μm beam diameter, resulting in a 50 μm wide hole for the microglia cell to reside in. However, the surface area within this cage was deemed too high (2500 μm^2) with respect to that of the cell area (9.11- 111.9 μm^2). So reducing the beam diameter to 5 μm for consistency purposes and the cage width to 50 μm (only twice the size of the 25 μm cage), resulted in a 40 μm wide hole and a lower surface area(1600 μm^2) deemed more suitable for the cell to proliferate in.

The sequential printing method

Although this sequential printing method was a good solution for the purpose of printing the nanopillars individually onto the cages, it still had some issues to solve. One of those issues came to light when the cage was printed first, and the pillars directly after that. The already printed top of the cage caused shadowing, meaning that the laser could not reach certain positions underneath the top of the cage, resulting in unprinted pillar structures on the vertical beams and underneath the top of the cage. This was solved by printing each section of the cage (bottom, vertical beams and top) with the respective pillars in steps, as seen in appendix A.5.

Angular printing of nanopillars on 50 μm cage

The nanopillars on the 50 μm cage with a hatching and slicing distance of 0.2 and 0.25 μm respectively, when printed at an angle of 60° with respect to the x-z and y-z plane resulted in non printed pillars. This was solved by decreasing the hatching distance of the pillars to 0.1 μm. Also, the multi-pass printing method was tried to use a lower laser power and writing speed while passing the structure twice in an attempt to create a finer tuned diameter pillar, but the printing speed was twice as long so this option was not viable.

Cage detachment

Even though the 3D structures survived the sterilization procedure, the structure detachment issue occurred as well for the un-/decorated cages (both 25 and 50 μm) during the cell seeding step. This problem was minimized by using the same Ormoprime layer as for the pillars.

4.1.2. Cell experiments

Pedestal experiments

The reason behind the lack of data of the microglia cells on the pedestals for the first 2 experiments, was due to the fact that the cell phenotypes could not be distinguished due to the fluorescent images being not clear enough. The reason for this might have something to do with the autofluorescence of the pedestal interfering with the immunofluorescence of the cell staining, however, this could not be verified. Also, for the SEM pictures, there were not enough samples to perform the analysis on (less than 20, and most were amoeboid). Finally, although the pedestals survived the simulation of the sterilization procedure, in the later experiments all the pedestals except for 1 were washed off during the cell seeding step. There simply was no data to make a comparison between donors.

Usage of a laminin coating

It was shown that a laminin-coated substrate provides a lower ramified phenotype percentage and less complex ramified cell with respect to an uncoated substrate and for micropillars, no difference exists in complexity, but still, a lower ramified percentage for the laminin-coated micropillars. However, laminin plays a role in the attachment of the cell to the structure. Although no significant difference was seen between the laminin-coated and uncoated substrate cell density (cell/cm^2), the difference becomes clearer when introducing IP-Dip structures. The difference increased even more when observing the 3D structures in which the laminin-coated undecorated and decorated cages, had a cell density (cell/mm^3) of approximately 2 times that of the uncoated undecorated and decorated cages.

Cell membrane rupture caused by dehydration protocol for SEM imaging

One of the encountered problems during the microglia cell culture on the micropillars was the rupturing of the cell membrane. This was the result of cell membrane shrinking in between the pillars caused by the dehydration protocol used for preparing the cells for SEM imaging. We tried to solve this problem by adding an additional drying chemical, called HMDS, in combination with decreasing the weight percentage of PFA and GA in the ethanol bath the cells were dehydrated in. The usage of HMDS led to less cell membrane shrinkage.

Cage experiments

The fact that fewer cells tried to phagocytize the 50 μm cages than the 25 μm cages, could be an indication that the 25 μm wide cage is at the lower threshold of foreign body objects small enough to be phagocytized

by microglia cells. For this reason, the 50 μm wide cages were chosen for the continued experiments, as the phagocytic behaviour of the cell is undesirable.
The size of the 25 μm wide cages seemed to be too small for the cell to see any desired effects. The shape of the cell body seemed to be guided by the shape of the cage, resulting in unnatural cell morphologies not typically seen in vivo, and thus further experiments with these cage dimensions were cancelled.
Some cells wrapped around the cages in a way that resembled the foreign body response, as the cells tried to phagocytize the cages. This seems to be less for the cages that have the micro-/ nanopillars as decoration. This might be because the bending pillars make it seem as if the material's stiffness is slightly softer and more resembling the brain tissue than the cages without any decoration.
Although a shift in cell occupancy was seen when adding micro-/and nanopillars as decoration to the cages. It is not significant enough to conclude that this was definitely caused by the added nanodecoration.
Ormoprime was used to increase structure attachment strength/ adhesion strength to substrate and Laminin to increase cell attachment to the structure. The combination of these two products resulted in the unwanted phenomenon of increased attachment of red blood cells to the substrate and 3D structures. This effect was not predicted but in hindsight would be normal as the laminin coating should have a positive effect on the attachment of cells, red blood cells not excluded.

4.2. Recommendations

Fluorescent images

The usage of low autofluorescence material is necessary to be able to perform meaningful morphological analysis of microglia cells on 3D structures. Our own study showed that the autofluorescence of the structures (green channel) caused interference with the immunofluorescence staining of the cell nuclei (blue). This was the case for the Hoesch staining but not the DAPI staining (both blue staining of the nuclei). The reason for the interference was probably because the emission spectrum and excitation spectrum of the Hoesch and DAPi staining overlapped with that of the IP-dip material, but unfortunately, that does not explain why the interference did not occur for the DAPI staining. Maybe the 488 nm excitation source that was used for the confocal microscope caused this interference.
However, this problem was solved by splitting the RGB colour (red, blue, green) pictures in separate channels, using ImageJ, we could adjust the contrast of the respective images so that they would match in brightness. Then the green channel was subtracted from the blue channel in ImageJ (process>math>subtract mode) this resulted in an image in which the structures were filtered out in the blue channel.

Morphology analysis of cells on 3D structures possible?

Although it is possible to do a morphology analysis on cells within 3D structures, it is not recommended as the cell membranes overlap making it almost impossible to distinguish individual cells. A solution might be to add an additional fluorescent marker that binds to a protein in the cell membrane, which will help in distinguishing the cells from each other (F-actin for example).

Structure detachment avoidance

In the future, it is necessary to prevent structure detachment during the cell seeding step. This can be realised by providing the microglia in a medium in which the cells are already separated from red blood cells and other undesired cells. Then the rinsing step in the microglia seeding protocol, which washes out red blood cells and detaches structures, does not need to be performed. Another solution is to prevent the detachment of the pedestals specifically. This detachment could be caused by out-of-plane bending of the thin film due to thermal stresses forming within the material by a combination of high surface-to-mass ratio and one-sided rapid cooling. A second possibility is that the bending is caused by swelling, due to the absorbance of the cell culture medium. This can be prevented or reduced by cutting grooves in the surface perpendicular to the bending direction. or just make the entire surface consists of smaller squares that are not joined at the edges.

Larger structure covered areas

Larger areas covered by the desired structures are needed so that the extracted data can be statistically relevant and so that studies can be performed for which large amounts of cells are needed (gene expression

studies). For the micro-and nanopillar arrays, the suggestion would be to go for classical photo-lithography, to have a mask of larger areas printed, followed by Drie etching. This, however, is done with silicon wafers which have a higher young's modulus (125-180 GPa [94]) than IP-Dip and thus might not give the desired effect as the IP-Dip pillars do (as these are less compliant). But this effect might be compensated by making high aspect ratio pillars, meaning a high pillar with a small diameter.

High-throughput technique for 3D structure fabrication

To increase the throughput of the undecorated cages, the 25x objective could be used. This objective has a lower resolution with respect to the 63x objective, but a higher printing speed is possible. However, for the micro- or nanopillar decorated 3D structures, high throughput is not possible with the 25x objective because the fine features of the nanopillars can not be printed with this objective.

Usage of non-autofluorescent material

The usage of non-autofluorescent material for the fabrication of the structures would prove to be useful when identifying cells cultured on 3D structures. This was no problem for cells cultured on flat surfaces or 2.5D structures but poses a problem when the cells are on the 3D structures as the structures might interfere with the signal of the fluorescent markers.

Stabilize setup for the confocal microscope

The sample is positioned at the bottom of a Petri dish, and as PBS or water might get underneath the sample, this will result in a small tilt that affects image quality. Providing a stable setup will prove to be desirable when imaging nanoscale features of cells such as filopodia.

Usage of 2.5D and 3D structures in cell cultures

The usage of nanopillars would be most suitable for 2D/2.5D cell cultures focused on microglia morphology research due to the more in vivo like morphology of the cell and the higher percentage of ramified cells. However, it is recommended that if laminin is used, to use it in combination with other biochemicals. The reason is that using just laminin results in a lower percentage of ramified cells as compared to not using it. For gene expression studies the preference goes to 3D structures combined with a smaller substrate and substrate holder (well plate), to reduce the usage of cell medium while having a high cell density for the same amount of surface area as compared to a classical 2D culture. Additionally, it would be wise to use laminin here as it does increase the cell density by twofold as compared to not using it.

5

Conclusion

This thesis was a pilot study in which we employed the two-photon-polymerization technique and the biocompatible material IP-Dip, to create an ***in vitro*** platform that provided a more ***in vivo*** like ramified microglia cell morphology both on 2.5D and 3D structures as compared to normal 2D ***in vitro*** studies.

Although not statistically significant, due to an insufficient amount of samples, this study has shown that the addition of physical cues (2.5D structures) can be used to increase the degree of ramification, the number of primary branches and increase the percentage of ramified cells present in a culture with respect to cells cultured on a fused silica substrate (2D). Additionally, this research is relevant in the sense that an increase in ramified cells can be achieved, while culturing the cells on nanopillars made out of a relatively stiff material ($\approx 1 \times 10^6$ stiffer than the brain). By bending in direction of the forces exerted by the cells, the material's effective shear modulus of the nanopillars appears to be $\approx$ 4250 times lower than the bulk modulus and thus the material creates the impression of being softer to the cell. This results in homeostatic microglia being cultured on a stiff complex structure providing enough structural stability, without the need for a soft material having a brain-like Young's modulus.

Also, from the results, it is apparent that adding laminin as a biochemical coating on micropillars does not increase the percentage of ramified cells in culture. Coating a fused silica substrate with laminin even has a negative effect on the degree of ramification of a ramified cell with respect to an uncoated substrate. However, it does result in a higher cell density on the pedestal, pillar and cage structures, with even a cell density that is twice as high in both laminin-coated undecorated and decorated cages as compared to the uncoated versions.

Furthermore, microglia on 3D structures show the same phenotypes as in 2D culture but display a more ***in vivo*** representable cell morphology that extends in the third dimension. This is the reason for the flat amoeboid cell (2D) to be an enwrapping amoeboid cell in a 3D environment and for the ramified cell to extend the primary branches out-of-plane.

Another observation was that the size of the cages played a role in the phagocytic behaviour of microglia cells. The 25 μm cages appeared to be more engulfed by microglia with respect to the 50 μm cages, indicating that a size threshold exists for phagocytosis. Lastly, the interaction of the filopodia with the micro-/nanopillars on the decorated cages is different than with undecorated cages. The filopodia on the decorated cages extend in more directions as compared to undecorated cages. While providing more anchoring points for the cells, the pillars instigated more cell migration towards the top of the decorated cages and fewer amoeboid phenotypes being present on the decorated cages as compared to undecorated cages, while still having approximately the same cell density.

6

Self-reflection

What did I learn during this project?
I learned that the gap between theory and practical application is quite a hurdle to overcome, but not impossible when certain problems are approached with a well-devised step-by-step plan born from creative thoughts. Technical issues or insecurities between the micro/nano-engineering and the cell-biology field were eventually the problems that proved to be the most difficult ones to be solved. Thankfully, good communication between both fields led to solving most of the problems.

What went well?
Improvising in combination with risk prevention (back-up plans), in case certain cultures would go wrong or structures would not be printed before certain deadlines. Solving technical issues that came into play while trying to set up certain experiments. The quality of the SEM images greatly improved w.r.t. the beginning of the project.
A lot of experiments on different structure types and conditions were performed that are deemed relevant, in a relatively short amount of time, providing a broad basis for future studies.

What could have gone better?
More in between reading of literature could have prevented some minor hold-ups. Better planning on what to do with certain data. Better planning of what should be in the report and additionally taking into account which pictures to include so that images might be taken during experiments beforehand. More frequent breaks of a couple of days in between weeks of continuous work, in order to rest the mind and take a different viewpoint on the work done to see if it still progressing in the right path and also to get a better overview of the work that is done. This is because continuous labour without breaks might result in tunnel vision.

What would I have done differently?
During the experimental part, I realised that the scope of my study was extraordinarily broad. The amount of time invested in this project might be closer to the beginning of a PhD. I could have spent my time more efficiently by focusing on fewer structures or less partial experiments. Nothing is wrong with having an ambitious project, but one should always be more realistic regarding time planning.

All in all, I am happy with the amount of work I delivered, and the results and insights that I gained during my experiments. In my view the results gained, prove to be useful for future studies in both the bioengineering and biomedical fields.

A

Fabrication

A.1. Structure fabrication procedure

The process that was followed step-by-step for the printing of each structure is the following:

1. Clean fused silica (25 mm) substrate with a fine cleanroom cloth with some acetone
2. Then clean substrate with IPA covered fine cloth
3. Blow-dry the sample
4. Oxygen Plasma cleaning (Diener oxygen plasma cleaner) of the surface at 80% power (of 100 W) for 5min (gas flow rate at 5 sccm)
5. Place substrate in the middle of the spin coater
6. Deposit 7 droplets with a small pipette on the substrate
7. Turn on spin coater at 4000 rpm for 60 sec, with an acceleration of 1080 rpm
8. Post bake 5min at 150°
9. Place substrate in the Nanoscribe sample holder, and fix the sample in place with tape around the edges
10. Deposit one droplet of IP-Dip (or any other negative-tone photoresist)
11. The Sample holder is placed in the Nanoscribe printer, the print job is uploaded and the printing process follows
12. The sample holder is taken out of the printer and the samples are placed on a fine cloth, with the resin side pointing upwards
13. The sample is carefully submerged horizontally in a Petri dish filled with PGMEA for 25 min
14. The sample is carefully submerged horizontally in a Petri dish filled with IPA for 5 min
15. The sample is carefully submerged horizontally in a Petri dish filled with Novec 7100 Engineering Fluid for 30 seconds
16. The sample is carefully removed from the Petri dish then tilted 45° and carefully blow-dried with an air-gun
17. Oxygen Plasma functionalization (Diener oxygen plasma cleaner) of the surface at 80% power (of 100W) for 20 s (gas flow rate at 5 sccm)

A.2. Structure Optimization

A.2.1. Dose test pedestal

For the pedestal dose test, a 20 μm wide and 10 μm in height pedestal was used. The laser power (LP) varied from 20 % to 80 % in steps of 20 % in the y-direction and two ranges were used for the writing speed (WS). The first range of WS varies from 5k μm/s to 20k μm/s in steps of 5k μm/s, and the second range varies from 30k μm/s to 60kμm/s in steps of 10k μm/s, as can be seen in fig. A.1. The reason behind the chosen printing parameter range is to check the extremes of printing. Also, printing parameters were needed in order to provide prints with a large enough surface area, using a high printing speed to reduce printing time. On the other hand, high-resolution prints were needed later on in the project to be able to print the nanoscale dimensions of the pillar arrays and decoration on the cages. It was assumed that such fine dimensions could only be printed using a low LP and WS. But, it turned out this was not the case. In fig. A.1, one can see that for 20 % LP no pedestal were printed(polymerized). Also, black spots can be seen at high LP and low WS. This is due to laser overexposure and is undesirable. Furthermore, detachment of the structure is also undesirable as the structures still need to be subjected to sterilization and a cell seeding step. So, The ideal printing parameters are those that result in pedestals without black spots and are still attached to the fused silica substrate; LP at 60 % and writing speeds at 10k, 15k, 20k and 30k μm/s, and LP at 80 % with the writing speeds at 40k, 50k, and 60k μm/s. As a high printing speed resulted in a reduced overall printing time, the combination of a LP at 80 % with a WS of 60k μm/s was chosen.

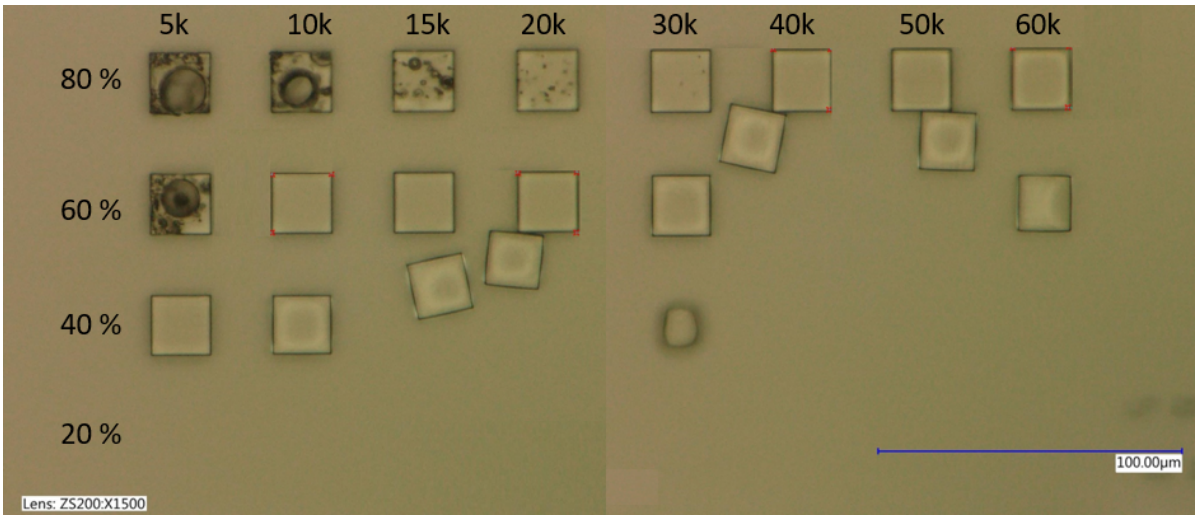

Figure A.1: Dose test pedestal. The vertical axis shows the LP percentage and the horizontal axis shows the WS in μm/s. Black coloured bubble formation is due to overexposure to the laser.

A.2.2. Dose test micropillars

The micropillars were printed first in preparation of the nanopillars, this was because the nanopillar dimensions were really pushing the limits of the Nanoscribe machine and therefore it was not certain that these structures could even be printed in big arrays with the desired length and diameter. The length of the pillar was designed at 2.5 μm, the diameter at 1 μm and printed with a hatching distance of 0.2 μm, a slicing distance of 0.25 μm and at an interface position of 1 μm. The pillars were in an array of 26x26 with a minimum distance of 1 μm resulting in a 51 μm x 51 μm array. Because the mass/volume of these micropillars were several orders of magnitude smaller than the pedestal, it was assumed that due to the smaller heat capacity of this smaller body, the ideal printing parameter set must be different than that of the pedestal. Therefore, the decision was made to do a dose test with a larger range of printing parameters. In fig. A.2, it can be seen that for the printing parameters on the left side of the image, the LP ranges from 10 % to 45 % in steps of 5 %, and the WS ranges from 10k μm/s to 25k μm/s in steps of 5k μm/s. It is directly apparent that for a LP of 30 % and lower and WS of 10k μm/s up-till 25k μm/s, the structure did not polymerize. The same goes for a LP of 35 % and writing speeds 15k, 20k and 25k μm/s, and also 40 % LP with a WS (WS) at 25k μm/s. The ideal printing parameters were: 1) WS 30k μm/s and LP 60 %, 2) WS 10k μm/s and LP 45 %, and 3) WS 40k μm/s and LP 70 %.

After adopting the same LP (85%), WS (60k μm/s), hatching distance (0.2 μm) and slicing distance as for the nanopillars, a hatching test was performed to optimize the shape of the micropillar. In fig. A.3 the hatching test shows that the best micropillar shape is on the left side of each hatching distance, on the edge of polymerization (lower LP results in unprinted structures). This however proved to be a very time-consuming process and was not continued. Later on in the project, the combination of a LP 70% and a WS of 30 mm/s was chosen for each structure as this provided all structures to be printed.

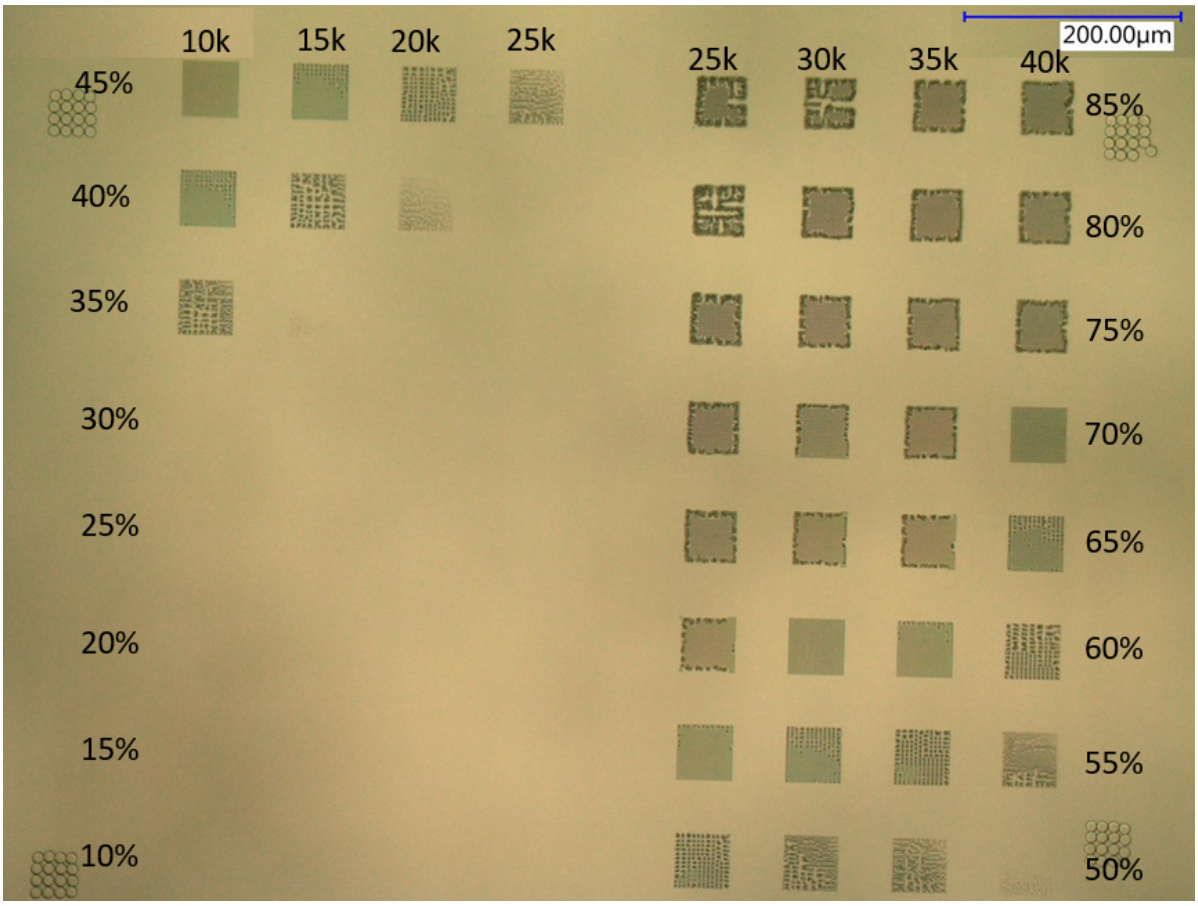

Figure A.2: Dose test micropillars. The vertical axis shows the LP percentage and the horizontal axis shows the WS in μm/s.

A.2.3. Dose test nanopillars

The Dose test for the nanopillars was performed in 2 parts for both parts the LP was increased with steps of 5 μm and the WS with steps of 5 mm/s. In the first part (fig. A.4), the pillars were mostly not printed for a LP between 10-45 % and a WS of 10-25 mm/s. More promising results were for a higher LP 50-85 % and WS between 35 and 40 mm/s. Therefore in part 2, the LP was between 50-85 % and the WS between 35-60 mm/s (still steps of 5 were performed for both the LP and WS). The best results were for LP 85 % and a WS of 60 mm/s.

A.2.4. Dose test cages

A preliminary dose test for the cages was done to find out what combination of WS and LP results in polymerized cages. After that, the set of printing parameters was fine-tuned, to have cages with better resolution.

The ideal printing parameters, while having a balance between a high speed and high resolution, for the 25 μm and 50 μm cages are indicated as the cages in between the red lines drawn, see fig. A.9.

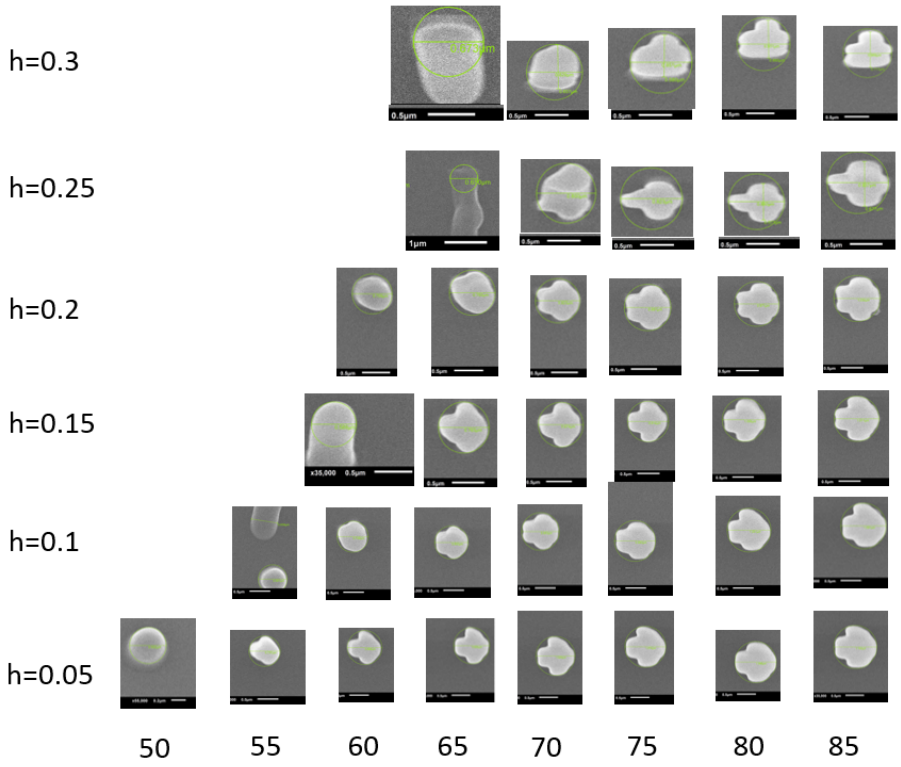

Figure A.3: Hatching test micropillars at 60 mm/s WS. The vertical axis shows the hatching distance in μm and the horizontal axis shows the LP in %.

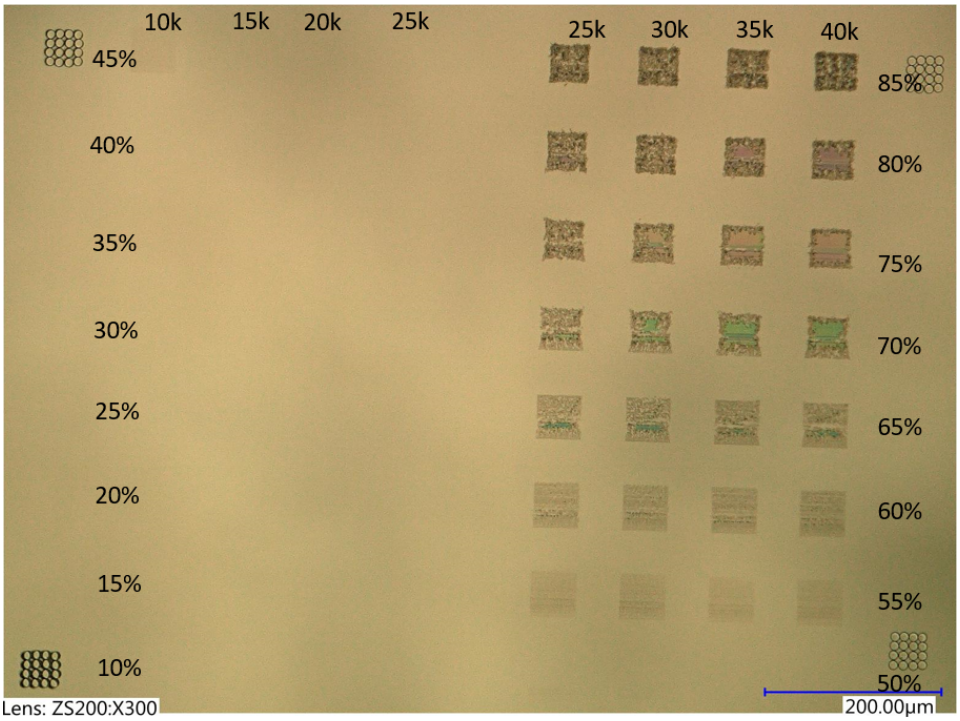

Figure A.4: Dose test nanopillars part 1. The vertical axis shows the LP percentage and the horizontal axis shows the WS in μm/s.

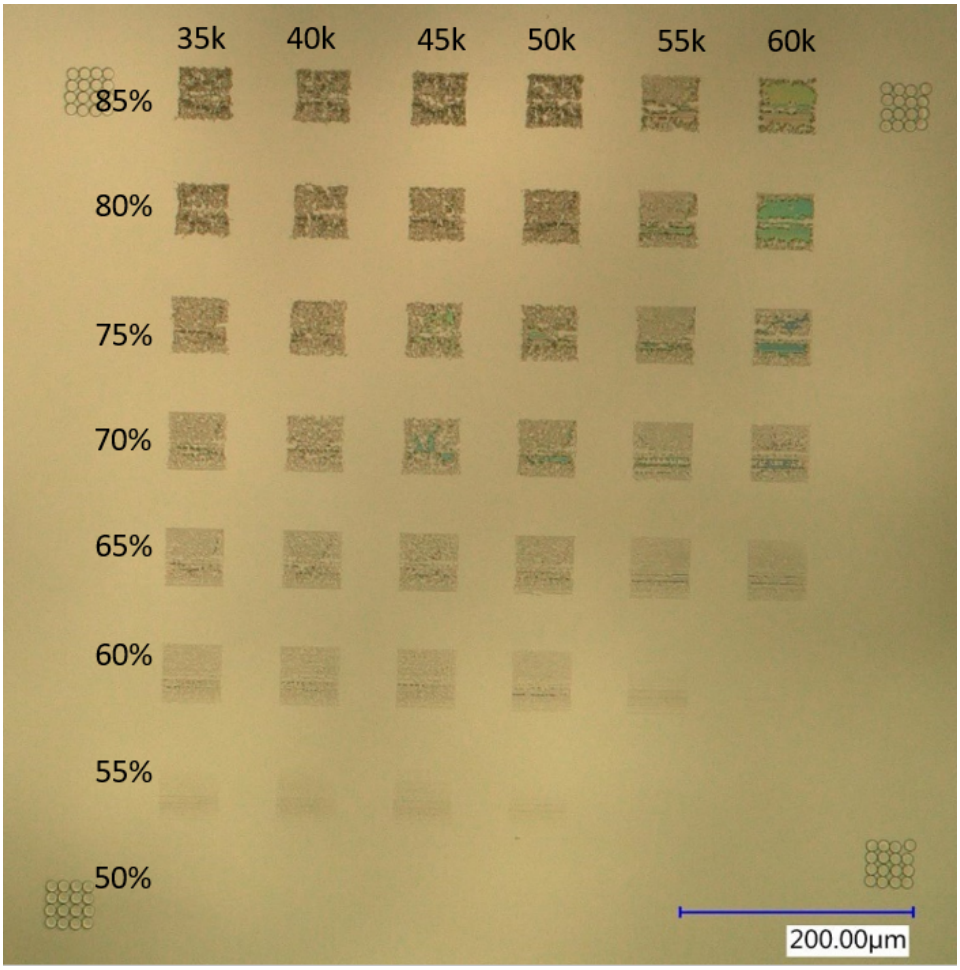

Figure A.5: Dose test nanopillars part2. The vertical axis shows the LP percentage and the horizontal axis shows the WS in µm/s.

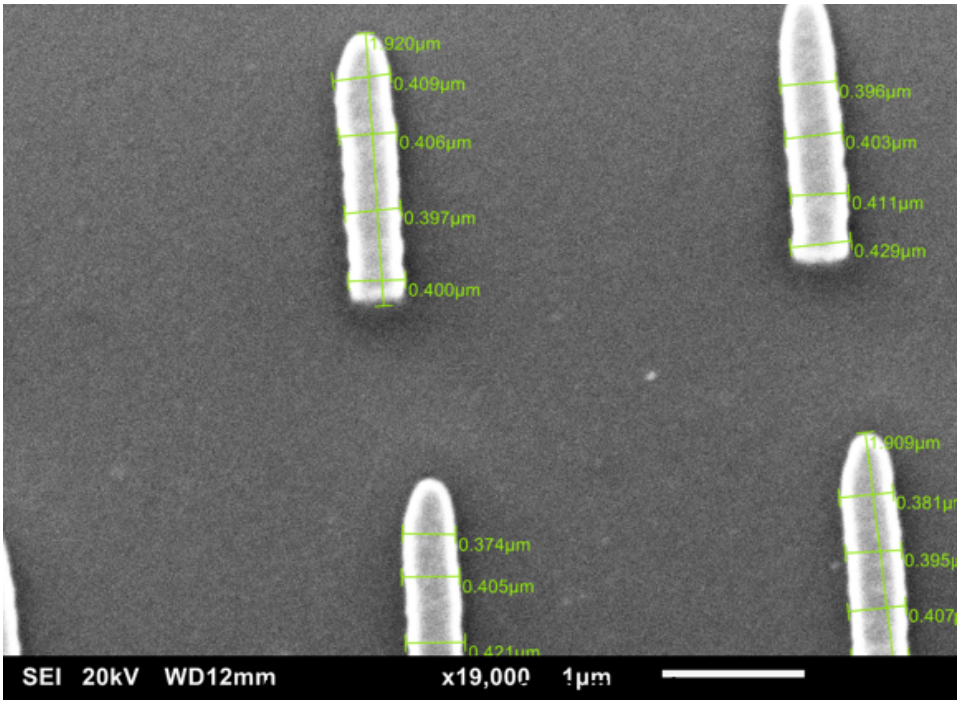

Figure A.6: SEM image with measurements of NP1, printed with LP 85%, WS 60mm/s, h=0.2µm, s=0.25µm, IP=1µm

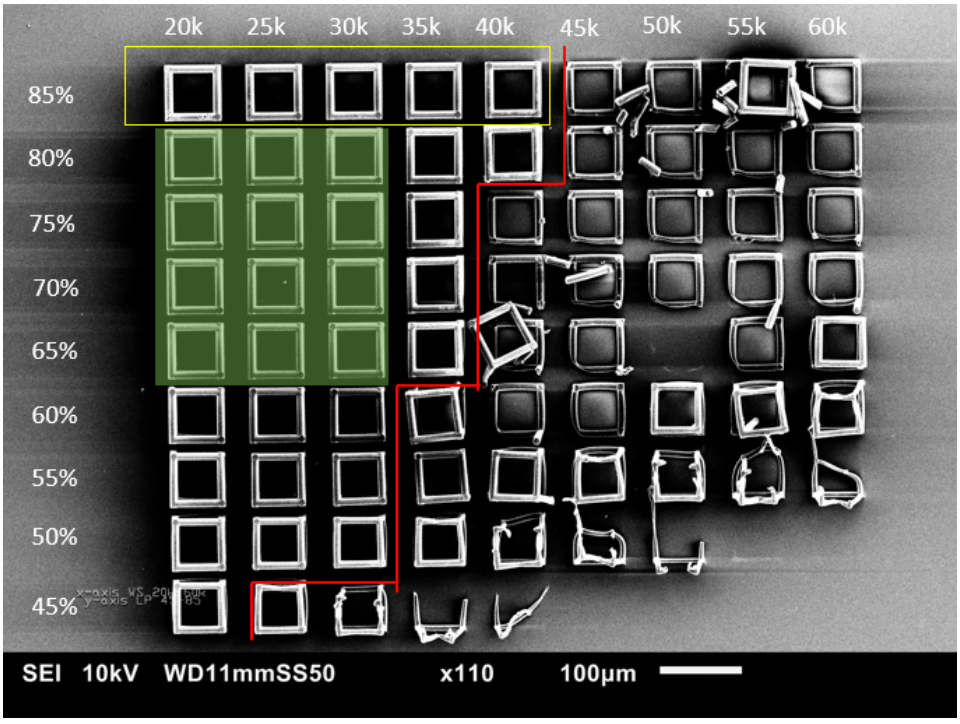

Figure A.7: Dose test 70µm cage, LP on the vertical axis, and WS on the horizontal axis. The cages left of the red line were fully printed, but some were warped. The yellow square shows fewer warped cages, but with minor black spots due to overexposure. The green area shows the optimal printing parameters.

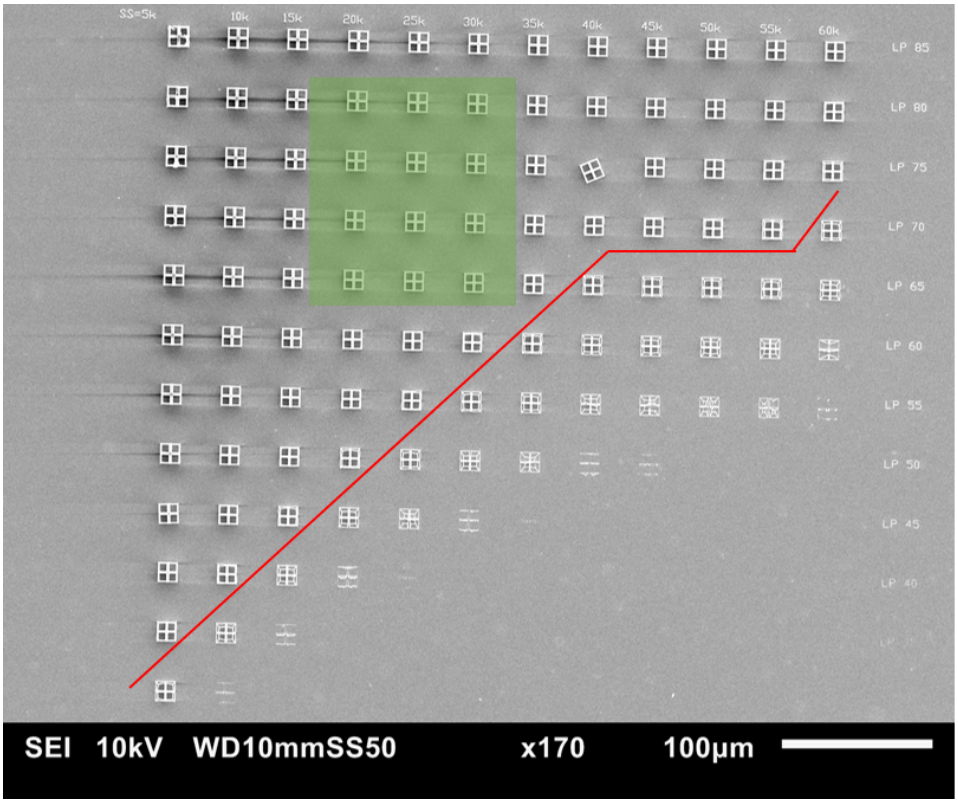

Figure A.8: Dose test 7µm cage, LP on the vertical axis, and WS on the horizontal axis. The cages above the red line were printed. The Green area shows optimal printing parameters.

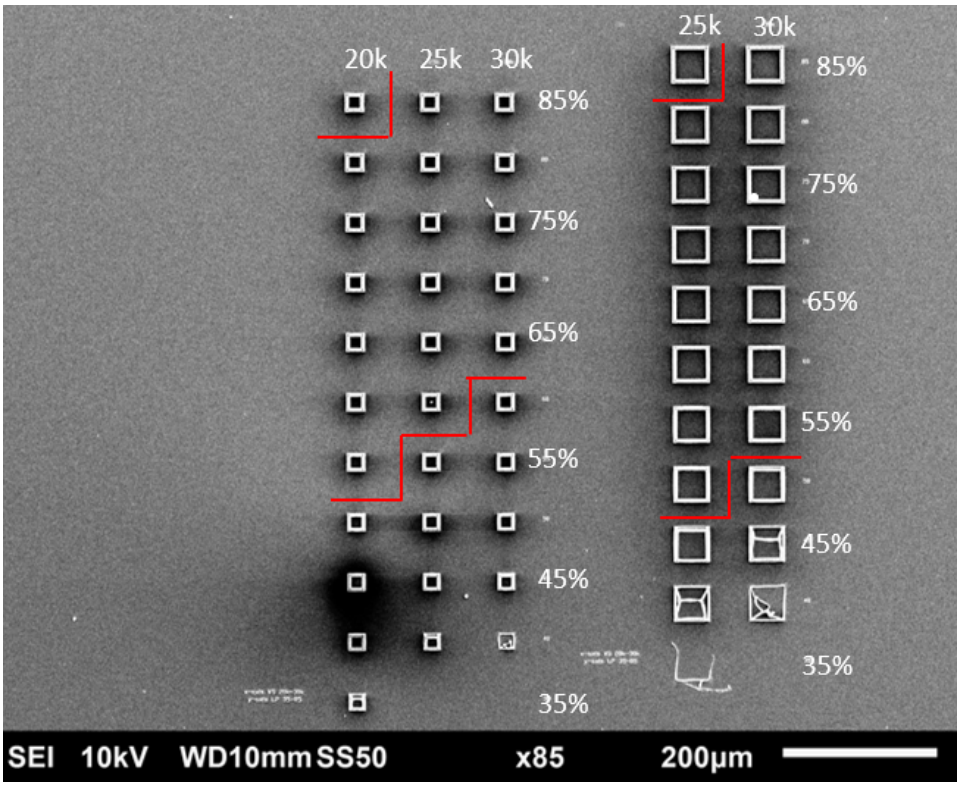

Figure A.9: Dose test 25 µm and 50 µm cage. The cages in between the red lines are printable. LP on the vertical axis, and WS on the horizontal axis.

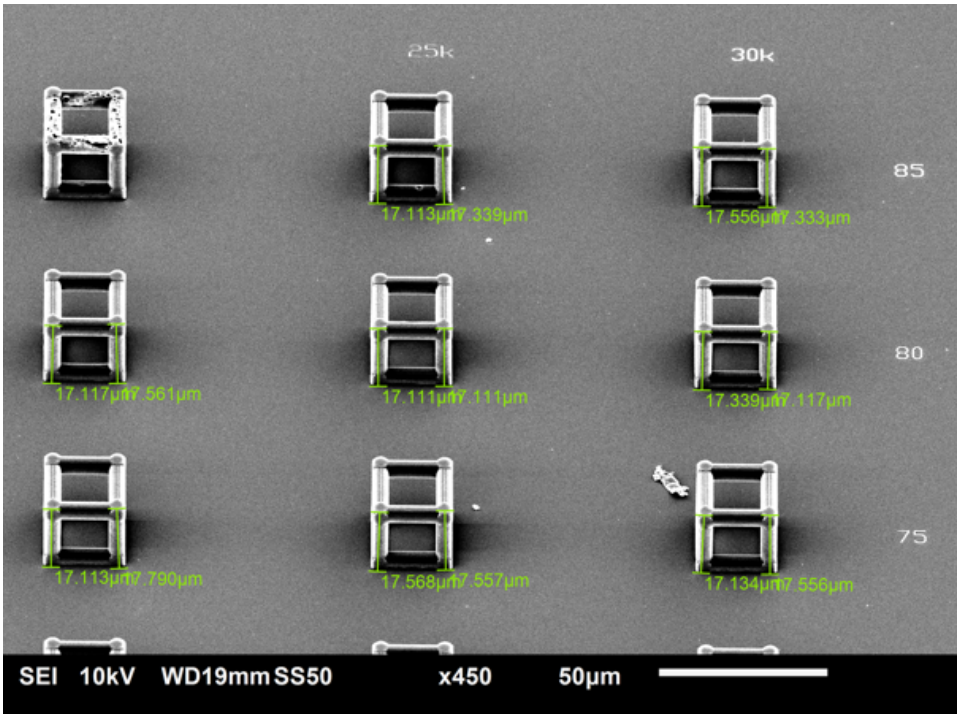

Figure A.10: SEM image of an isometric view of dose test 25 µm cage. Measurements part 1.

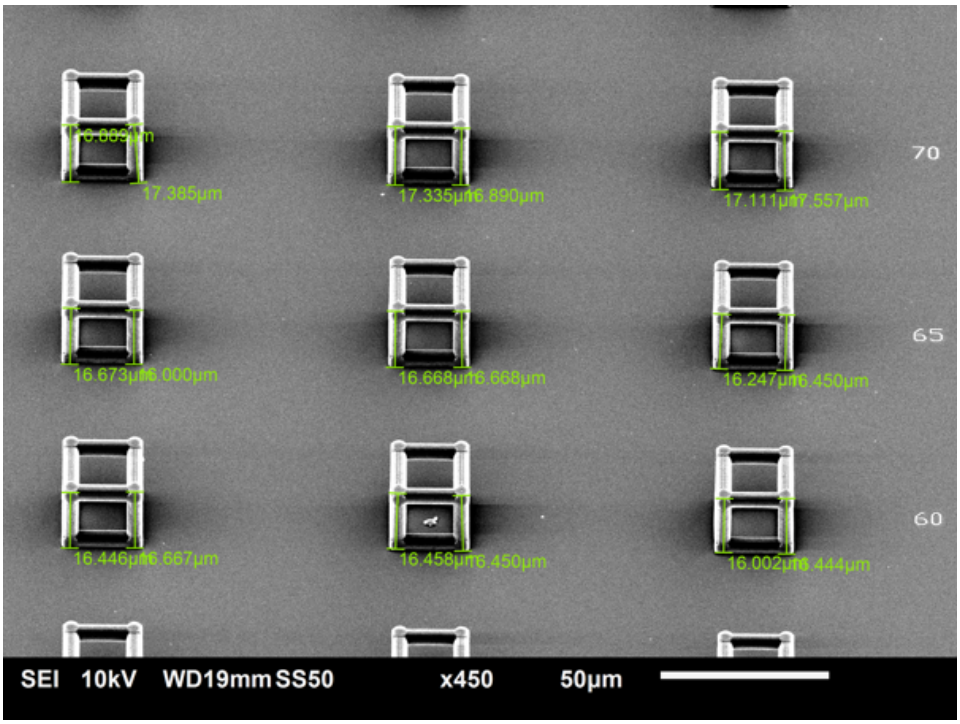

Figure A.11: SEM image of an isometric view of dose test 25 µm cage. Measurements part 2.

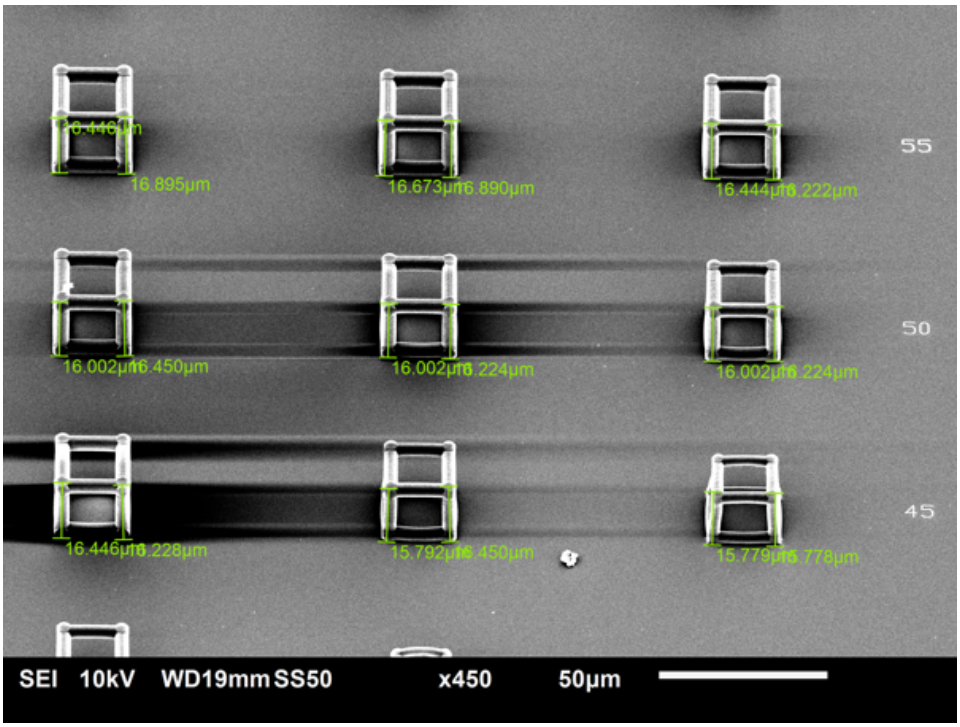

Figure A.12: SEM image of an isometric view of dose test 25 µm cage. Measurements part 3.

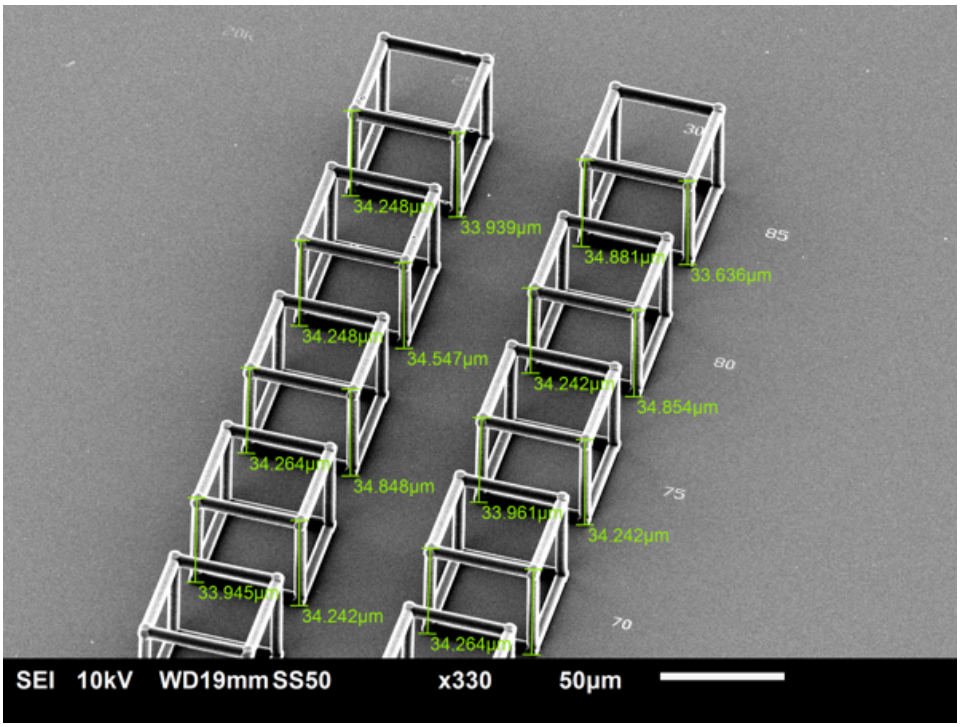

Figure A.13: SEM image of an isometric view of dose test 50 µm cage. Measurements part 1.

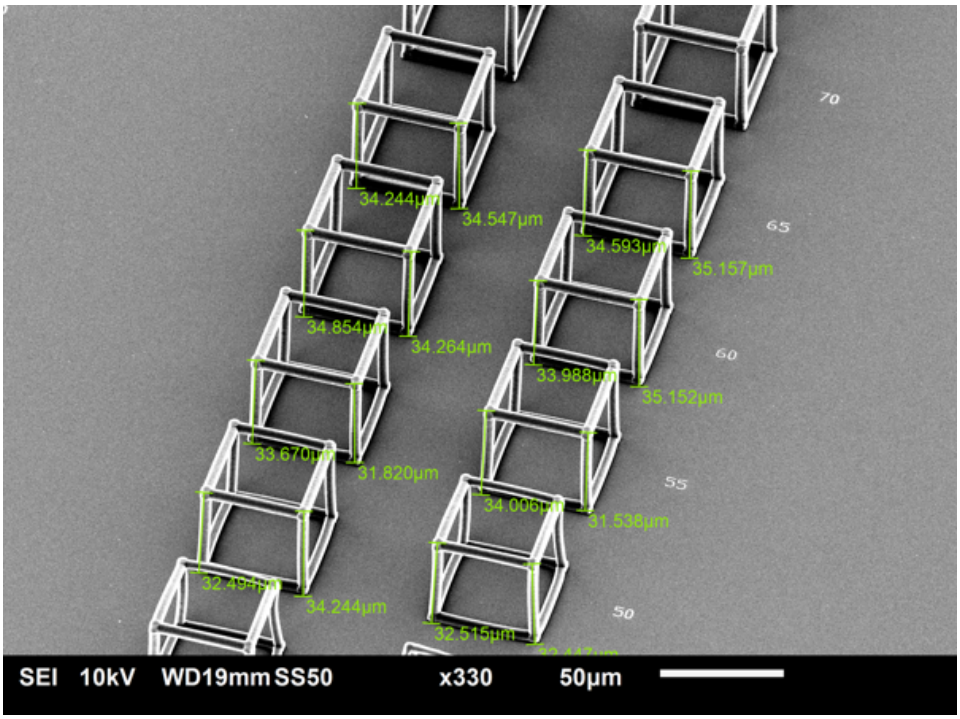

Figure A.14: SEM image of an isometric view of dose test 50 µm cage. Measurements part 2.

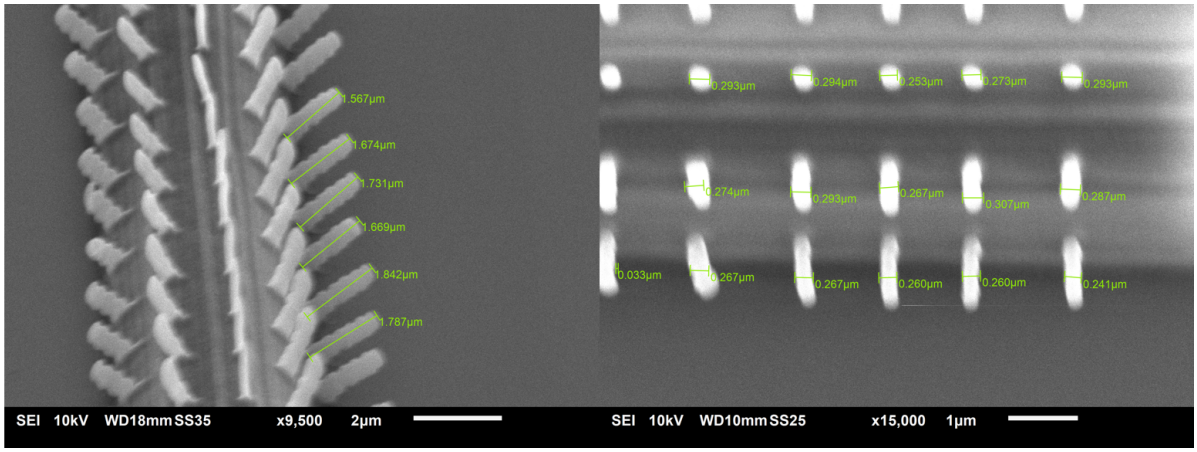

Figure A.15: SEM image with measurements of NP LP 70%, WS 30mm/s, h 0.1µm, s 0.25µm, on BC. (left) 45° tiled view. (right) top view.

A.3. Development procedure optimization (IP-Dip nanopillars)

What was looked into was optimizing the development procedure in order to prevent the nanopillars from collapsing. Novec was used because of the low surface energy, resulting in lower forces acting on the pillars when the sample was blow-dried with a ball blower. At first, the added Novec seemed to worsen the situation. But the discovery was made that sample orientation in the sample holder played a role in pillar collapse as well. A vertical orientation of the sample resulted in more collapse than having a horizontal orientation of the sample. The probable reason behind this is that when the sample emerged from the development agent PGMEA, tiny droplets ran down the pillars, exerting a high enough force to collapse the pillars.

The old procedure was:

1. Submersion of the sample, with a vertical orientation in PGMEA for 25 min
2. Submersion of the sample, with a vertical orientation in IPA for 5 min
3. blow-drying of the sample

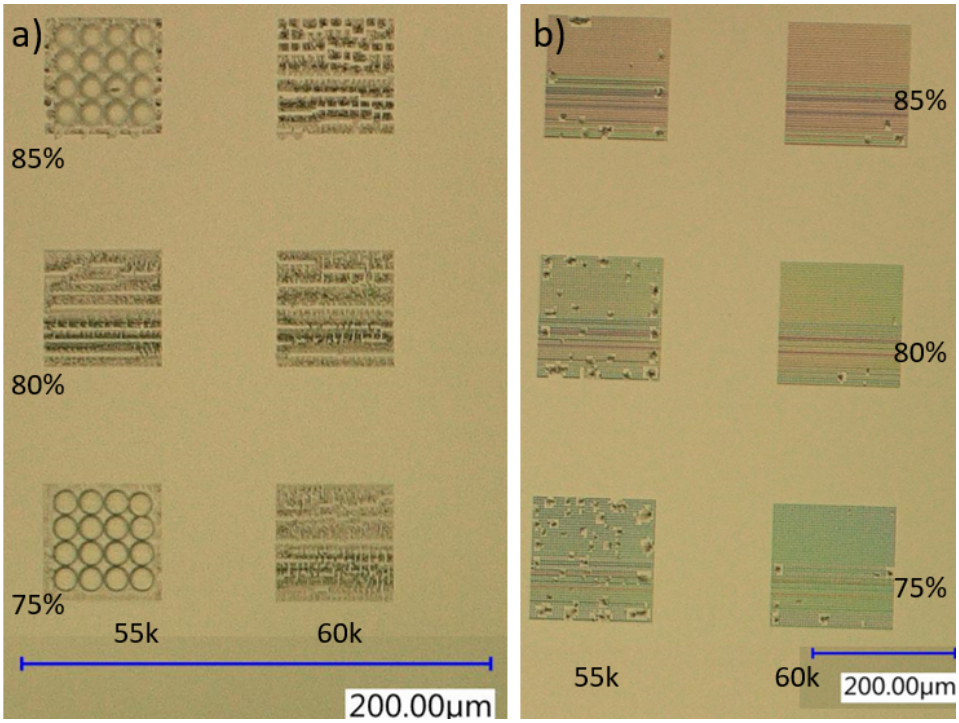

Figure A.16: Keyance image of nanopillars after development step. The horizontal axis represents the WS and the vertical axis the LP. **(a)** vertical submersion of sample in Novec, **(b)** horizontal submersion of sample in novec.

The new procedure involved using Novec after the IPA step (fig. A.16a):

1. Submersion of the sample, with a vertical orientation in PGMEA for 25 min
2. Submersion of the sample, with a vertical orientation in IPS for 5 min
3. Submersion of the sample, with a vertical orientation in Novec for 30 sec
4. blow-drying of the sample

Unfortunately, this made the collapsing pillars worse. The situation was improved by simply placing the sample horizontally in a Petri dish (fig. A.16b):

1. Submersion of the sample, with a horizontal orientation in PGMEA for 25 min
2. Submersion of the sample, with a horizontal orientation in IPS for 5 min
3. Submersion of the sample, with a horizontal orientation in Novec for 30 sec

4. blow-drying of the sample

A.4. OrmoPrime thin film coating procedure

1. Cleaned fused silica 25 mm substrate with acetone and IPA
2. Plasma treatment of surface (80 % of 100W for 5min, O_2 5ccm)
3. Deposit 7 droplets with a small pipette on the substrate
4. Turn on spin coater at 4000 rpm for 60 sec, with an acceleration of 1080 rpm
5. Post bake 5min at 150 C deg

When the procedure is followed step-by-step, the thickness should be near 130 +/- 15 nm.

A.5. Sequential printing of decorated cages

The first sequential printing of the BC-NP (using 6 steps), as seen in fig. A.17, resulted in shadowing caused by the top part of the print causing unprinted pillar structures on the vertical beams of the cage (fig. A.18).

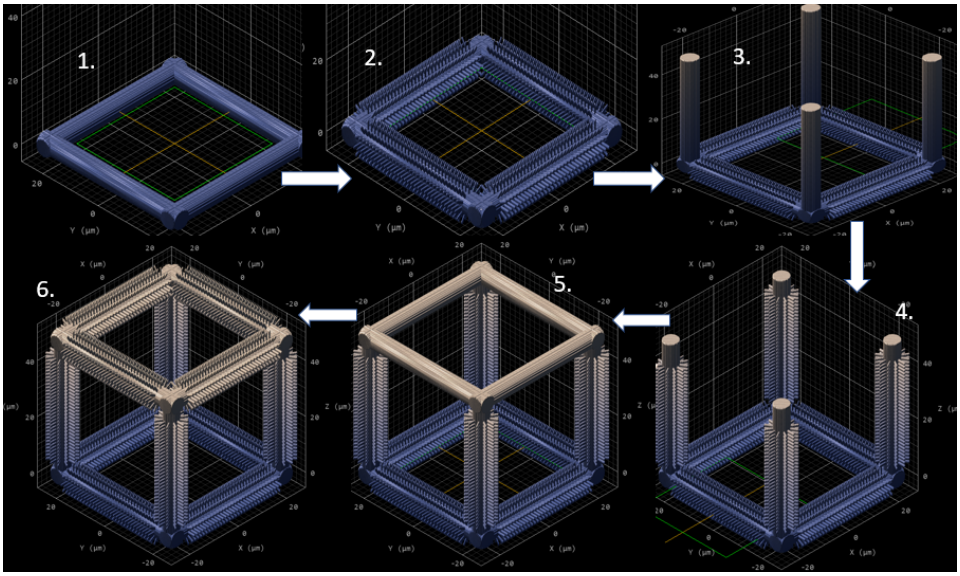

Figure A.17: Sequential printing of BC-NP in 6 steps.

A.6. Sterilization procedure

The sterilization step was simulated, in order to observe if any problems would arise regarding the printed structures. The sterilization procedure as performed by the BPRC consists of incubation in a Petri dish:

1. 5 min ethanol 50% incubation
2. 5 min PBS incubation
3. 5 min ethanol 70% incubation
4. 5 min PBS incubation
5. 5 min ethanol 99.9% incubation
6. 5 min PBS incubation

During this sterilization protocol, it was found that increasing the interface position from 0.5 to 1 μm resulted in more structures surviving this procedure, as the 0.5 μm interface position (IP) did not have any structures left (see fig. A.19).

The newer protocol consisted of replacing PBS with demi-water, as demi-water has a lower surface energy because it contains no minerals, and this resulted in no structure detachment (see fig. A.20). The new protocol:

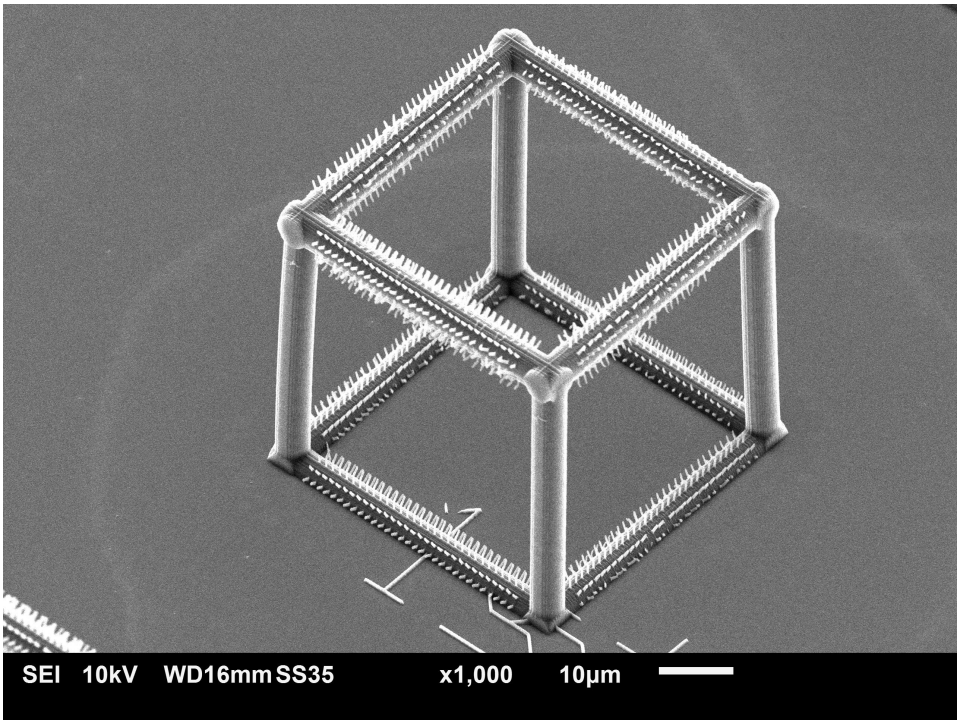

Figure A.18: SEM image of BC-NP showing non printed pillars on vertical beams due to shadowing.

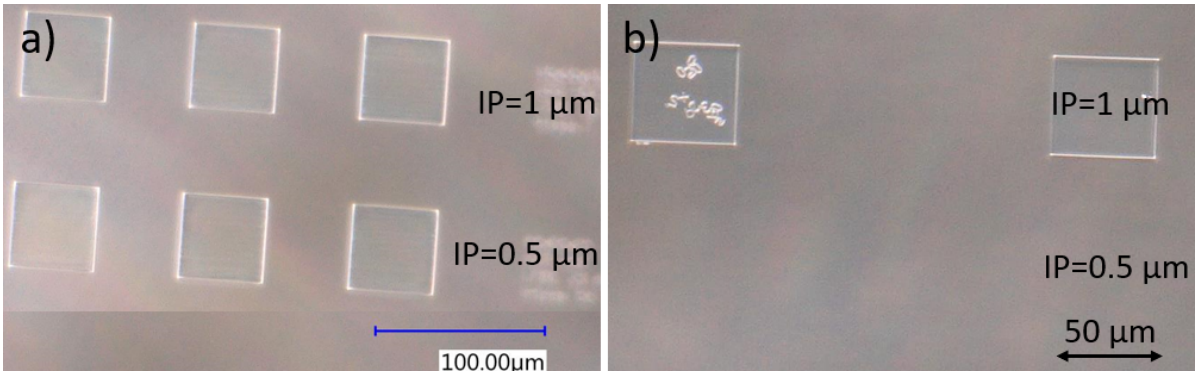

Figure A.19: Sterilization procedure: a) before sterilization, b) after PBS incubation.

1. 5 min ethanol 50% incubation
2. 5 min demi-water incubation
3. 5 min ethanol 70% incubation
4. 5 min demi-water incubation
5. 5 min ethanol 99.9% incubation
6. 5 min demi-water incubation

A.7. Cell fixation protocol using HMDS

Upon investigating the SEM pictures of cells cultured on micropillars, it was seen that some cells had ruptured membranes. This rupturing was due to stress forming in the cell membrane caused by the rapid shrinking of the cell membrane which was induced by the cell fixation protocol for SEM imaging. It was decided that a change in GA percentage or adding another fixating agent that causes less cell shrinkage, HMDS, would result in fewer cells with ruptured membranes. When looking at appendix A.7, it can be seen that 6 cases were investigated; No HMDS but 2 % PFA with 2 % GA, only 2 % GA, and only 4 % GA. And 2 % PFA with 2 % GA, only 2 % GA, and only 4 % GA but HMDS added as well. Using no PFA, 4% of GA and HMDS proved to be the best combination for the least amount of cell membrane rupture, but for consistency purposes, HMDS was used with 2% PFA and 2% GA.

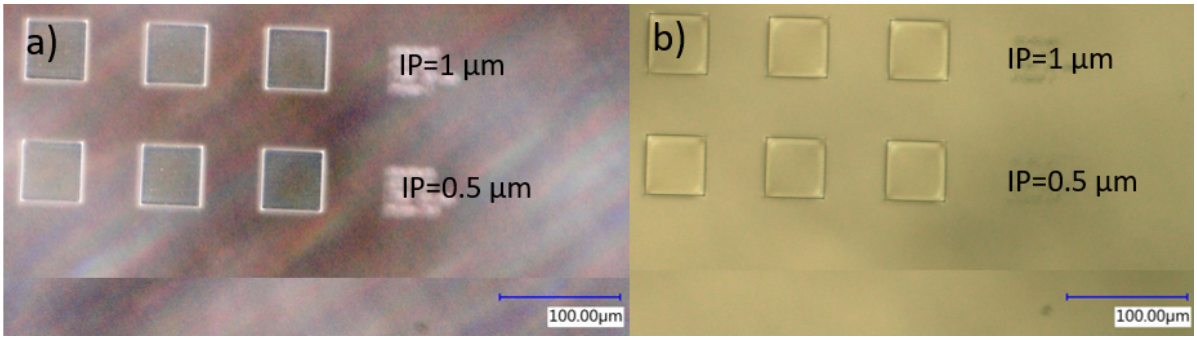

Figure A.20: Sterilization procedure: a) before sterilization, b) after demi-water incubation.

It can be seen from visual inspection that the combination of HMDS with 4 % GA resulted in less cell membrane rupture.

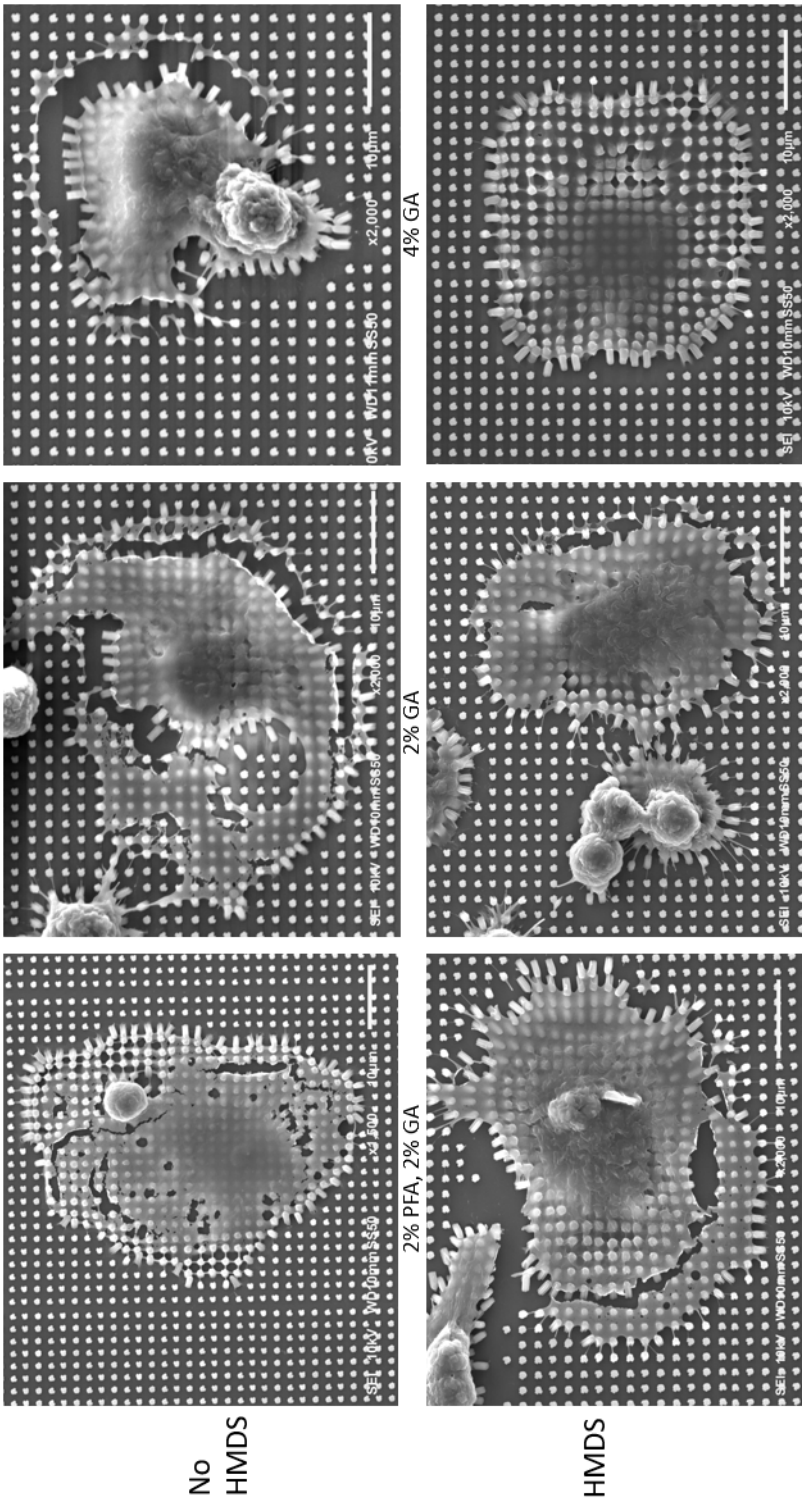

Figure A.21: SEM picture of THP-1 cells treated with different percentages of GA and treatment of HMDS. Top row no HMDS, bottom row HMDS applied

B

Cell data and graphs

B.1. Sholl analysis procedure

1. Open ImageJ and upload SEM or fluorescent image (if SEM image go to step 3, else continue) in which the cell membrane is visible within a grayscale image (for us the red channel) (fig. B.1a)
2. Go to image> adjust> brightness and contrast to increase the contrast of the picture
3. Measure scale bar in image in pixels and set scale for image Analyze> set scale (fig. B.1b)
4. Go to plugins> neuroanatonomy> SNT
5. Select image to trace and press ok
6. Draw the entire perimeter of the cell (fig. B.1c)
7. Click finish, go to path manager> click on path and then click analyze> skeletonize (fig. B.1d)
8. Go to LUT. invert LUT
9. Process> binary> fill holes
10. LUT> invert LUT
11. Process> binary > make binary
12. Select line tool and draw a line from the centre of cell towards the end of farthest process (fig. B.1e)
13. Go to plugins> neuroanatonomy> sholl> sholl from image
14. Set step size to 5 μm and click analyze (fig. B.1h)
15. Drawn concentric circles measure the intersections (fig. B.1f)
16. Sholl plot (fig. B.1g)
17. Save intersection data in excel file and now you can use that data for further processing

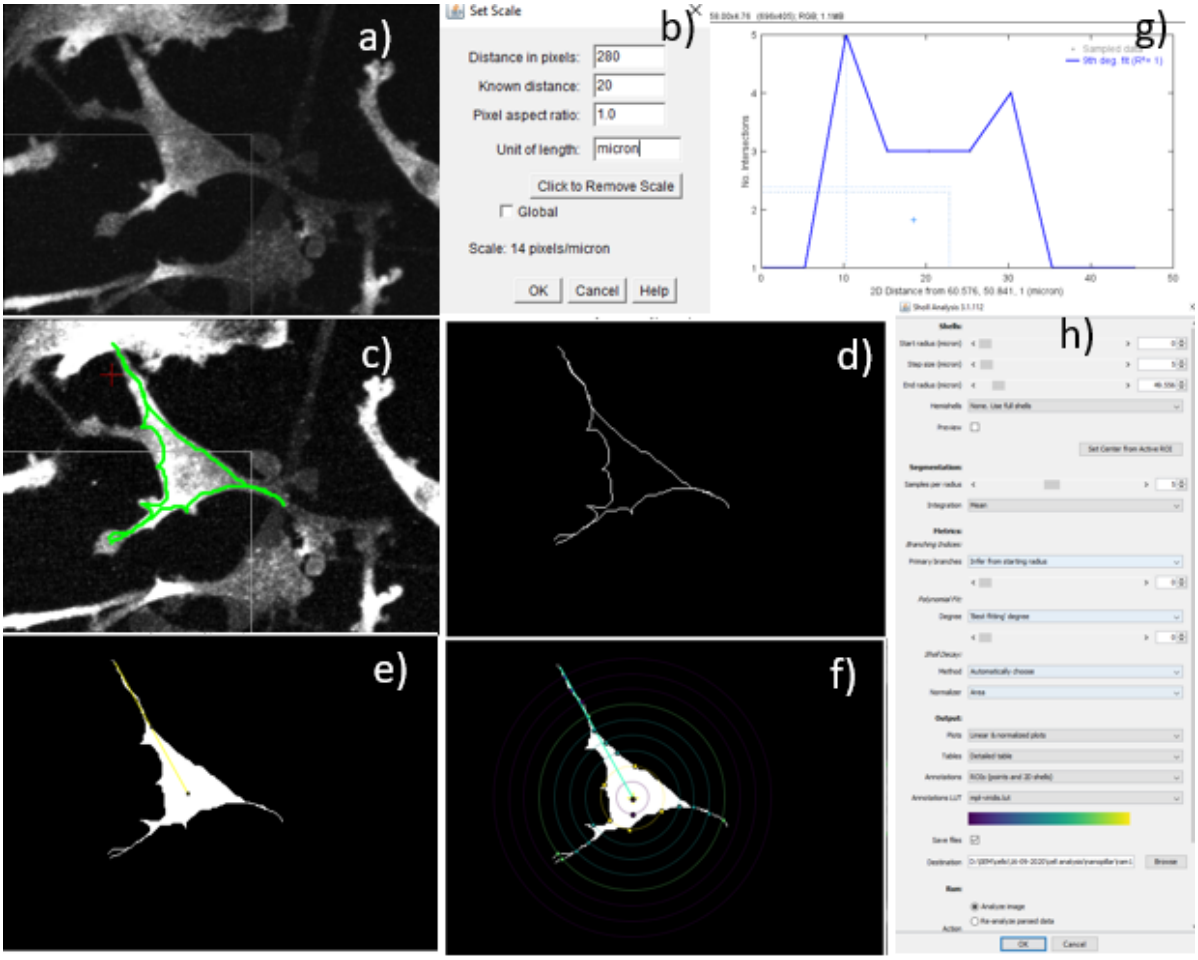

Figure B.1: Steps for Sholl analysis. a) select image to analyze, b) set scale, c) trace perimeter using SNT, d) rendered path, e) draw a line from the centre, f) drawn concentric circles, g) sholl plot, h) sholl analysis parameters.

B.2. Compression and pillar bending test data

Table B.1: Compression test pedestal 1: height = 20 μm, length = 130 μm, width = 130 μm, h = 200nm, s = 250 nm, lp = 85 %, ws=60 mm/s

Identifier	**Spring constant (kN/m)**	**Initial length (μm)**	**Tip area (μm^2)**	**Young's modulus (MPa)**
Measurement 1	130.63	20	2500	1.05
Measurement 2	179.75	20	2500	1.44
Measurement 3	153.27	20	2500	1.23
Measurement 4	175.22	20	2500	1.4
Average				**1.28**
Std. dev.				**0.18**

Table B.2: Compression test pedestal 2: height = 20 μm, length = 130 μm, width = 130 μm, h = 200 nm, s = 250 nm, lp = 70 %, ws = 30 mm/s

Identifier	**Spring constant (kN/m)**	**Initial length (μm)**	**Tip area (μm^2)**	**Young's modulus (MPa)**
Measurement 1	181.49	20	2500	1.45
Measurement 2	94.31	20	2500	0.75
Measurement 3	82.33	20	2500	0.66
Measurement 4	76.48	20	2500	0.61
Average				**0.87**
Std. dev.				**0.39**

Table B.3: Pillar bending test: Pillar height = 1.9 μm, pillar diameter = 390 μm, h = 200 nm, s = 250 nm, lp = 85 %, ws = 60 mm/s.

	k measured (N/m)	k cantilever (N//m)	kpillar (N/m)	E modulus (Gpa)
pillar 1	0.793	14.4	0.839	1.690
pillar 2	0.792	14.4	0.838	1.688
pillar 3	0.823	14.4	0.873	1.759
pillar 4	0.958	14.4	1.026	2.066
Average	0.841		0.894	1.801
st. dev.	0.079		0.089	0.180

B.3. Box plots

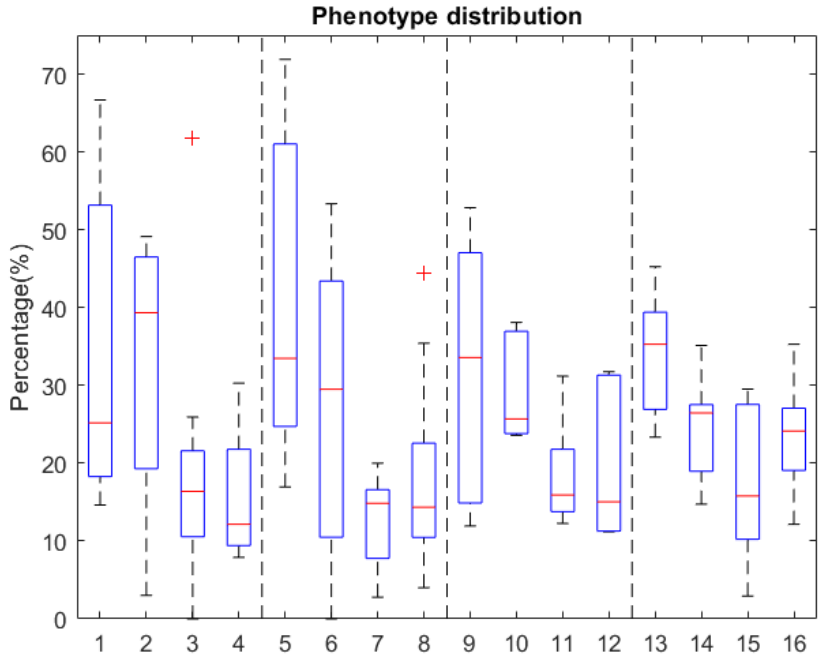

Figure B.2: Box plot of Phenotype distribution. 1-4 LS, 5-8 US, 9-12 LMP, 13-16 UMP. Box 1 of series: flat amoeboid, box 2 of series:bi-polar, box 3 of series: globular, box 4 of series: non-amoeboid. All donors used.

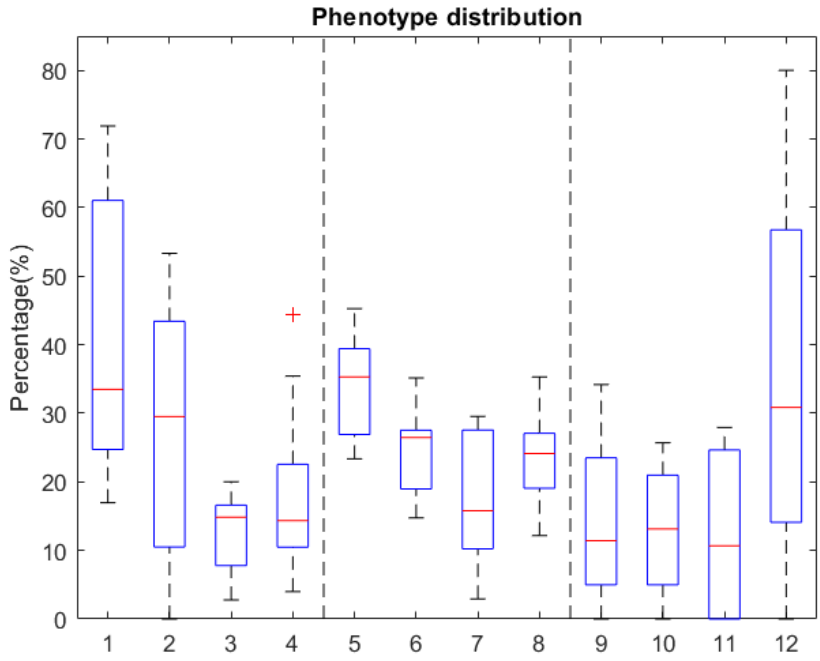

Figure B.3: Box plot of Phenotype distribution. 1-4 US, 5-8 UMP, 9-12 UNP. Box 1 of series: flat amoeboid, box 2 of series:bi-polar, box 3 of series: globular, box 4 of series: non-amoeboid. All donors used.

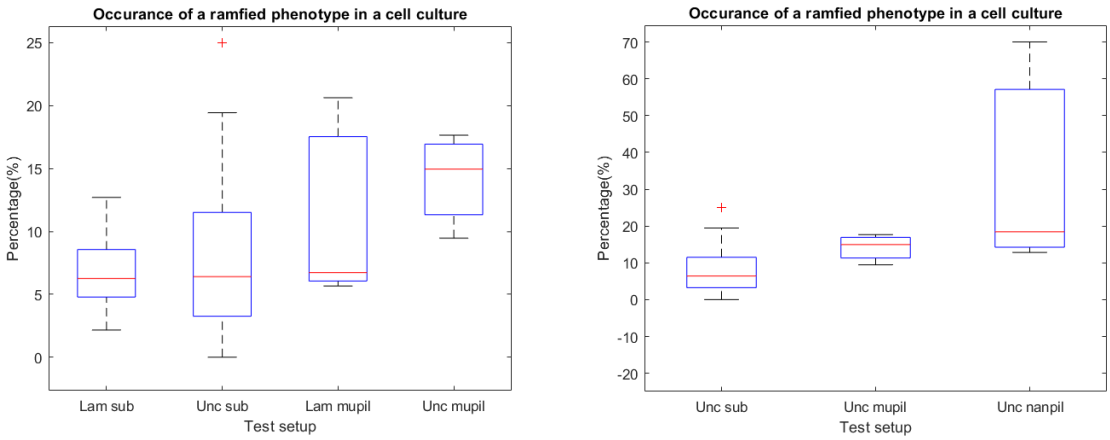

(a) **(b)**

Figure B.4: a) Ramified phenotype percentages fused silica substrate and micropillars, both uncoated and laminin-coated. All donors used. b) Ramified phenotype percentages for fused silica substrate, micropillars and nanopillars, all uncoated. All donors used.

B.4. The average number of cells per cage

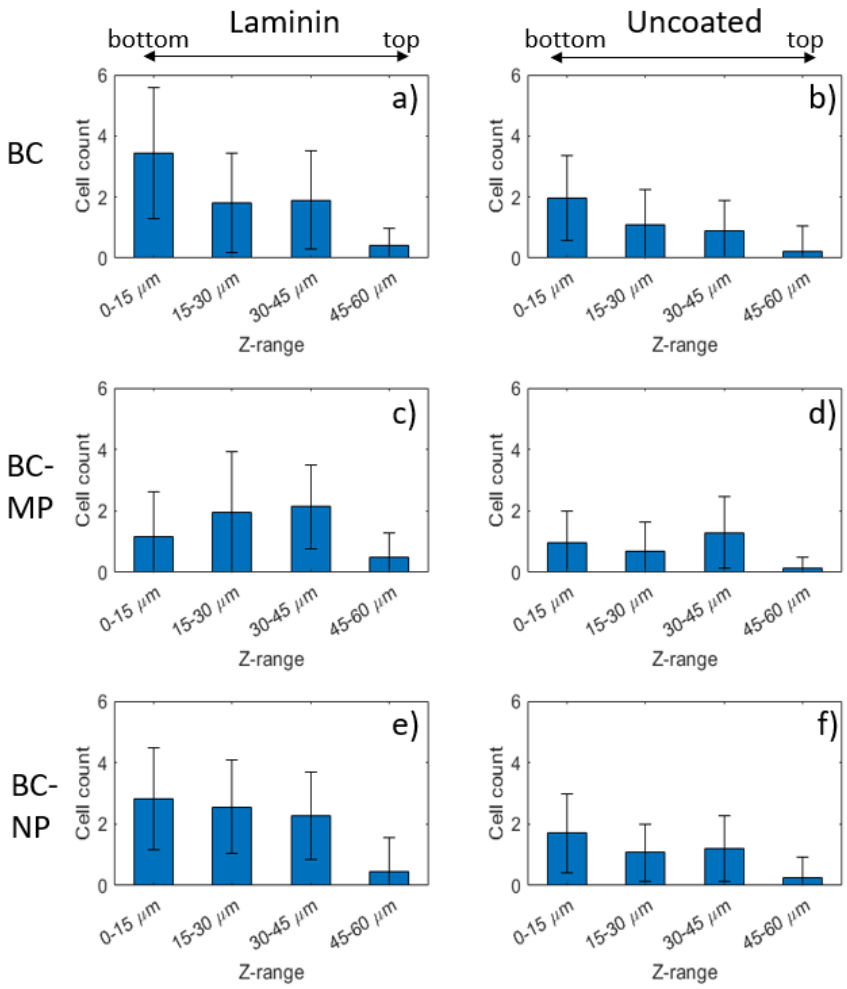

Figure B.5: The average number of cells per cage with respect to the z-range of the cage. Laminin-coated in the left column and uncoated in the right column. a and b BC, c and d BC-MP, e and f BC-NP. Donor R09153, with $N_{cage} > 25$ and $N_{cells} > 50$.

B.5. Cell data

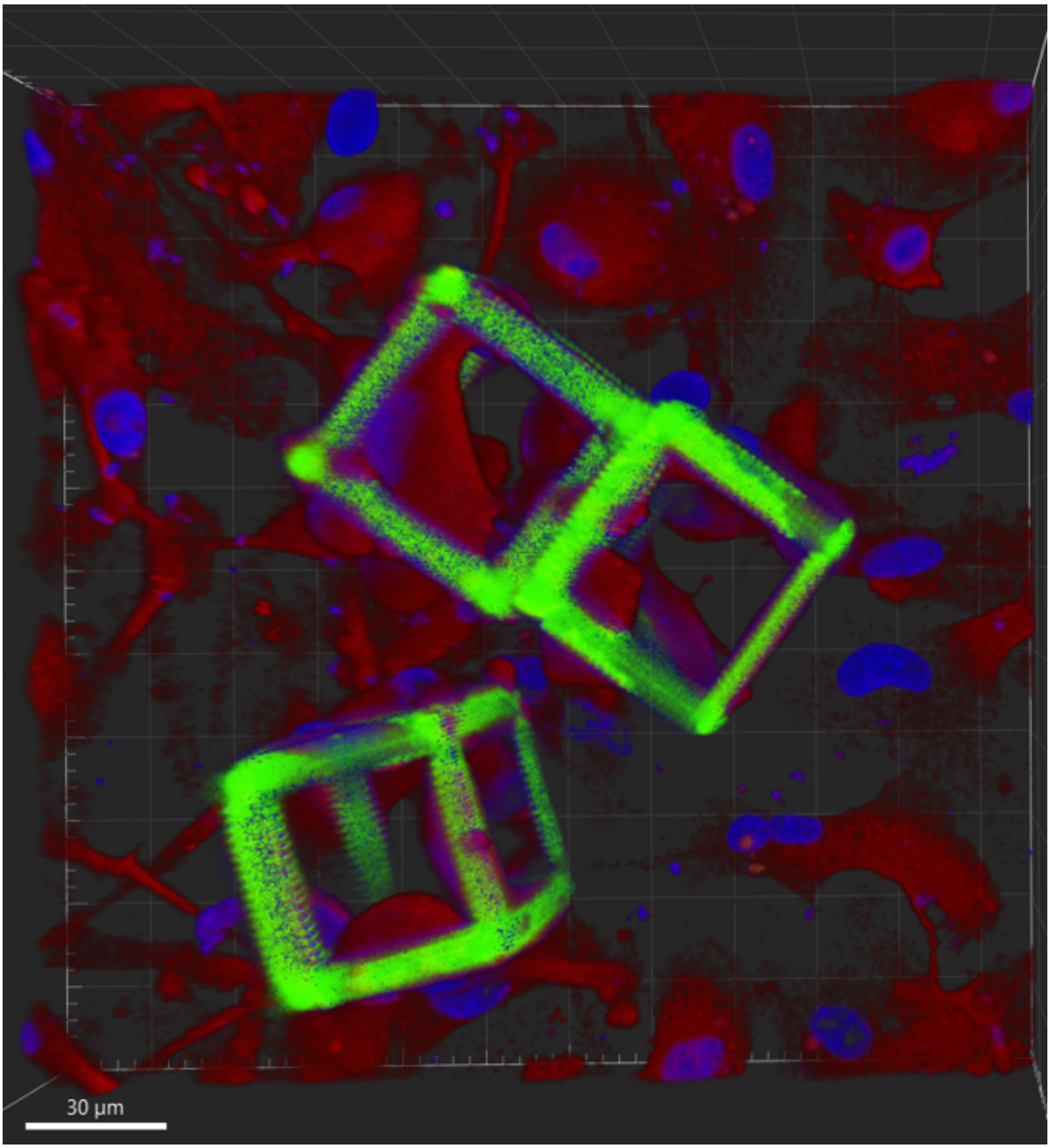

Figure B.6: Fluorescent image of a top view of BC-MP, enhanced in Imaris.

Table B.4: Lam sub: Cell count

	R07007		**R07110**			**R17045**	**R15059**		**R09153**
	sub1	sub 2	sub1	sub 2	sub 3	sub	1 sub	lam2 sub	1 sub
Flat amoeboid	40	37	35	30	13	22	35	48	12
Bipolar	16	22	65	52	10	1	94	114	26
Globular	9	4	28	21	50	0	62	38	8
Non amoeboid	9	7	11	9	8	10	48	32	17
Total	**74**	**70**	**139**	**112**	**81**	**33**	**239**	**232**	**63**
Ramified	4	3	10	7	4	3	20	5	8

Table B.5: Lam sub: Number of primary branches

		Number of primary branches				
		ram 1	ram 2	ram 3	ram 4	ram 5
R07007	lam sub1	5	5	4	5	-
	lam sub2	4	4	5	-	-
R07110	lam sub1	4	4	4	4	7
	lam sub2	10	4	4	4	4
	lam sub3	3	5	4	3	3
R17045	lam sub	7	4	3	3	-
R15059	lam 1 sub	3	3	3	4	5
	lam2 sub	3	3	4	4	4
R09153	lam 1 sub	4	7	3	6	7

Table B.6: Lam sub: Area under curve

		Area under the curve				
		ram 1	ram 2	ram 3	ram 4	ram 5
R07007	sub1	155	305	135	285	-
	sub2	190	175	275	-	-
R07110	sub1	280	305	175	280	550
	sub2	730	215	255	465	390
	sub3	295	230	335	235	290
R17045	sub	205	685	410	225	-
R15059	1 sub	195	205	200	235	195
	lam2 sub	140	115	145	235	115
R09153	1 sub	175	535	120	380	425

Table B.7: Unc sub: Cell count

	R07007		**R07110**			**R01068**		**R17045**	**R15059**		**R09153**	
	sub 1	sub2	sub 1	sub2	sub3	sub SEM	sub	sub	1 sub	2 sub	1 sub	2 sub
Flat amoeboid	52	26	72	21	17	28	38	23	55	39	9	9
Bipolar	88	18	12	0	3	20	57	3	111	116	10	15
Globular	13	4	21	5	2	13	23	2	40	46	1	7
Non amoeboid	12	2	22	4	4	18	34	4	19	29	16	17
Total	**165**	**50**	**127**	**30**	**26**	**79**	**152**	**32**	**225**	**230**	**36**	**48**
Ramified	8	0	10	0	1	6	16	4	6	12	7	12

Table B.8: Unc sub: Area under the curve

		Area under the curve				
		ram 1	ram 2	ram 3	ram 4	ram 5
R07007	sub 1	165	230	200	225	-
	sub 2	-	-	-	-	-
R07110	sub 1	-	-	-	-	-
	sub 2	-	-	-	-	-
	sub 3	215	205	180	400	455
R01068	sub	520	285	380	265	230
R17045	sub	460	525	-	-	-
R15059	1 sub	150	215	280	285	150
	2 sub	270	460	120	320	275
R09153	1 sub	370	320	260	340	665
	2 sub	325	390	420	200	245

Table B.9: Unc sub: Number of primary branches

		Number of primary branches				
		ram 1	ram 2	ram 3	ram 4	ram 5
R07007	sub 1	3	4	3	3	-
	sub 2	-	-	-	-	-
R07110	sub 1	-	-	-	-	-
	sub 2		-	-	-	-
	sub 3	5	3	4	3	11
R01068	sub	6	4	4	5	4
R17045	sub	8	13	-	-	-
R15059	1 sub	3	3	6	4	4
	2 sub	3	7	4	4	3
R09153	1 sub	5	6	4	4	7
	2 sub	4	3	8	4	3

Table B.10: Lam mup: Cell count

	R15059			**R09153**	
	mupil 1	mupil 2	mupil 1 SEM	mupil 1	mupil 2
Flat amoeboid	45	56	51	13	10
Bipolar	49	25	27	28	24
Globular	25	13	18	34	9
Non amoeboid	15	12	17	34	20
Total	**134**	**106**	**113**	**109**	**63**
Ramified	9	6	7	18	13

Table B.11: Lam mup: Number of primary branches

		Number of primary branches				
		ram 1	ram 2	ram 3	ram 4	ram 5
R15059	lam mupil	4	6	7	5	-
	lam mupil2	4	4	6	5	4
R09153	lam mupil	10	6	5	7	6
	lam mupil2	5	6	8	6	6

Table B.12: Lam mup: Area under the curve

		Area under the curve				
		ram 1	ram 2	ram 3	ram 4	ram 5
R15059	lam mupil	205	145	465	145	-
	lam mupil2	160	100	180	245	215
R09153	lam mupil	305	200	215	285	395
	lam mupil2	295	445	435	710	355

Table B.13: Unc mup: Cell count

	R01068		**R15059**			**R09153**	
	mupill sem	mupill1	mupill1	mupill1 SEM	mupill2	mupill1	mupill2
Flat amoeboid	63	25	41	43	37	23	12
Bipolar	35	23	29	14	52	16	9
Globular	57	29	16	15	41	5	1
Non amoeboid	38	30	20	23	18	14	12
Total	**193**	**107**	**106**	**95**	**148**	**58**	**34**
Ramified	21	16	17	12	14	10	6

Table B.14: Unc mup: Number of primary branches

		Number of primary branches				
		ram 1	ram 2	ram 3	ram 4	ram 5
R01068	unc mupil	8	6	6	6	7
R15059	unc mupil	7	7	8	8	10
	unc mupil2	9	4	5	5	4
R09153	unc mupil	4	5	4	6	8
	unc mupil2	7	6	3	4	4

Table B.15: Unc mup: Area under the curve

		Area under the curve				
		ram 1	ram 2	ram 3	ram 4	ram 5
R01068	unc mupil	345	480	405	410	385
R15059	unc mupil	225	230	190	340	265
	unc mupil2	295	225	135	325	270
R09153	unc mupil	200	365	330	250	380
	unc mupil2	545	590	360	195	185

Table B.16: Unc nanp: Cell count

	R01068		**R09153**
	nanpil SEM	nanopil1	nanopil sem
Flat amoeboid	23	40	2
Bipolar	46	19	2
Globular	50	25	0
Non amoeboid	60	33	16
Total	**179**	**117**	**20**
Ramified	33	15	14

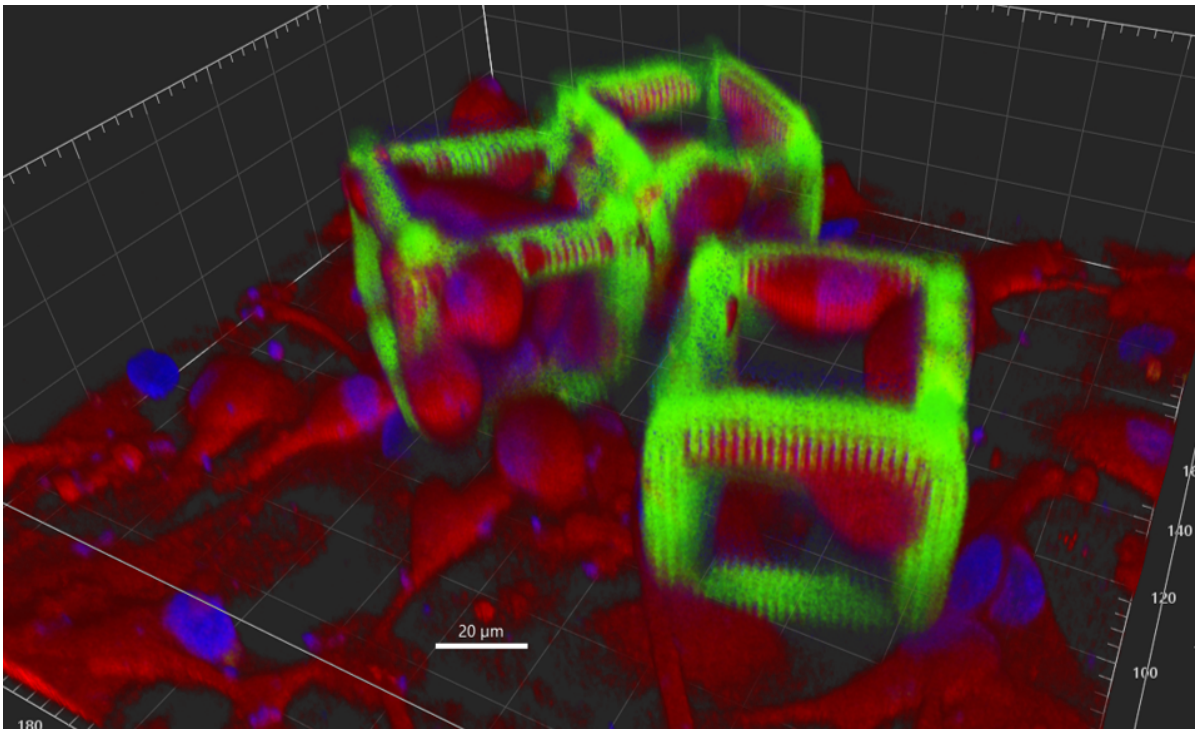

Figure B.7: Fluorescent image of an isometric view of BC-MP, enhanced in Imaris.

Table B.17: Unc nanp: Number of primary branches

		Number of primary branches				
		ram 1	ram 2	ram 3	ram 4	ram 5
R01068	unc nanpil sem	7	6	8	7	-
	unc nanpil	6	6	4	5	-
R09153	unc nanpil sem	7	7	6	6	7

Table B.18: Unc nanp: Area under the curve

		Area under the curve				
		ram 1	ram 2	ram 3	ram 4	ram 5
R01068	unc nanpil sem	300	420	430	330	-
	unc nanpil	470	370	475	660	-
R09153	unc nanpil sem	440	590	295	320	275

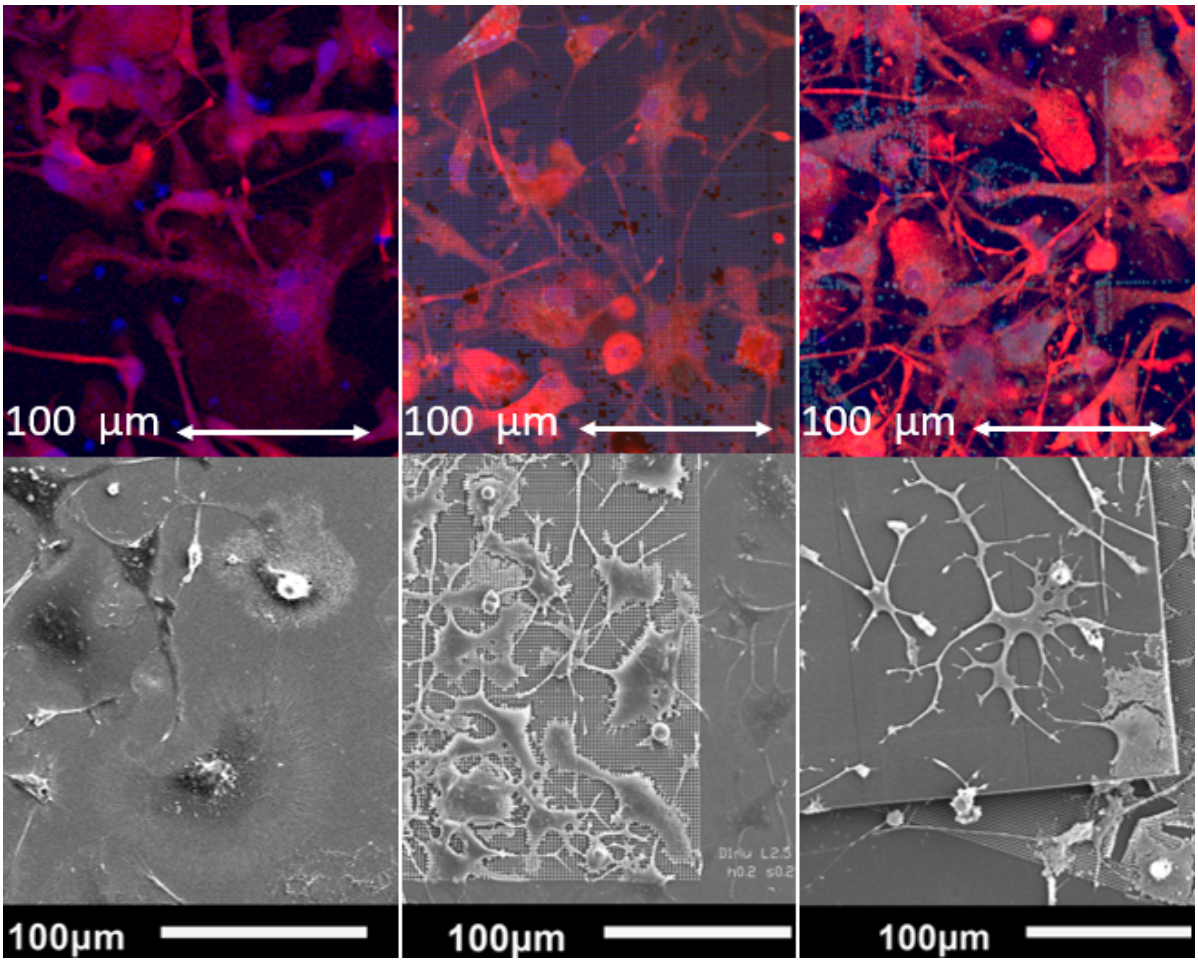

Figure B.8: SEM and Fluorescent image showing (from left to right) microglia on pedestal, MP and NP.

B.6. Initial time planning

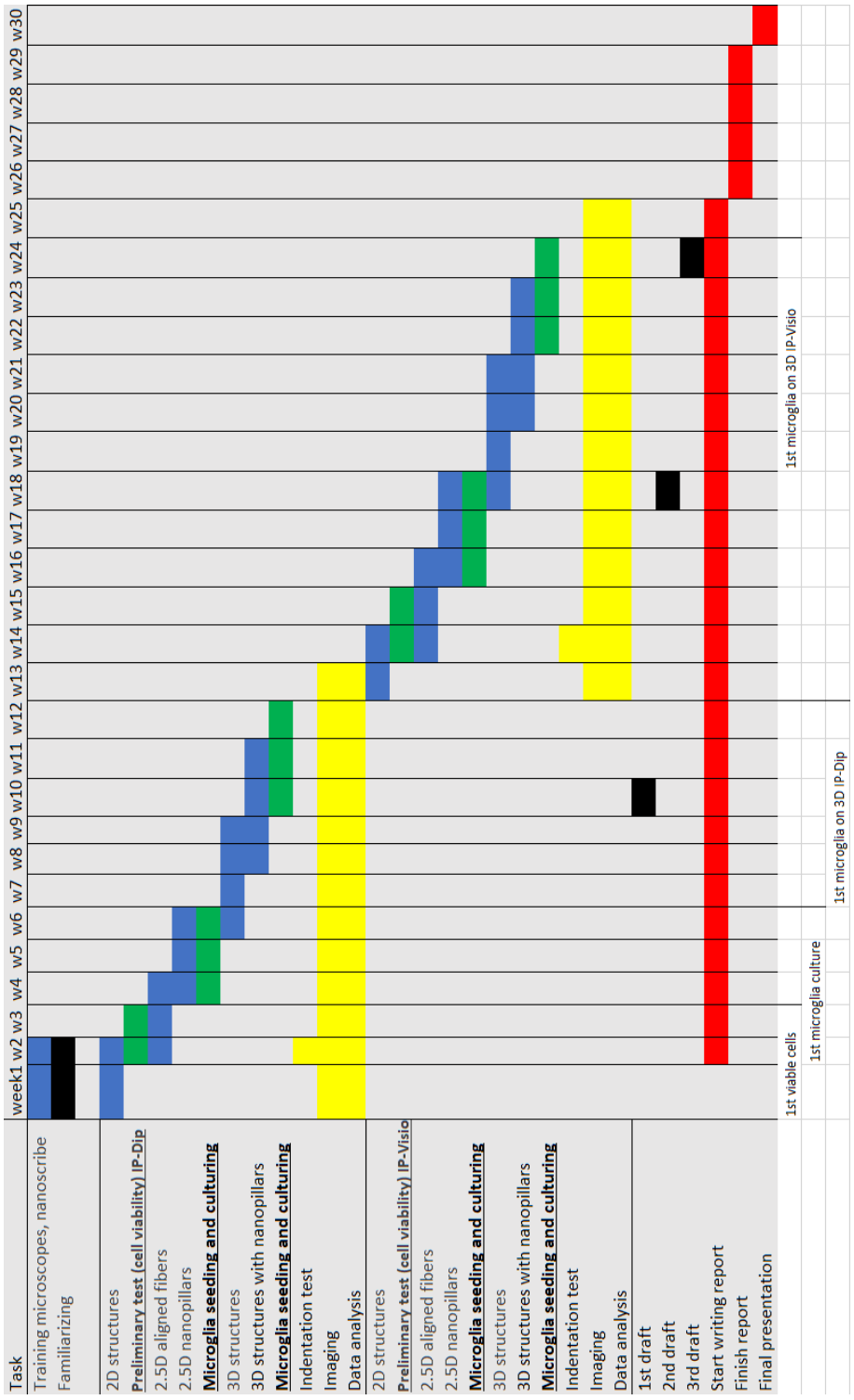

Figure B.9: Initial time planning for 30 weeks (start in July, ending in February). The colours stand for: black = Familiarization with equipment and report drafts, blue = Fabrication of structures, yellow = Imaging, material characterization and data analysis, green = cell culturing, red = report writing, finishing and presentation practising. Underneath the chart are the to be achieved milestones.

Bibliography

[1] L. Guzman-Martinez et al. “Neuroinflammation as a common feature of neurodegenerative disorders”. In: Frontiers in Pharmacology 10.1008 (2019), pp. 1–17. ISSN: 16639812. DOI: 10.3389/fphar.2019.01008.

[2] B. Delatour et al. “In vivo imaging biomarkers in mouse models of Alzheimer’s disease: Are we lost in translation or breaking through?” In: International Journal of Alzheimer’s Disease 2010 (2010), p. 11. ISSN: 20900252. DOI: 10.4061/2010/604853.

[3] M. Vitek et al. “Translational animal models for Alzheimer’s disease: An Alzheimer’s Association Business Consortium Think Tank”. In: Alzheimer’s Dementia: Translational Research Clinical Interventions 6.1 (2020), pp. 1–12. ISSN: 2352-8737. DOI: 10.1002/trc2.12114.

[4] G. Stonebarger et al. “The Rhesus Macaque as a Translational Model for Neurodegeneration and Alzheimer’s Disease”. In: Frontiers in Aging Neuroscience 13.September (2021), pp. 1–8. ISSN: 16634365. DOI: 10.3389/fnagi.2021.734173.

[5] D. Gosselin et al. “An environment-dependent transcriptional network specifies human microglia identity”. In: Physiology behavior 176.5 (2017), pp. 139–148. ISSN: 16634365. DOI: 10.1126/science.aal3222.An.

[6] H. Könnecke et al. “The Role ofMicroglia and Matrix Metalloproteinases Involvement in Neuroinflammation and Gliomas”. In: Clinical and Developmental Immunology 2013 (2013), p. 15. ISSN: 17402522. DOI: 10.1155/2013/914104. URL: http://dx.doi.org/10.1155/2013/914104.

[7] Y. Kim et al. “Nano-Architectural Approaches for Improved Intracortical Interface Technologies”. In: Frontiers in Neuroscience 12.July (2018). DOI: 10.3389/fnins.2018.00456.

[8] The Nervous System. June 2020. URL: https://courses.lumenlearning.com/wm-biology2/chapter/glial-cells/.

[9] D. Liewald et al. “Distribution of axon diameters in cortical white matter: an electron-microscopic study on three human brains and a macaque”. In: Biological Cybernetics 108.5 (2014), pp. 541–557. ISSN: 14320770. DOI: 10.1007/s00422-014-0626-2.

[10] “The principles of nerve cell communication”. In: Alcohol health and research world 21.2 (1997), pp. 107–108. ISSN: 0090838X.

[11] R. Cronin et al. “Stratification of astrocytes in healthy and diseased brain”. In: Brain Pathology 176.3 (2017), pp. 139–148. ISSN: 3902264330. DOI: 10.1016/j.physbeh.2017.03.040.

[12] A. Verkhratsky et al. “Physiology of astroglia”. In: Physiological Reviews 98.1 (2018), pp. 239–389. DOI: 10.1152/physrev.00042.2016.

[13] J. Zuchero et al. “Intrinsic and extrinsic control of oligodendrocyte development Origin and OPC specification”. In: Current Opinions Neurobiology 23.6 (2013), pp. 914–920. DOI: 10.1016/j.conb.2013.06.005.

[14] A. Jiménez et al. “Structure and function of the ependymal barrier and diseases associated with ependyma disruption”. In: Tissue Barriers 2.3 (2014), pp. 1–14. ISSN: 21688370. DOI: 10.4161/tisb.28426.

[15] K. Saijo et al. “Microglial cell origin and phenotypes in health and disease”. In: Nature Reviews Immunology 11.11 (2011), pp. 775–787. ISSN: 14741733. DOI: 10.1038/nri3086.

[16] S. Hickman et al. “Microglia in neurodegeneration”. In: Nature Neuroscience 21.10 (2018), pp. 1359–1369. ISSN: 15461726. DOI: 10.1038/s41593-018-0242-x.

[17] E. Shobin et al. “Microglia activation and phagocytosis: relationship with aging and cognitive impairment in the rhesus monkey”. In: GeroScience 39.2 (2017), pp. 199–220. DOI: 10.1007/s11357-017-9965-y.

[18] H. Jeong et al. “Brain Inflammation and Microglia: Facts and Misconceptions”. In: Experimental Neurobiology 22.2 (2013), pp. 59–67. DOI: 10.5607/en.2013.22.2.59.

[19] Torres-Platas et al. “Morphometric characterization of microglial phenotypes in human cerebral cortex”. In: Journal of Neuroinflammation 11.12 (2014). ISSN: 17422094. DOI: 10.1186/1742-2094-11-12.

[20] Fused silica. June 2020. URL: https://www.accuratus.com/fused.html.

[21] Silica-Fused Silica. June 2020. URL: https://www.azom.com/properties.aspx?ArticleID=1387.
[22] Silicon Dioxide. June 2020. URL: https://www.memsnet.org/material/silicondioxidesio2film/.
[23] S. Budday et al. “Mechanical properties of gray and white matter brain tissue by indentation”. In: Journal of the Mechanical Behavior of Biomedical Materials 46 (2015), pp. 318–330. ISSN: 18780180. DOI: http://dx.doi.org/10.1016/j.jmbbm.2015.02.024.
[24] S. Budday et al. “Mechanical characterization of human brain tissue”. In: Acta Biomaterialia 48 (2017), pp. 319–340. ISSN: 18787568. DOI: 10.1016/j.actbio.2016.10.036.
[25] C. Tomba. “Primary brain cells in in vitro controlled microenvironments: single cell behaviors for collective functions”. In: Acta Biomaterialia (2014). URL: https://tel.archives-ouvertes.fr/tel-01127126.
[26] I. S. Palamà et al. “Nanomaterials for regenerative medicine: Chapter 22: MECHANICAL GUIDANCE OF CELL MIGRATION”. In: NANOMEDICINE 6.1 (2010), pp. 565–578. URL: https://doi.org/10.2217/nnm.10.146.
[27] M. Dubbelaar et al. “The Kaleidoscope of Microglial Phenotypes”. In: Frontiers in Immunology 9.July (2018). DOI: 10.3389/fimmu.2018.01753.
[28] Y. Chen et al. “Receptor-mediated cell mechanosensing”. In: Molecular Biology of the Cell 28.23 (2017), pp. 3134–3155. DOI: 10.1091/mbc.E17-04-0228.
[29] G. Choi. “Importance of Microglial Cytoskeleton and the Actin-interacting Proteins in Alzheimer’s Disease”. In: Biomedical Science Letters 26.1 (2020). DOI: 10.15616/bsl.2020.26.1.1.
[30] J. Small et al. “The lamellipodium: Where motility begins”. In: Trends in Cell Biology 12.3 (2002), pp. 112–120. DOI: 10.1016/S0962-8924(01)02237-1.
[31] Q. Zhao et al. “The mechanosensitive Piezo1 channel: a three-bladed propeller-like structure and a lever-like mechanogating mechanism”. In: FEBS Journal 286 (2019), pp. 2461–2470. DOI: 10.1111/febs.14711.
[32] A. Theocharis et al. “Extracellular matrix structure”. In: Advanced Drug Delivery Reviews 97 (2016), pp. 4–27. ISSN: 18728294. DOI: 10.1016/j.addr.2015.11.001. URL: http://dx.doi.org/10.1016/j.addr.2015.11.001.
[33] A. Katsumi et al. “Integrins in Mechanotransduction”. In: Journal of Biological Chemistry 279.13 (2004), pp. 12001–12004. DOI: 10.1074/jbc.R300038200.
[34] M. J. P. Biggs et al. “Nanotopographical modification: A regulator of cellular function through focal adhesions.” In: Bone 23.1 (2008), pp. 1–7. DOI: 10.1038/jid.2014.371.
[35] L. Pieres et al. “The role of the surface on microglia function : implications for central nervous system tissue engineering”. In: Interface 12.24 (2015). DOI: 10.1098/rsif.2014.1224. URL: http://dx.doi.org/10.1098/rsif.2014.1224.
[36] V. Perry. “Microglia and macrophages of the central nervous system: The contribution of microglia priming and systemic inflammation to chronic neurodegeneration”. In: Seminars in Immunopathology 35.5 (2013), pp. 601–612. DOI: 10.1007/s00281-013-0382-8.
[37] E. Saino et al. “Effect of electrospun fiber diameter and alignment on macrophage activation and secretion of proinflammatory cytokines and chemokines”. In: Biomacromolecules 12.5 (2011), pp. 1900–1911. ISSN: 15257797. DOI: 10.1021/bm200248h.
[38] S. Persheyev et al. “BV-2 microglial cells sense micro-nanotextured silicon surface topology”. In: BIOMEDICAL MATERIALS RESEARCH 99A.1 (2011), pp. 135–140. DOI: 10.1002/jbm.a.33159.
[39] C. Rasmussen et al. “Enhanced Differentiation of Human Embryonic Stem Cells Toward Definitive Endoderm on Ultrahigh Aspect Ratio Nanopillars”. In: Advanced Functional Materials 26.6 (2016), pp. 815–823. DOI: 10.1002/adfm.201504204.
[40] T. Luu et al. “Micro- and Nanopatterned Topographical Cues for Regulating Macrophage Cell Shape and Phenotype”. In: ACS Applied Materials and Interfaces 7.51 (2015). ISSN: 19448252. DOI: 10.1021/acsami.5b10589.
[41] A. Miri et al. “Multiscale Bioprinting of Vascularized Models”. In: Biomaterials 198 (2019), pp. 204–216. DOI: 10.1016/j.biomaterials.2018.08.006..
[42] Electrospinning. June 2020. URL: https://www.nanoscience.com/techniques/electrospin/.
[43] Schematic representation of the multiphoton writing process. July 2021. URL: https://en.wikipedia.org/wiki/Multiphoton_lithography.
[44] D. Tamay et al. “3D and 4D printing of polymers for tissue engineering applications”. In: Frontiers in Bioengineering and Biotechnology 7.July (2019). ISSN: 22964185. DOI: 10.3389/fbioe.2019.00164.

[45] B. Bushan et al. “An overview of additive manufacturing (3D printing) for microfabrication”. In: Microsystem Technologies 23.4 (2017), pp. 1117–1124. ISSN: 0946707. DOI: 10.1007/s00542-017-3342-8.

[46] I. Rana Khalid et al. “3D Bioprinting: An attractive alternative to traditional organ transplantation”. In: Archive of Biomedical Science and Engineering 5.1 (2019), pp. 1117–1124. DOI: 10.17352/abse.000012.

[47] G. Gillispie et al. “Assessment methodologies for extrusion-based bioink printability”. In: Biofabrication 12.2 (2020). ISSN: 17585090. DOI: 10.1088/1758-5090/ab6f0d.

[48] M. Waqas Munir et al. “Classification of Electrospinning Methods”. In: Nanorods and Nanocomposites (2020). DOI: 10.5772/intechopen.88654.

[49] P. Dalton et al. “Electrospinning and additive manufacturing: Converging technologies”. In: Biomaterials Science 1.2 (2013), pp. 171–185. ISSN: 20474830. DOI: 10.1039/c2bm00039c.

[50] D. Fan. ME46025: Manufacturing for the micro and nano scale, Lecture 2, Two photon polymerization. Apr. 2019.

[51] Nanoscribe Photonic Professional GT2 specifications. May 2020. URL: https://www.nanoscribe.com/en/solutions/photonic-professional-gt2#tab-385.

[52] K. Worthington et al. “Two-photon polymerization for production of human iPSC-derived retinal cell grafts”. In: Acta Biomaterialia 55.June (2017), pp. 385–395. DOI: 10.1016/j.actbio.2017.03.039.

[53] X. Zhou et al. “A review on the processing accuracy of two-photon polymerization”. In: AIP Advances 5.3 (2015). DOI: 10.1063/1.4916886.

[54] IP-Dip. June 2020. URL: https://support.nanoscribe.com/hc/en-gb/articles/360001748953-IP-Dip.

[55] E. Lemma et al. “Mechanical Properties Tunability of Three-Dimensional Polymeric Structures in Two-Photon Lithography”. In: IEEE Transactions on Nanotechnology 16.1 (2017), pp. 23–31. DOI: 10.1109/TNANO.2016.2625820.

[56] M. Olsen et al. “In-chip fabrication of free-form 3D constructs for directed cell migration analysis”. In: Lab on a Chip 13.24 (2013), pp. 4800–4809. DOI: 10.1039/c3lc50930c.

[57] IP-L 780. June 2020. URL: https://support.nanoscribe.com/hc/en-gb/articles/360001755654-IP-L-780.

[58] M. Nouri-Goushki et al. “Submicron Patterns-on-a-Chip: Fabrication of a Microfluidic Device Incorporating 3D Printed Surface Ornaments”. In: ACS Biomaterials Science and Engineering 5.11 (2019), pp. 6127–6136. DOI: 10.1021/acsbiomaterials.9b01155.

[59] IP-S. June 2020. URL: https://support.nanoscribe.com/hc/en-gb/articles/360001750353-IP-S.

[60] Y. Liu et al. “Deformation behavior of foam laser targets fabricated by two-photon polymerization”. In: Nanomaterials 8.7 (2018), pp. 1–20. DOI: 10.3390/nano8070498.

[61] R. Kramer et al. “Multiscale 3D-printing of microfluidic AFM cantilevers”. In: Lab on a Chip 20.2 (2020), pp. 311–319. DOI: 10.1039/c9lc00668k.

[62] M. Schmid et al. “Optical properties of photoresists for femtosecond 3D printing: refractive index, extinction, luminescence-dose dependence, aging, heat treatment and comparison between 1-photon and 2-photon exposure”. In: Optical Materials Express 9.12 (2019). DOI: 10.1364/ome.9.004564.

[63] Q. Akolowala et al. “3D Engineered Glioblastoma Microenvironments for Proton Beam Irradiation”. In: (2021).

[64] A. Ongaro et al. “Polylactic acid, a sustainable, biocompatible, transparent substrate material for Organ-On-Chip, and Microfluidic applications”. In: bioRxiv (2019). DOI: 10.1101/647347.

[65] SD3D. “PLA Technical data sheet”. In: 41 (2014), pp. 2–3. URL: https://www.sd3d.com/wp-content/uploads/2017/06/MaterialTDS-PLA_01.pdf.

[66] S. Farah et al. “Physical and mechanical properties of PLA, and their functions in widespread applications — A comprehensive review”. In: Advanced Drug Delivery Reviews 107 (2016), pp. 367–392. DOI: 10.1016/j.addr.2016.06.012.

[67] K. Ragaert et al. “Bulk Mechanical Porperties of Thermoplastic Poly- e- caprolacton”. In: 6e Polymers & Molds Innovations Conference (2014). URL: 270509196_Bulk_Mechanical_Porperties_of_Thermoplastic_PCL.

[68] T. Vandamme et al. “Physico-mechanical properties of poly(-caprolactone) for the construction of rumino-reticulum devices for grazing animals”. In: Biomaterials 16.18 (1995), pp. 1395–1400. DOI: 10.1016/0142-9612(95)96875-Z.

[69] S. Huang et al. “Highly Fluorescent Polycaprolactones with Tunable Light Emission Wavelengths across Visible to NIR Spectral Window”. In: Advanced Materials Interfaces 3.17 (2016), pp. 1–6. DOI: 10.1002/admi.201600259.

[70] M. Broz et al. “Structure and mechanical properties of poly(D,L-lactic acid)/poly(-caprolactone) blends”. In: Biomaterials 24.23 (2003), pp. 4181–4190. DOI: 10.1016/S0142-9612(03)00314-4.

[71] R. Haq et al. “Characterization and Mechanical Analysis of PCL/PLA composites for FDM feedstock filament”. In: Materials Science and Engineering 226.1 (2017). DOI: 10.1088/1757-899X/226/1/012038.

[72] J. Maitra et al. “Cross-linking in Hydrogels - A Review”. In: American Journal of Polymer Science 4.2 (2014), pp. 25–31. DOI: 10.5923/j.ajps.20140402.01.

[73] R. Wong et al. “Effect of crosslinking agent concentration on the properties of unmedicated hydrogels”. In: Pharmaceutics 7.3 (2015), pp. 305–319. ISSN: 19994923. DOI: 10.3390/pharmaceutics7030305.

[74] G. Hoti et al. “Effect of the Cross-Linking Density on the Swelling and Rheological Behavior of Ester-Bridged -Cyclodextrin Nanosponges”. In: Materials 14.3 (2021), pp. 1–20. ISSN: 19961944. DOI: 10.3390/ma14030478.

[75] A. Accardo et al. “Two-photon lithography and microscopy of 3D hydrogel scaffolds for neuronal cell growth”. In: Biomedical Physics and Engineering Express 4 (2018). ISSN: 20571976. DOI: 10.1088/2057-1976/aaab93.

[76] S. Gäbler et al. “Determination of the viscoelastic properties of hydrogels based on polyethylene glycol diacrylate (PEG-DA) and human articular cartilage”. In: International Journal of Materials Engineering Innovation 1.1 (2009), pp. 3–20. DOI: 10.1504/IJMATEI.2009.024024.

[77] D. Wei et al. “A biocompatible hydrogel with improved stiffness and hydrophilicity for modular tissue engineering assembly”. In: Journal of Materials Chemistry 3.14 (2015). DOI: 10.1039/c5tb00129c.

[78] M. Zhu et al. “Gelatin methacryloyl and its hydrogels with an exceptional degree of controllability and batch-to-batch consistency”. In: Scientific Reports 9.1 (2019). DOI: 10.1038/s41598-019-42186-x.

[79] A. Accardo et al. “Multiphoton Direct Laser Writing and 3D Imaging of Polymeric Freestanding Architectures for Cell Colonization”. In: Small 13.27 (2017). ISSN: 16136829. DOI: 10.1002/smll.201700621.

[80] S. Pucev et al. “3D-microfabrication by two-photon polymerization of an integrated sacrificial stencil mask”. In: Micro and Nano Engineering 2.october (2019), pp. 70–75. DOI: 10.1016/j.mne.2019.01.004.

[81] I. Pepelanova et al. “Gelatin-methacryloyl (GelMA) hydrogels with defined degree of functionalization as a versatile toolkit for 3D cell culture and extrusion bioprinting”. In: Bioengineering 5.3 (2018), pp. 3–20. DOI: 10.3390/bioengineering5030055.

[82] MaxGel™ ECM Hydrogel: An In Vitro Human Cell Derived Basement Membrane Extract for 3D Cell Culture Applications. June 2020. URL: https://www.sigmaaldrich.com/life-science/stem-cell-biology/3d-stem-cell-culture/maxgel-human-ecm.html.

[83] C. Hoeve. “The structure of water absorbed in collagen”. In: Journal of Physical Chemistry 82.14 (1978), pp. 1660–1663. DOI: 10.1021/j100503a018.

[84] D. Jordan-Lloyd. “The absorption of water by gelatin”. In: Biochemical Journal 25.6 (1931), pp. 1943–1948. DOI: 10.1042/bj0251943.

[85] C. Liao et al. “A material odyssey for 3D nano/microstructures: two photon polymerization based nanolithography in bioapplications”. In: Applied Materials Today 19 (2020). ISSN: 23529407. DOI: 10.1016/j.apmt.2020.100635.

[86] Human Retinal Engineering. June 2020. URL: http://www.tuckerlaboratory.org/Tissue$%5C%$20Engineering.

[87] W. Jager. Polymer chemistry, Lecture 3, Free Radical polymerization. Dec. 2018.

[88] H. Sun et al. “Scaling laws of voxels in two-photon photopolymerization nanofabrication”. In: Applied Physics Letters 83.6 (2003), pp. 1104–1106. DOI: 10.1063/1.1599968.

[89] Nanoscribe-GmbH. “Photonic Professional (GT) Manual User”. In: (2013). ISSN: 15214095. DOI: 10.1038/87470.

[90] D. Torres-Torres et al. “Geometry and bluntness tip effects on elastic-plastic behaviour during nanoindentation of fused silica: Experimental and FE simulation”. In: Modelling and Simulation in Materials Science and Engineering 18.7 (2010). DOI: 10.1088/0965-0393/18/7/075006.

[91] L. Angeloni et al. “Mechanical characterization of nanopillars by atomic force microscopy”. In: Additive Manufacturing 39 (2021). ISSN: 22148604. DOI: 10.1016/j.addma.2021.101858. URL: https://doi.org/10.1016/j.addma.2021.101858.

[92] 3M™ Novec™ 7100 Engineered Fluid, product information. Sept. 2021. URL: https://multimedia.3m.com/mws/media/1998180/3m-novec-7100-engineered-fluid.pdf.

[93] O.W. Reif M. W. Jornitz. Sterile Filtration. Springer, 2006, p. 149.

[94] W. Suwito et al. “Elastic moduli, strength, and fracture initiation at sharp notches in etched single crystal silicon microstructures”. In: Journal of Applied Physics 85.7 (1999), pp. 3519–3534. ISSN: 00218979. DOI: 10.1063/1.369711.